POLITECNICO

MILANO 1863

SCUOLA DI INGEGNERIA INDUSTRIALE
E DELL'INFORMAZIONE

Approach of accelerated SOFC durability test with steam treatment

TESI DI LAUREA MAGISTRALE IN
ENERGY ENGINEERING - INGEGNERIA ENERGETICA

Author: **Marco Castelli**

Student ID: 953736
Advisor: Prof. Andrea Casalegno
Co-advisors: Anke Hagen
Academic Year: 2021-22

Abstract

These days, fresh investments in the sector of renewable energy are being stimulated by knowledge of the causes and effects of climate change. In the coming decades, hydrogen will be crucial to achieving the objective of a more sustainable society, for which the European Union is a global leader in research and development (RANDD).

Devices that convert electrochemical energy have the potential to be crucial in the creation and storage of electrical energy in future energy scenarios. In contrast to traditional methods of energy production, they transform chemical energy which, for instance, is stored in a fuel directly into electrical energy. Thus, fuel cells promise lower fuel usage and CO_2 emissions as they may obtain much higher efficiencies than traditional power generation. One of the best method to make green hydrogen is electrolysis. When compared to other electrolyzers, Solid Oxide Electrolysis Cells (SOECs) in particular offer a number of advantages, including the ability to directly convert hydrocarbons, carbon monoxide (CO), and other high energy-density gases, as well as the ability to operate in both electrolysis and fuel cell modes.

The focus of this project is on study the durability, specifically to investigate approaches for shortening/accelerating lifetime testing. Steam treatment at OCV was studied as an accelerating factor at the SOFC stack level. The stack A composed of state-of-the-art anode-supported cell, was tested at OCV for 500 h, and the second stack, stack B was tested for 1400 h at the same conditions both at a temperature of 750°C with a fuel composition of 10/90 H_2/H_2O.

The difference between the two stacks were that Stack A was new and the Air electrode is composed by LSC, instead stack B was already tested for 1000h in co-electrolysis and the air electrode is composed by $LSCF$. The stack A showed a degradation for the ohmic resistance of 6.7% and the polarization resistance degradation of 33.5%, were the big changes was identified in Bode diagram at high frequency range, instead stack B was shown unexpected behavior: an increase of performance in the polarization resistance for the first 900 h.

The influence of steam is interesting under OCV. From one side can be considered has a parameter to increase the acceleration of the degradation. And from the stack B, tested in

co-SOEC in the pre-history, the steam treatment does not cause degradation and it is possible to regain some performance lost caused by degradation during the prior operation, for example, carbon deposition.

Further research and development should focus on understand the mechanism behind high content of steam in order to gain a better understanding of this cell's behavior, and accelerate the degradation processes.

Keywords: SOFC, OCV, H_2O, degradation, acceleration, carbon deposition, high steam content.

Abstract in lingua italiana

In questi giorni, nuovi investimenti nel settore delle energie rinnovabili vengono stimolati dalla conoscenza degli effetti del cambiamento climatico. Nei prossimi decenni, l'idrogeno sarà fondamentale per raggiungere l'obiettivo di una società più sostenibile, per la quale l'Unione Europea è un leader mondiale nella ricerca e sviluppo (RANDD).

I dispositivi che convertono l'energia elettrochimica hanno il potenziale per essere cruciali nella creazione e nell'immagazzinamento di energia elettrica negli scenari energetici futuri. Contrariamente ai metodi tradizionali di produzione di energia, trasformano l'energia chimica che, ad esempio, viene immagazzinata in un combustibile direttamente, in energia elettrica. Pertanto, le celle a combustibile promettono un consumo di carburante ed emissioni di CO_2 inferiori poiché possono ottenere efficienze molto più elevate rispetto alla generazione di energia tradizionale.

Uno dei metodi migliori per produrre idrogeno verde è l'elettrolisi. Rispetto ad altri elettrolizzatori, le celle di elettrolisi a ossidi solidi (SOEC) in particolare offrono una serie di vantaggi, tra cui la capacità di convertire direttamente idrocarburi, monossido di carbonio (CO) e altri gas ad alta densità di energia, nonché la capacità di operare sia in modalità elettrolisi che cella a combustibile.

L'obiettivo di questo progetto è lo studio per accelerare il tempo di testing, attraverso l'applicazione di un fluido 90% vapore e 10% H_2 a OCV, testando due stack SOFC. Lo stack A, composto da celle nuove, con l'anode come supporto, è stato testato a OCV per 500 ore e il secondo stack, lo stack B, è stato testato per 1400 ore alle stesse condizioni, entrambi a una temperatura di 750 ℃.

La differenza tra i due stack si compone da: lo stack A è nuovo e il catodo è composto da LSC, invece lo stack B è già stato testato per 1000 ore in coelettrolisi e il catodo è composto da LSCF. Lo stack A ha mostrato una degradazione nella resistenza ohmica del 6,7% e la degradazione della resistenza di polarizzazione del 33,5%, dove i grandi cambiamenti sono stati identificati nel diagramma di Bode nel range delle alte frequenze, invece lo stack B ha mostrato un comportamento imprevisto, infatti si è ottenuto un aumento di prestazioni nella resistenza di polarizzazione per le prime 900 h.

L'influenza del vapore a OCV è interessante. Da un lato, il vapore, diventa un parametro

che si può considerare per aumentare l'accelerazione del degrado. E dall'altro come si nota dallo stack B avente una storia antecedente in co-SOEC, col trattamento a vapore, recupera alcune prestazioni perse causate dal degrado durante l'operazione precedente, ad esempio dovuto al carbon deposition.

Ulteriori ricerche e sviluppo dovrebbero concentrarsi sulla comprensione del meccanismo alla base dell'alto contenuto di vapore nel fluido d'ingresso, al fine di ottenere una migliore comprensione del comportamento di questa cellula e accelerare i processi di degradazione.

Parole chiave: SOFC, OCV, H_2O, degradazione, accelerazione, carbon deposition, alto contenuto di vapore.

Contents

1 | Introduction

Renewable energy sources are gaining popularity as their position in all nations' energy portfolios steadily rises in response to the growing awareness of climate change challenges and the need to pursue sustainable development; this will open a possibility for hydrogen. This chapter will focus on the energy situation in the world, on emissions, and then on goals introduced by the international community by Europe and the possibilities for hydrogen.

1.1. Overview in world and Europe situation
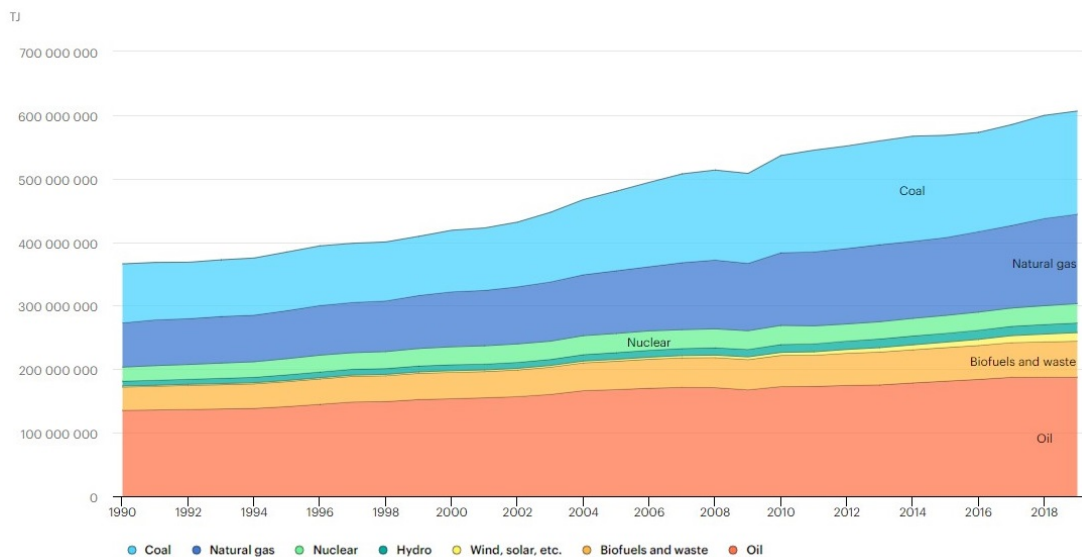
1.1.1. Situation World

Figure 1.1: Energy sources used from 1990 in the world. Figure from IEA, Global share of total energy supply by source, 2018, IEA, Paris

This section discusses how the energetic situation is characterized in the world and the impact of this situation, and different goals for de-carbonization.

From Figure 1.1 it is possible to appreciate the situation of energy supplies in the last years worldwide. The three main power supplies are oil with a share of 31.6%, coal with a share of 26.9 % and at the end natural gas with a share of about 22.8%. Those three energy supply trends during the past years have been increasing yearly due to the rise in the demand. In the last few years, renewables started to have a small share of the energy supply, but still low compared to the others. Figure 1.2 represents the total concentration of CO_2 from 400000 years until today with a forward prevision till 2100. Throughout history, there have been some changes in the concentration of CO_2 in the atmosphere but never reached a level as in those last years. These changes started after the industrialization period, and the projection is related to a situation kept constant in those last years.
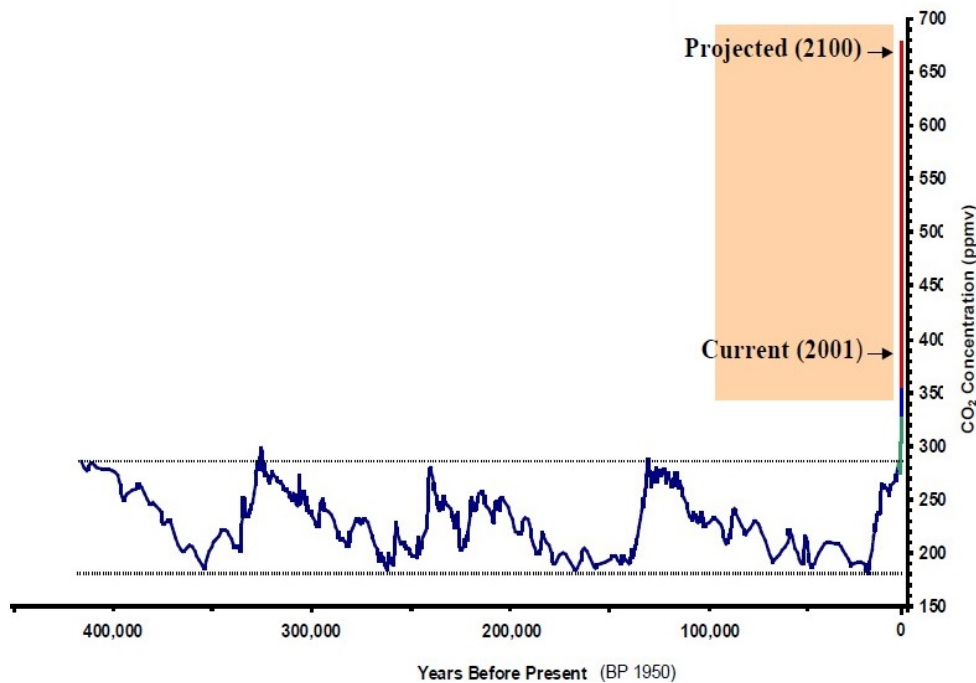

Figure 1.2: Past and projection of CO_2 concentration in atmosphere. Figure from IPCC

From figure 1.3 is possible to appreciate that the main sector that has a significant impact on emission is electricity and heat. The other two sectors with a significant influence are industry and transport.

From this analysis is possible to understand that globally needed a huge effort to reduce emissions. During the past years, significant work has been done to reach all countries' knowledge and a common plan.

In fact, during the past years, there have been different international cooperation on climate change from 1988 For instance, in the 1997 Kyoto, and in 2009 Copenhagen

summit, but the main goals were reached in 2015 in Paris with the so call Paris agreement.
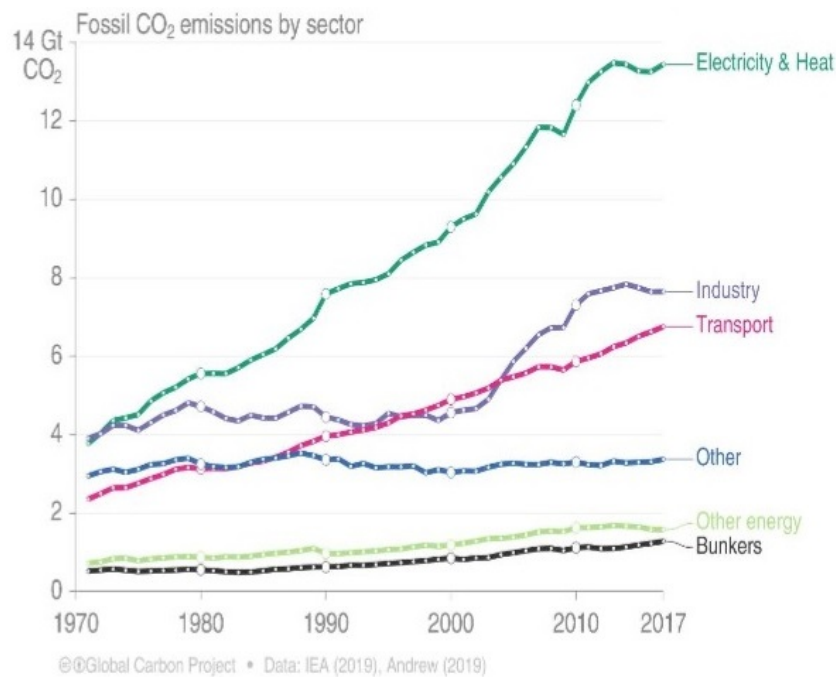
Figure 1.3: Emissions of CO2 by sector. From IEA

The Paris agreement is a legally binding international treaty on climate change, where there were 196 parties. This agreement aimed to regulate the maximum temperature reachable, expressed to be 2°C below the set temperature in 1990, then carbon neutral by 2050, with a revision period after 5 years.

1.1.2.   Situation Europe

In Europe, instead, there is a slightly different situation compared to the rest of the world; as is appreciable from Figure 1.4, the primary fuels used are oil, coal, natural gas, nuclear, and it is possible to appreciate that in the last few years there is a downward trend for the use of coal and oil.

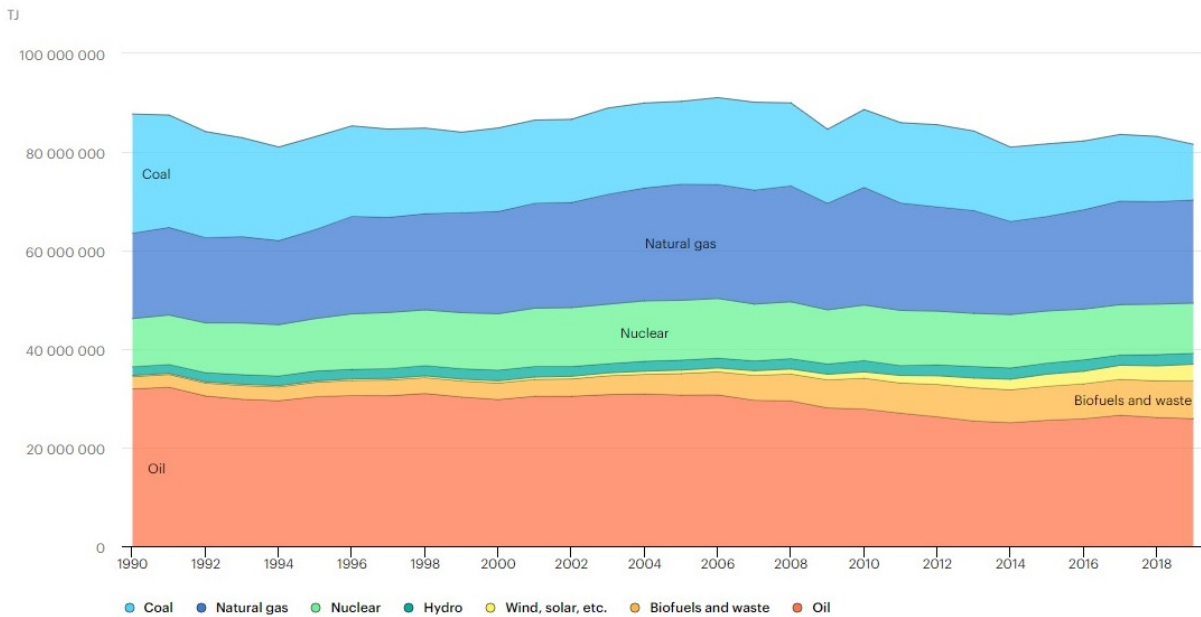Figure 1.4: Total energy supply in Europe by from 1990. Figure from IEA

Europe in 2020 created the deal called: the Green deal, which is a plan for making the EU's economy more sustainable and has a vision of the future EU energy system based on an integrated energy system. The integrated energy system means that energy flows between users and producers and will have three characteristics: a cleaner power system with more direct electrification of end-use sectors like industrial heating of buildings and transportation, a cleaner fuel system for difficult-to-electrify sectors like heavy industry, and a "circular" system that is more efficient and where waste energy is gathered and utilized.

The green deal's goals are composed of: reaching carbon neutrality by 2050, 2030 cut the gas emission to 55%, increasing energy efficiency, and integrating renewable energy into the system.

1.2. Future of hydrogen

Europe's total hydrogen production capacity at the end of 2018 was 11.5 million tons per year [10]. The most prevalent method of obtaining hydrogen is through on-site captive production, with roughly two-thirds of all hydrogen production capacity being set aside for own consumption. The most common technology for producing hydrogen is steam reforming of natural gas. The electrolysis is used in Europe when the capacity is insufficient to use a built dedicated steam reformer, or the capacity is too high for external supplies such as a cylinder or tube trailers. According to EU Joint Research Centre, the capacity of

the electrolyzers is about 1 GW, which is 1.6% of the total hydrogen production capacity. Instead, the power to hydrogen is still a marginal part of the market.

The leading producer in the EU is Germany which has a capacity of about 2.5 Mt of hydrogen per year.

The sector's demand is divided into 45% in the refinery and 34% in ammonia [10] These two account for 4/5 of the use of hydrogen. The 1% use is in the energy sector that is used in combined heat and power(CHP), where hydrogen is burned and produces heat and power, produced on-site, thanks to other processes.

For the future, the planned installation of electrolyzer by 2040 is 20,011 MW and expected an installation of 22,900 km of network for hydrogen by 2040, called Europen Hydrogen backbone. Then other projects were proposed as "green flamingo" an Iberian green hydrogen export connected to the Port of Rotterdam, or "green spider" which connects Spain, France, and Germany [43].

The need for storage for intermittent renewable energy is evident; in addition to conventional energy storage methods like pumped hydro, compressed air storage, or secondary batteries, hydrogen is a practical alternative.

In Europe, the road map for hydrogen is building by 2030, 40 GW of renewable hydrogen electrolyzers and 10 Mt of production.

Hydrogen is expected to help the integration of renewables in the various sectors; in fact, hydrogen can be used in stationary power supply, especially in emergencies, grid balancing, and combined heat and power. The use of hydrogen in refitting pipes of methane can be a new way to use the lost power from renewables, and a blending of the two gases can become an early step toward gradual gas grid decarbonization [10]. One of the big issues is the maximum legal or safely acceptable hydrogen concentration in the pipes.

The reason why hydrogen in electricity storage has hindered it is round trip efficiency, the cost, and lifetime of electrolyzers. However, the increase of unpredictable renewable with fluctuating supply, and with some new research and development, can be more attractive in the future.

1.3. Fuel cell

This subchapter describes the electrochemical device fuel cell. This device, known as a fuel cell, can directly and continuously transform the chemical energy of fuels like hydrogen, methanol, ethanol, or natural gas into electrical energy.

The principle of the fuel cell is reported in Figure 1.5, in this image is reported solid oxide fuel cell for simplicity.

One possible data as indicated the invention of the fuel cell is in 1839 as the invention

of gas battery by Sir W. Grove & C. Schönbein, but during the last 30 years, fuel cells have received enormous attention worldwide for their potential for power generation in portable, transport, and stationary applications.
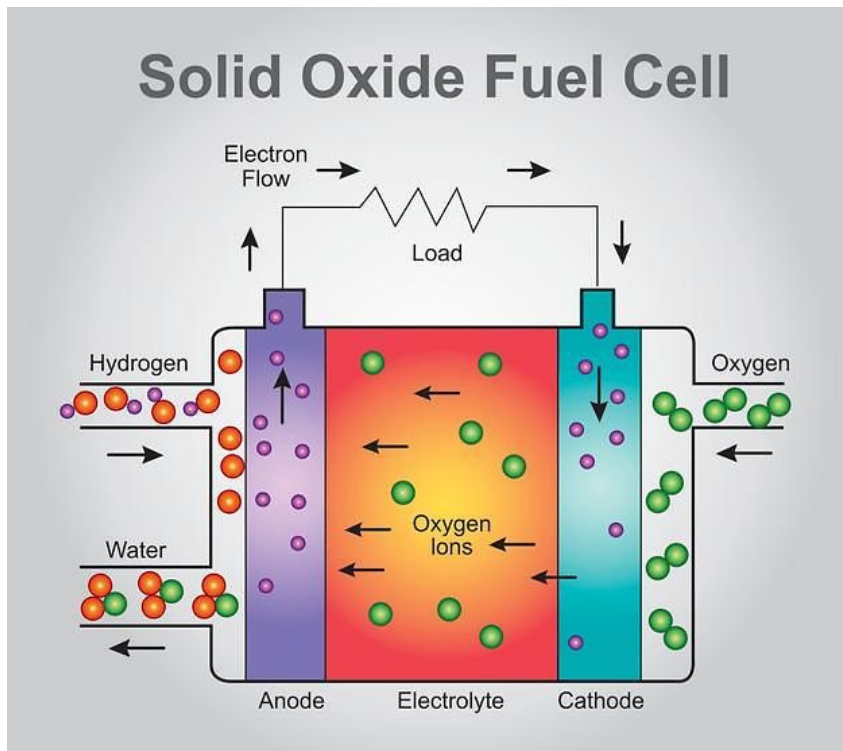

Figure 1.5: Scheme of Solid Oxide Fuel Cell

All the fuel cells are composed of an anode, electrolyte, and cathode, fuel e.g hydrogen passes over the anode side, and oxygen passes over the cathode side. Two reactions occur on those two sides, is present a proton or ion movement in the electrolyte, and electrons are moved in the electric circuit, that connects anode to cathode, generating power in case of the fuel cell. The next chapter will be described in detail, but more important is that no collision between the two fuels must happen, otherwise chemical combustion of hydrogen in oxygen will take place.
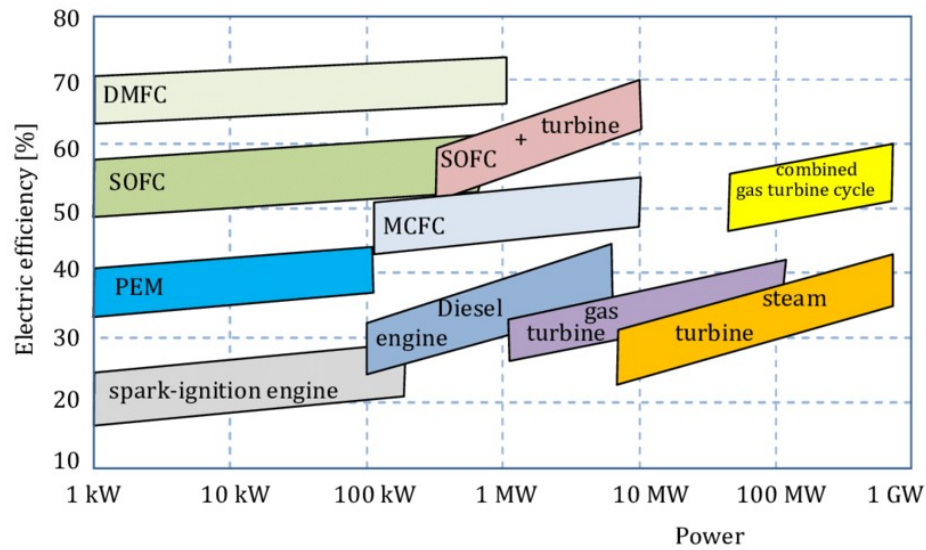
Figure 1.6: Electric efficiency vs power for different technologies. Shown [27]

The important aspects are that fuel cells are intrinsically more efficient than other energy conversion technologies, as represented in Figure 1.6, and emit far fewer greenhouse gases. In fact, for this reason, water electrolysis is starting to obtain more and more interest, in fact, works as the inverse of the fuel cell, with water as fuel input, to obtain hydrogen and oxygen. Hydrogen is an energy carrier, which can be stored and used to balance the grid in case of needs or use via the synthesis of liquid biofuels, e.g ammonia, and methanol.

1.4.   Classification of fuel cells

Different categories for categorizing fuel cell types based on electrolytes, fuels, or temperatures can be used, reported in Figure 1.7.
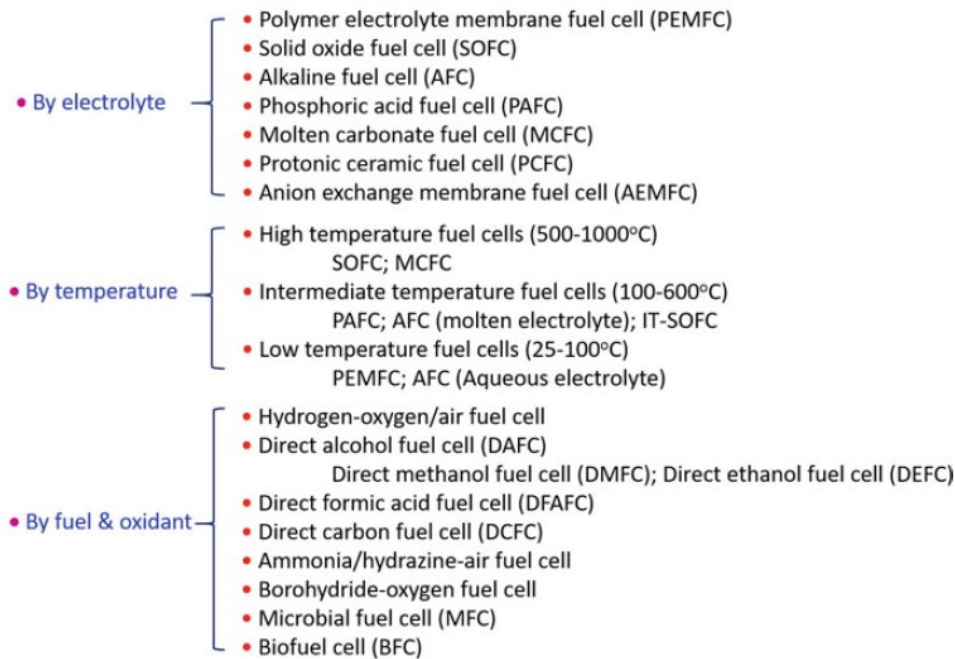
Classification of fuel cells

- By electrolyte
  - Polymer electrolyte membrane fuel cell (PEMFC)
  - Solid oxide fuel cell (SOFC)
  - Alkaline fuel cell (AFC)
  - Phosphoric acid fuel cell (PAFC)
  - Molten carbonate fuel cell (MCFC)
  - Protonic ceramic fuel cell (PCFC)
  - Anion exchange membrane fuel cell (AEMFC)

- By temperature
  - High temperature fuel cells (500-1000ºC)
            SOFC; MCFC
  - Intermediate temperature fuel cells (100-600ºC)
            PAFC; AFC (molten electrolyte); IT-SOFC
  - Low temperature fuel cells (25-100ºC)
            PEMFC; AFC (Aqueous electrolyte)

- By fuel & oxidant
  - Hydrogen-oxygen/air fuel cell
  - Direct alcohol fuel cell (DAFC)
            Direct methanol fuel cell (DMFC); Direct ethanol fuel cell (DEFC)
  - Direct formic acid fuel cell (DFAFC)
  - Direct carbon fuel cell (DCFC)
  - Ammonia/hydrazine-air fuel cell
  - Borohydride-oxygen fuel cell
  - Microbial fuel cell (MFC)
  - Biofuel cell (BFC)

Figure 1.7: Fuel cell classification.Shown [21]

The most famous classification is based on electrolyte materials. The following subchapter is going to be described in summary the different typologies.

1.4.1.   Alkaline fuel cells (AFCs)

The alkaline fuel cell uses concentrated KOH as an electrolyte and operates at a high-temperature 200°C with a high concentration of KOH or at a lower temperature for less concentration. It can use different electrocatalysts such as Ni, Ag metal oxides, and noble metals; in fact, it was one of the first modern fuel cells developed[21], reaching an efficiency of around 45-60%.
The advantages are that it has fast cathode kinetics, cheap electrolyte, and low-cost catalysts; the disadvantage: is sensitive to CO_2 in both fuel and air, and it is a complex system. The application can be military and space with a power range of 1-100 kW.

1.4.2.   Polymer electrolyte membrane fuel cells (PEMFC)

Pem uses polymeric materials as an electrolyte, the most common is perfluorosulfonic acid such as Nafion. The materials have high ionic conductivities that are more than 0.1 S/cm, PEMFCs are the most advanced fuel cell vehicle technology currently available,

and the state of the art of electrocatalyst for both oxygen reduction reaction and hydrogen oxidation reaction is platinum, reaching an efficiency of around 40-60%. The main issues are related to water management, scarcity and cost of platinum.

Instead, the advantages are solid construction, high power density low temperature, quick start-up, and fast load response; the negative aspects are that uses a noble metal catalyst, CO intolerance, water management, intensive cooling, and low waste heat value.

The application can be backup power portable power transport distributed generation with a power range between 10W and 1MW.

1.4.3. Solid oxide fuel cell

This fuel cell is the one analyzed in this thesis, SOFC are all-solid devices; this type of fuel cell doesn't need precious metal electrocatalysts because of their high operating temperatures of 600-1000 °C [21] and has the possibility to operate in the reverse mode so in electrolyzers and fuel cell switching fuels. Has the possibility to use different types of fuels as hydrocarbons for high temperatures. This high temperature is related to the low oxide conductivity and high activation energy of oxide electrolytes such as YSZ.

The challenges in SOFC technologies are thermal stability, stack durability, and reduction of temperature. In fact, the thermal instability is leading to different thermal coefficients for diverse components in stacks.

The advantages are high efficiency, high solid construction, fuel flexibility, non-noble metal catalysts, and good heat value. Instead, the disadvantages are a thermal mismatch, poor thermal cyclability, and a slow start. The application is auxiliary power electric utility distributed generation with a power range between 1kW and 2MW.

1.5. Classification SOFC

There are two different classifications for the SOFC, one is related to the geometry of the cell, and the other is related to which is the support of the cell.

1.5.1. Cell design

SOFC can be manufactured in different ways, the main one is planar or tubular geometry. The planar geometry presents lower manufacturing cost and high power density, but sealings must be applied later on with high temperature, or with sealing concepts Figure 1.8(a).
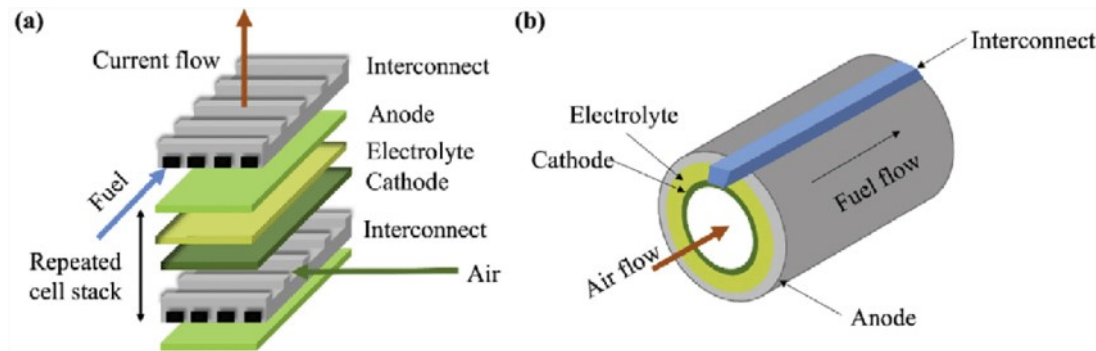
Figure 1.8: Cell design: left planar geometry, right tubular geometry. Shown [34]

Instead, the tubular geometry presets lower power density, for the long current path, and the manufacturing cost is higher than the planar cell. However, are mechanically strong, long-lasting, and tolerant to severe temperature changes. Then operating temperatures are higher, but the sealing can be made at a lower temperature Figure 1.8(b).

1.5.2. Cell concepts

There are different cell concepts in the planar panorama. The cell is composed of cathode electrolyte and anode, and only a few tenths of μm thick is required for the active layer, then is necessary to provide a layer of mechanical support. This additional layer can be composed of one of the three levels or can be made by an additional stratum different from anode-cathode and electrolyte.

This subchapter will summarily explain the five different concepts with features and commercial manufacturers where the name comes from the mechanically support layer.
The first concept is the electrolyte supported (ESC), Figure 1.9(a), which is composed of a thickness of the electrolyte in the range of 100 μm, this high thickness requires a high operating temperature (900-1000°C) for the oxygen ion conductivity. A new improvement of thickness has been studied reducing the temperatures. The advantage is the mechanical strength due to the dense electrolyte. A problem is that a lower working temperature necessitates strong electrode electrocatalytic activity and high ionic conductivity of the electrolyte to compensate for the cell's loss without sacrificing the power density obtained at high temperatures. A way to overcome this problem is to reduce the electrolyte thickness using anode-supported or cathode-supported cells. Two companies' examples for this typology of the cell are Sunfire-Staxera and Bloom Energy.
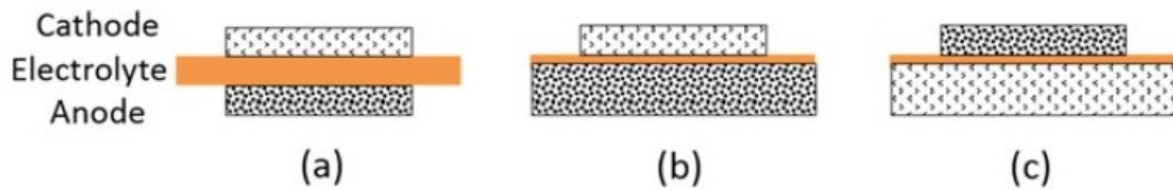
Figure 1.9: Typical cell structures used in SOFCs: a electrolyte-supported,b anode-supported, and c cathode-supported [21].

Anode supported (ASC) is the most common supported cell. The state-of-the-art is composed of a thick porous supporting layer of 500 μm, as reported in Figure 1.9(c) which has a lowering operating temperature of <800°C, having a reduction of the ohmic resistance, and to enhance the cell efficiency the electrolyte must be thin. The anode is made up of a porous layer with lower mechanical strength than a layer that isn't porous, making it more difficult to resist the mechanical and thermal stresses brought on by fast temperature changes. With this composition, there is a substantial risk of cell failure due to redox cycling brought on by air entering the anode compartment when the fuel supply is cut off. One company that produces this type of composition of the cell is Solidpower Spa.

An additional typology of the cell is the cathode-supported cell (CSC) Figure 1.9(b), which, thanks having a thin electrolyte, has a lower temperature of <800 °C and has some advantages in using hydrocarbon fuels with low steam/carbon ratios, due to the low anode thickness that is electrochemically active, and thus reduce the risk of carbon deposition. Other advantages are: is not present the cycling redox problem, is can be subjected to volume contraction, due to the thin anode compared to the anode supported. On the other hand, there are huge manufacturing challenges and higher costs [43] and one of the main producers is Siemens.

The last two concepts present in the anode-supported cell are composed of an additional layer attached to the anode stratum. One is the porous substrate supported, which is the main one produced by the Mitsubishi, that presents lower temperature thanks to the thin cell. The other is metal supported which presents a lower operating temperature possible <600°C thanks to the thin cell, presents high mechanical strength, and flexibility, but of course, is under study for the challenges for the metal corrosion at DTU.

2 | Solid oxide cells

Reversible Solid oxide technology is an energy conversion device that converts chemical energy into electric energy through an electrochemical reaction; this technology has been studied for years. The great possibility behind this technology is the bifunctional operation, fuel cell, electrolysis, and high efficiency [18, 40]. The next subchapter will describe the function, materials, and main mechanism of degradation.
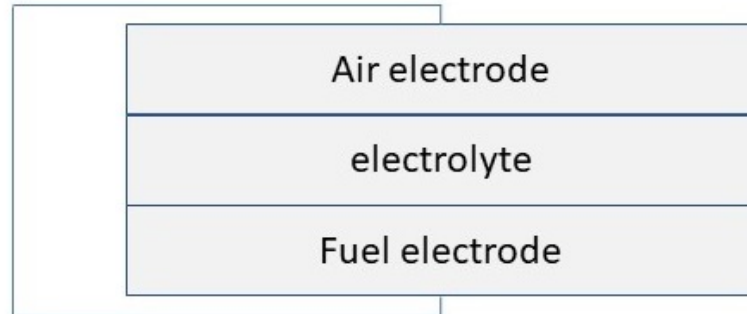
2.1.   Basic function

Figure 2.1: Scheme Solid Oxide Fuel Cell.

The Solid oxide cell is composed, as reported in Figure 2.1, of two electrodes: an air electrode, a fuel electrode, an electrolyte, and an electric circuit that connects in between the two electrodes.

In the Air electrode and in the Fuel electrode two main reaction occurs:

$$O_2^- <-> 1/2O_2 + 2e^- \tag{2.1}$$

$$H_2O + 2e^- <-> H_2 + O_2^- \tag{2.2}$$

The reaction that occurs in the Air electrode has two verses explained by the two arrows equations (2.1)(2.2). The reaction can occur on the right(2.1), called oxygen evolution, when it is in the electrolysis mode, or can occur on the left, called oxygen reduction, if it is in fuel cell mode. Figure 2.2

Instead, the reaction occurring in the Fuel electrode has two directions, eq(2.2). The one occurring on the left is called hydrogen oxidation, which happens in fuel cell mode, and hydrogen evolution (right) if it is in the electrolysis mode. Figure 2.2
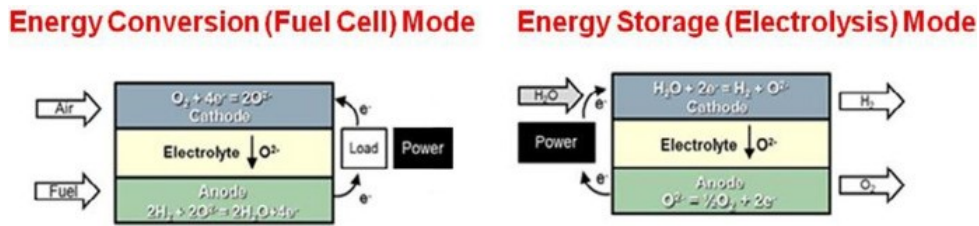
Figure 2.2: Reverse Solid Oxide Cell, left fuel cell mode, right electrolysis mode[29].

Each layer has its own function: Air electrodes must have good performance in gas transport thanks to their porosity, high electron and ion conductivity, and excellent catalytic activity for oxygen reaction.

The electrolyte must be gas tightness, a good ion O^{2-} conduction to bring ions from the cathode to the anode, and electrical insulation. In the end, the fuel electrode must have good catalytic activity for fuel oxidation, good gas transport thanks to the porosity, and good electron and ion conductivity.

The purpose of the electric circuit, between the two electrodes, is to provide electrons from one side to the other for the different reactions.

To overcome the ohmic loss from the electrolyte, solid oxide cells operate at temperatures between 650 and 800 °C and above. They can also use fuels such as H_2, Co, Ch_4, and hydrocarbons. The layers and the sealing materials must all be able to preserve chemical and thermic stability under those circumstances. In the following subsections are described the different layers.

2.1.1.   Air electrode

The basic structure of the Air electrode is based on the ideal cubic Perovskite oxide family (ABO_3).

An example of the construction (air electrode) is presented in Figure 2.3. A and B, in this structure, are cations, and the structure can be described as a 3-dimensional network of corner-sharing BO_6 octahedral, instead, the 12-fold A cations occupy all available
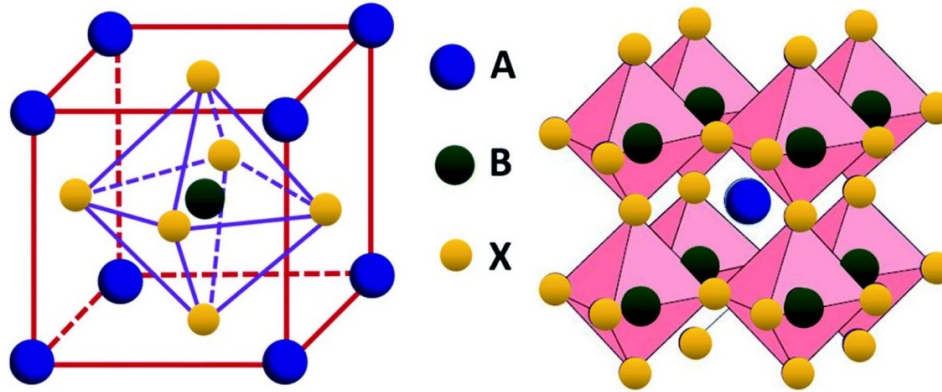
positions.

Figure 2.3: ABO_3 perovskite cubic structure schematic representation, A cation in blue, B cations in black and oxygen ions in yellow. Shown [18].

Since ABO_3's chemical bonds are highly ionic, they can be conceptualized as spheres with set radii. Perovskite has a basic cubic lattice structure, although there are other deformed forms, such as orthorhombic and hexagonal lattices, that have lesser symmetry. Figure 2.3.

A way to assess this is through Goldschmidt tolerance factor eq(2.3), where ra, rb and ro are the effective ionic radii.

$$t = \frac{(r_a + r_b)}{\sqrt{r_b + r_o}}, \tag{2.3}$$

If t is close to one, the probability of having a cubic structure is higher but it is not possible to predict the space group under the consideration that the material will crystallize only on the basics of calculated value t [18]. This structure is responsible for the transport of electrons due to the fact that the $3d$ orbitals of the metal, which is in octahedral configuration, overlap with the $2p$ orbitals of the oxygen atoms in this structure. Instead, ionic transport is possible, thanks to oxygen vacancies. In the end, is desirable to have a high mixed ionic-electronic conductivity of perovskites improving the cathode performance.

Different chemical compositions exhibit various physicochemical properties. As stated above, the material must possess a variety of qualities, including high ionic-electronic conductivity, chemical, and dimensional stability, thermal expansion comparable to that of other cell components, minimal reactivity with the electrolyte, high catalytic activity for oxygen dissociation/reduction, and porosity to allow gas to pass through the substance with ease.

The perovskites materials, made of $LN_{1-x}A_xMO_3$ oxides, are the favored candidate group in addition to noble metals, where: LN: lanthanides, A: alkali-earth metals

$(e.g. Sr, Ba), M$: composition of $Fe, Co,$ and Mn. The most used materials are: $LSCF, LSC$ and LSM.

The LSM Air electrode, made of $(La_{1-x}Sr_x)MnO_3$, was utilized by the initial version of SOFC. LSM was used because of its high electronic conductivity and high thermodynamic stability, although its operating temperature is 1000 °C, and its efficiency drops at lower temperatures [18].

To get a high p-type electrical conduction owing to the creation of a significant quantity of Mn^{4+}, lanthanum manganite $(LaMnO_3)$ is replaced with low valence elements like Sr. [18] This material has not been an ideal candidate due to the low ionic conductivity and slow surface oxygen exchange kinetics. [18] This material is characterized by high electronic conductivity at high temperature (>900°C), but the objective of the new studies are materials that can operate at a lower temperature, down to 600°C.

The perovskite family oxides, such as lanthanum strontium cobalt ferrite $(La, Sr)(Co, Fe)O_3$ called $LSCF$ or $(La_{0.6}Sr_{0.4})_{0.98}CoO_3$ LSC, are state-of-the-art for the material. These materials were chosen because they exhibit faster oxygen exchange kinetics compared to LSM and higher rates of oxide ion diffusion. The interaction of the cathode with the electrolyte (YSZ) at high temperatures is the only factor affecting cathode performance, so a thin layer of $Ge_{0.9}Gd_{0.10}a_{0.95}$ (CGO) is positioned between the YSZ and the Air electrode. [14, 20, 23]

2.1.2. Fuel electrode

The fuel electrode has various properties that must be respected, including the following: first and foremost, it must be an excellent catalyst for the oxidation of the fuel, stable in the reducing environment, sufficiently porous for gas in and out, and electronically conducting. The Fuel electrode must have the same thermal expansion coefficient as the other components and be chemically stable. At the beginning of SOFC, precious metals such as $Pt, Au,$ or Ni were studied. These candidates, as Ni, present an excellent catalyst but high thermal expansion coefficient $13.4 \times 10^{-6}/C$ [18], exhibiting a coarsening microstructure caused by the metal aggregation. The composition of $Ni - YSZ$, which is a state-of-the-art solution, was discovered to be capable of preventing the sintering of nickel particles. This brought a decrease in the effective thermal expansion coefficient of Ni and increased the adhesion with the electrolyte.

At the end Ni/YSZ has bivalent purposes, from one side being a catalyst and an electrical current collector from the other. Nickel is also quite active in the steam reforming of methane. Under reducing conditions, Ni can catalyze the formation of carbon from hydrocarbons, and if sufficient amounts of steam are not present together with the hy-

drocarbons on nickel surface, the anode activity may be affected. [18]. Additionally, Ni/CGO is a different substance that could also be used in the future.

Three phases are involved in the electrochemical reaction of gaseous reactants: gas phases, ceramic electrolytes, and metallic electrodes. The line where the intersection of the electrons on the Ni atom, the ion in the electrolyte, such as O_2, and the fuel gas is known as the TPB three-phase boundary. The TPB length and Ni particle radius have an inverse correlation, and the longer the TPB length per unit cell area, the lower the polarization resistance. This means that to achieve longer TPB, small Ni grain sizes are desired [18]. Because of the increased surface mobility at high temperatures [38] causing sintering and agglomeration, the goal of YSZ is to manage porosity and resolve Nickel's coarsening issue. [18]. A 40% nickel and 60% yttria composite has been discovered to have the lowest polarization resistance. And, also the porosities of roughly 30–40%, are the ideal microstructure for an electronic channel, prevent nickel agglomeration, and create paths for appropriate gas diffusion [24].

For support, instead, the cell can have an additional layer of $3YSZ$. 3 indicates 3 mol% $Y2O3$ which is one of the strongest ceramics mechanically for the martensitic transformation.

2.1.3.   Electrolyte

There are different electrolytes, but the state of the art is composed of $8YSZ$, 8 indicates the 8 mol% $Y2O3$, and this composition has the highest oxide ion conductivity [31].

Attached to the electrolyte, there is placed a reaction barrier of $Ce_{0.9}Gd_{0.1}O_{1.95}$ (CGO) to divide the perovskite and the electrolyte that otherwise will react at sintering temperature. Figure 2.4 shows a microscopy picture of the different layers.
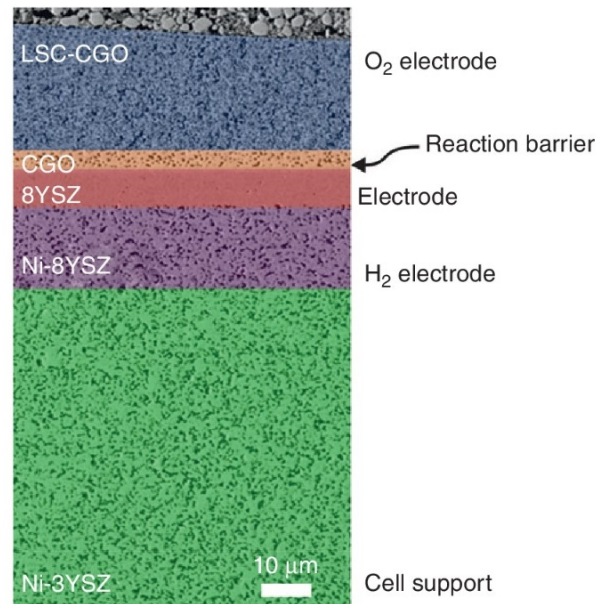
Figure 2.4:   Artificially coloured scanning electron microscope (SEM) of a DTU-manufactured cross-section solid oxide cell [31].

2.1.4. Interconnect material

The purpose of the interconnect material is to provide the separation between the air and fuel and provides the electrical connection between cells. As represented in Figure 2.5 the interconnect is composed of a plate where the fuel flows in a gap and then towards the Nickel plate; instead, the Air flows between the top part of the interconnect and the bottom of the next plate. The typical characteristic that the material chosen have to meet are different: high electronic conductivity, low ionic conductivity, chemical stability, matching thermal expansion with the cell, high mechanical strength, and high thermal conductivity. Doped lanthanum chromite has been utilized as the interconnect to meet those specifications. For cells that can reach a max temperature below 800 °C, it is feasible to employ metallic materials with oxidation resistance that, in comparison to lanthanum chromite, are simple to produce, less expensive, but must withstand both oxidation and corrosion in a dual atmosphere (oxidizing atmosphere one side and reduction on the other side). A protective oxide layer is formed in situ by oxidation or ex-situ by coating to manage this difference in the atmosphere.
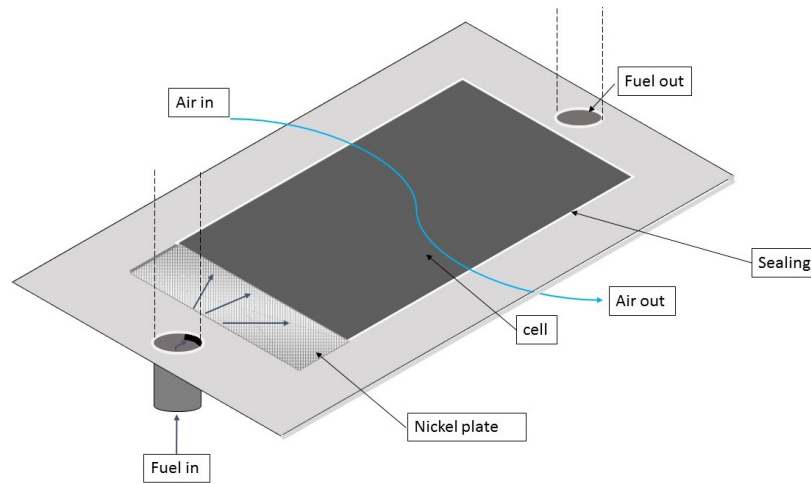
Figure 2.5: Interconnection, composed by a cell, a nickel plate and sealing material.

Another promising material is Ferritic stainless steel, due to the low cost and proper thermal expansion, but it has a huge issue due to the formation of chromium at the electrolyte and cathode interface, creating a poisoning of the cathode. The deterioration of the SOFC's performance is significantly influenced by the volatility of the Cr species. Through interactions of the cathode with $CrO_2(OH)_2$ are regarded as the primary cause, the mechanism of Cr poisoning is unclear [18]. To prevent the rapid deterioration of the cathode´s oxide reaction, a suitable surface layer can be placed on the interconnects to reduce the Cr evaporation.

2.1.5.   Sealing Materials

In planar SOFC stacks, seals are essential for preventing leakage outside the stack and between fuel and oxidant gases. As represented by Figure 2.5, the sealing significantly impacts the stack's stability since it must exhibit specific characteristics: it must be thermochemically stable, electrically insulating, the same thermal expansion of the cell components, and it should not migrate. And the ability to survive thermal cycling between operational temperature and room temperature is the last requirement.

Some examples are glass-ceramics and brazes, compliant seals e.g. viscous glasses, and compressive seals eg mica-base composites. Composition based on silica has so far produced the greatest results [18]. Brazing has been explored as a potential sealing technique in addition to glass seals.

2.1.6. Cell degradation

This subchapter is going to be described the degradation of the different components of the cell. Three categories of degrading processes have been established for $Ni-YSZ$ anodes: (1) material transport mechanisms, (2) deactivation and passivation mechanisms, and (3) thermomechanical mechanisms. [24] Most deterioration described in the literature is linked to current density, maybe because tests are conducted in galvanostatic mode [31, 39].

The first mechanism is related to the microstructural changes due to the movement of Ni. This phenomenon is composed of loss of $Ni-Ni$ contact and changes in the Ni grains. The coarsening is attributed to diffusion/sintering of particles and by Ni transport in the gas phase [24]. The sintering of Ni particles at high T is a crucial step in coarsening Ni. This can happen as a result of the diffusion of vacancies as well as the fact that smaller particles have higher surface energies and aggregate to lower energies. Due to the loss of $Ni-Ni$ contact[30], this increase in Ni size will decrease TPB, increase polarization resistance, and reduce electrical conductivity. Different research has described that dry and humid conditions influence the degradation, and a way to prevent this phenomenon is using sintering inhibitors, for instance CeO_2 to retarding the Ni growth and keep higher TPB [24].

The creation of $Ni(OH)_2$, which is caused by various chemical and physical processes, is another process that contributes to the coarsening of nickel. Typically, a substantial number of particles evaporate off smaller grains and settle on bigger grains.

Recent findings show that $Ni-YSZ$ deterioration is related to Ni removal from the cermet as well, $Ni-YSZ$ degradation is not only due to Ni particle growth. The high-water vapor pressures are shown to be connected to the stability of the Ni in the fuel electrode [18]. In fact it has been demonstrated that $Ni(OH)_2$ has a significant vapor pressure at high Ph_2O, creating a depletion of Ni from the cermet of the fuel electrode.
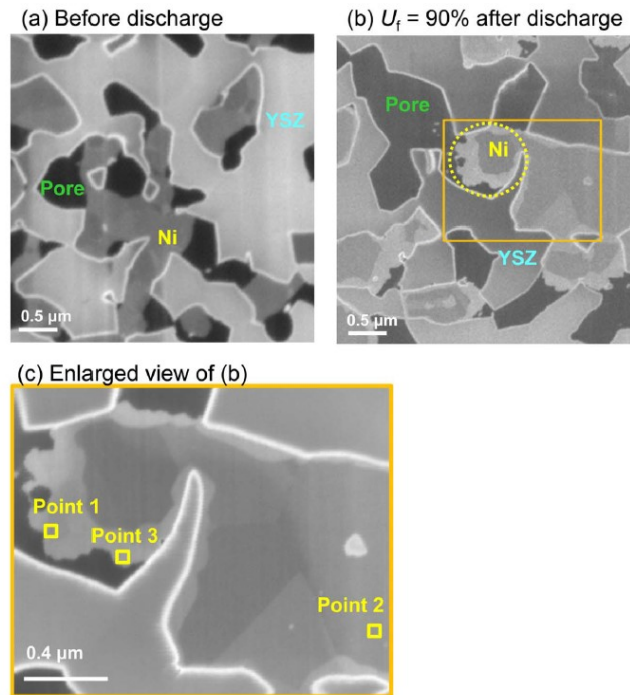
Figure 2.6: Sem rapresentation of possible Ni oxidation.[28]

This study gives an illustration of how a high steam concentration and high fuel utilization lead to an increase in oxidation and, subsequently a decrease in the TPB of the fuel electrode [28]. Figure 2.6 reports the SEM picture, which shows a grey area of Ni that may be an oxidation surface and which is present as a detachment from the YSZ.

High fuel utilization in [15] is defined as UF and is defined as the ratio of consumed fuel and total fuel supplied.

Impurities in carbonaceous fuels cause the second mechanism of degradation, which is deactivation and passivation. The electrode then is sensitive to different poisoning and trace impurities in different materials of the cell component like B, S, P, As, Cl and Cr.

For example, the segregation of glassy SiO_2 and Na_2O blocks the TPB in the $Ni-YSZ$ electrode; from [31], it has been discovered that impurities containing S often dissolve at temperatures higher than 700°C and adsorb on active Ni surfaces, inhibiting electrochemistry; this sulfur on nickel surface will inhibit O^{2-}, and slow down electrochemical reaction rate blocking the TPB. A higher level will be formatted irreversibly with nickel sulfide Ni_3S_2, which will permanently damage the cell [24].

Because most fuels from fossil sources contain sulfur, sulfur poisoning is the fuel impurity that has been the subject of most research [18]. In Figure 2.7 we can see that an H_2S content of 50 ppm between 700-850 °C, Ni will be fully covered; a way to overcome this problem is using scandia stabilized zirconia ($Ni-SSZ$) that is less affected by H_2S [18]

compare to the usual $Ni - YSZ$.
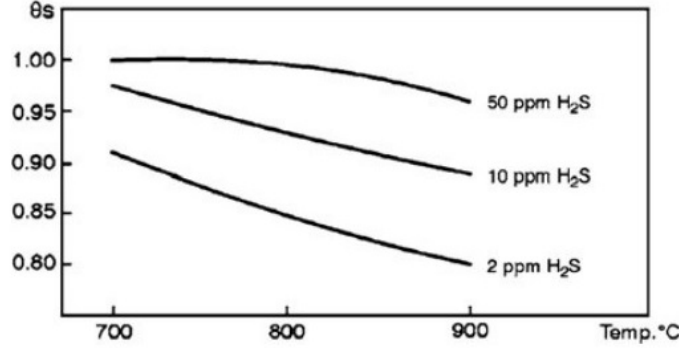
Figure 2.7: Chemisorption of H_2S on N_i catalytic partial oxidation.Shown [18].

Another phenomenon encountered using hydrocarbons is called carbon formation or coking. The different mechanisms are under study but mostly follow these relations:

$$\boldsymbol{SCO_{(g)}- > C_{(s)} + CO_{2(g)},} \tag{2.4}$$

$$\boldsymbol{CO_{(g)} + H_{2(g)}- > C_{(s)} + H_2O_{(g)},} \tag{2.5}$$
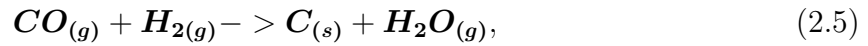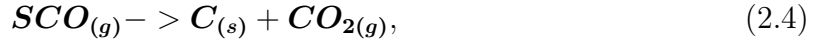
Bouduard reactions [31], say that the electrolysis of CO_2 into Co, or of H_2O/CO_2 into H_2/Co can result in carbon deposition between electrode and electrolyte. This leads to the formation of different carbon types covering YSZ and Ni.
Ni, is an excellent cracking catalyst, and in front of the carbon, activity tends to precipitate on the interface of Ni and YSZ [18]. The hydrocarbons can be steam-reformed either inside or externally as a solution to this issue. The endothermic nature of the reforming process, which results in severe temperature gradients and mechanical failure, is the only drawback of performing it internally. The operation of CH_4 must be distinct with respect carbon monoxide (CO); in fact, in fuel cell mode with CH_4, some carbon deposition could be seen, but in a way less harmful since carbon can grow in the gas channel. Is important to remember that at OCV carbon will deposit, and then if drawing a current, carbon is oxidized, which then will lead to the destruction of the cell. Of course, CH_4 is reformed internally or externally eq(2.6), and then carbon deposition can follow the above equation equation(2.4).

$$\boldsymbol{Ch_4 + H_2O- > CO + 3H_2,} \tag{2.6}$$
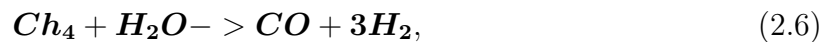
Replacing Ni with Ceria is the most common method of addressing the problem.

Another poisonous element is Cr, which affects the oxygen electrode, this element didn't receive much focus in the research field since it doesn't significantly affect a single cell. Instead, this is not accurate for stacks where Cr poisoning is the most studied phenomenon, where Cr comes from the interconnect materials composed of ferritic stainless steel. Step one of the reaction is the formation of Cr_2O_3, and we got formation of CrO_3 in dry air and $CrO_2(Oh)$ in moist air [31]; those compounds in contact with the oxygen electrode will be reduced and become solid Cr, which will block the 3PB, reducing the electrode performance. This paper then states that chromium poisoning may also occur at OCV but at a lower rate.

A way to prevent this is to cover the surface of the interconnectors composed of chromium-containing steel with a suitable metal oxide, such as $Mn_{1.5}Co_{1.5}O_4$ [31].

The third process involves residual stresses, either at interfaces at small scales or at large scales owing to stack characteristics.

The re-oxidation of the reduced $Ni-YSZ$, usually is detrimental to increasing the volume between Ni and NiO, damaging YSZ [18]. In fact, if fuel supplied is interrupted, the O^{2-} that is reaching Ni, will only oxidize the surface [24]. A way to overcome this problem is using a Ni infiltration on preformed porous YSZ structures, improving redox stability. Still, this method was time-consuming, even if it is an improved method for redox stability.

Another degradation factor is related to the difference in thermal expansion coefficient (CTE) between the electrolyte and the fuel electrode, creating internal stresses. In the paper [18] is reported that the $NiOYSZ$ creates stresses on the electrolyte due to the difference in CTE, that is beneficial for the anode supported cell, thanks to the compression, but is instead detrimental to the electrolyte in the electrolyte supported cell.
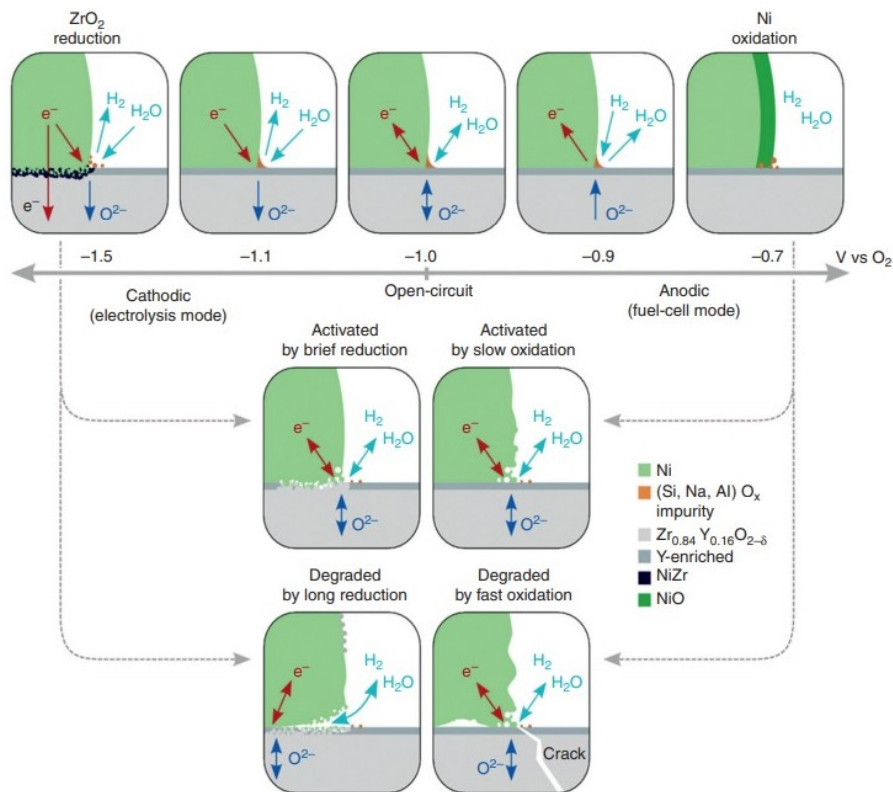
Figure 2.8: Coomonly seen Ni-YSZ fuel electrode-potential-driven activation and degradation phenomena [19].

Figure 2.8 represents the most common potential-driven degradations, the main parameter to describe the thermodynamic state of a given electrode is the electrode potential versus a well-defined reference as Pt/O_2 (1bar O_2, temperature). As written in the figure, we have a voltage that varies if it is in fuel cell mode or the electrolysis mode.

At a very negative electrode potential, the zirconia reduces into Zr metal (ZrO_2), which dissolves in the Ni, and creates tendency of zirconia nanoparticles.
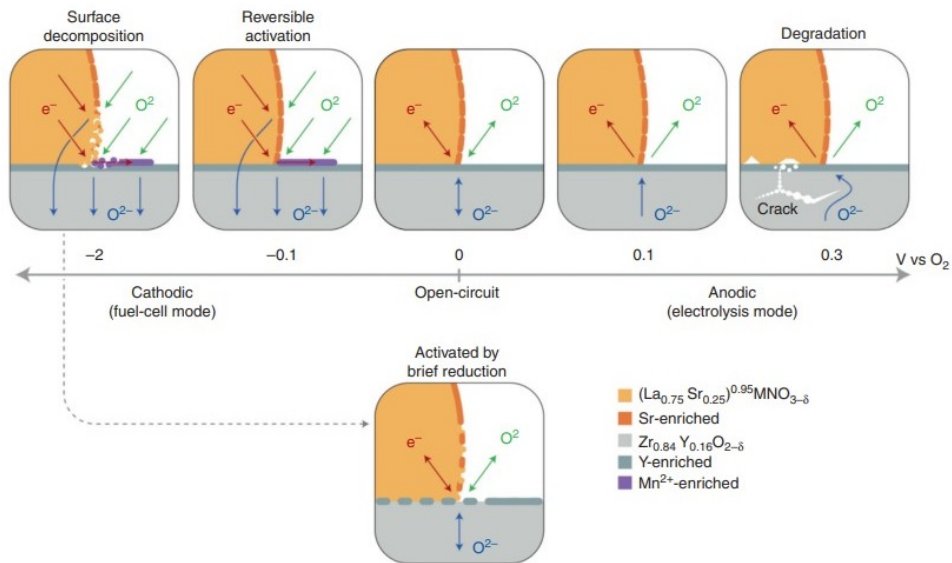
Figure 2.9: Commonly seen perovskite oxygen-electrode-potential-driven actviation and degrdation phenomena [19]

Instead, at a very positive potential, the Ni is oxidized to NiO. As before, short oxidation of Ni may temporarily activate the electrode; otherwise if it is continuous will damage irreversibly [31]. This will create a mechanically destruction of the cermet due to the large volume of NiO compared to Ni. After the re-reduction of NiO to Ni causes the Ni particles to coarsen.

In figure 2.9, instead, is reported the degradation for the air electrode. At the beginning of the degradation there is formation of nanoparticles, those at the beginning will increase the electrode performance. At high positive potential O_2 bubble are formed creating a weakening of YSZ near LSM.

3 | Experimental setup

This chapter aims to describe the test station that was used for short stack testing at the DTU Energy (Rig 85). The station was built up for stacks of Solid Oxide Cells. The station is referred to as ´Rig´ hereby and some are arranged for single cells, and others for the entire Solid oxide stack. This chapter will be divided into the following subchapters: hardware, control scheme, measurement equipment, stack supplier connection.

3.1.   Hardware

The test rig is supplied by the company HORIBA FuelCon AG (FuelCon Evaluator-S number 70623) as shown in Figure 3.1, with the name adopted in the laboratory as ´Rig85´.

Figure 3.1: Stack testing station (Rig85).

The station is controlled by a computer through a software called TestWork (provided by FuelCon), where the instructions to the station are implemented with a code of Visual Basic language. The rig was modified from a module testing rig to stack testing rig. Further details on the modification and hardware are described in the following subsections. The test rig is composed of three main parts. The first one, as indicated in the Figure 3.1, is where the furnace is placed with the stack, then there are different gas lines and the associated auxiliary equipment (heaters, valves etc.), and the last part is the 'brain' of the rig composed of the programmable logic controllers (PLCs) and all the electrical connections.

3.1.1.   Stack

The previous chapters explained how a cell is composed of an anode, a membrane(electrolyte), and a cathode. These nomenclatures are for the fuel cell mode, in electrolysis the anode and cathode would be reversed. Attached to the anode side is a Nickel mesh, represented in Figure 3.2, with the bifunctional aim to collect electrons from the anode reaction providing them to the cathode via the external circuit and an even gas distribution on the anode. Meanwhile, on the cathode side, there is a flow field that is aimed to evenly distribute the gases on the cathode surface and provide the electrons to the next cells for the reduction reaction from the nickel mesh to the cathode reaction.
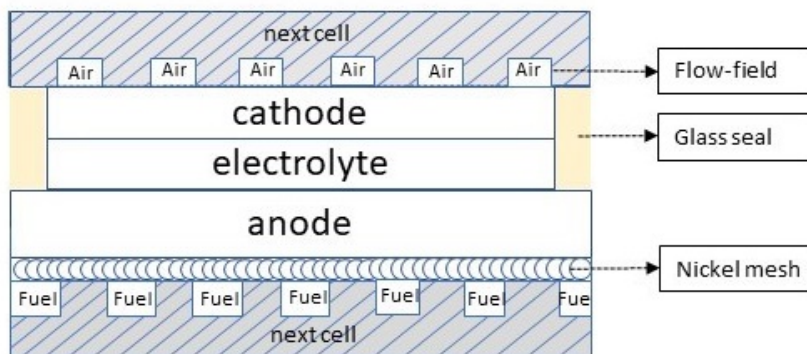
Figure 3.2: Single repeat units composed by cathode electrolyte and anode.

The stack is composed of different cells with interconnects placed one over another (known as Single Repeat Units (SRU)), as represented in Figure 3.3. The SRUs, are stacked under pressure by two end plates and sealed all around thanks to the glass fiber and a metal housing. Two cells are connected through a separator plate that has the bi-functional purpose to be the flow field for the Airside, and on the other side to provide the fuel to anode of the next cell. In addition, the separator plate has the function to provide electrons from the anode reaction of one cell to the cathode reaction to the cell next to

it, spreading them in an optimized way on the surface.
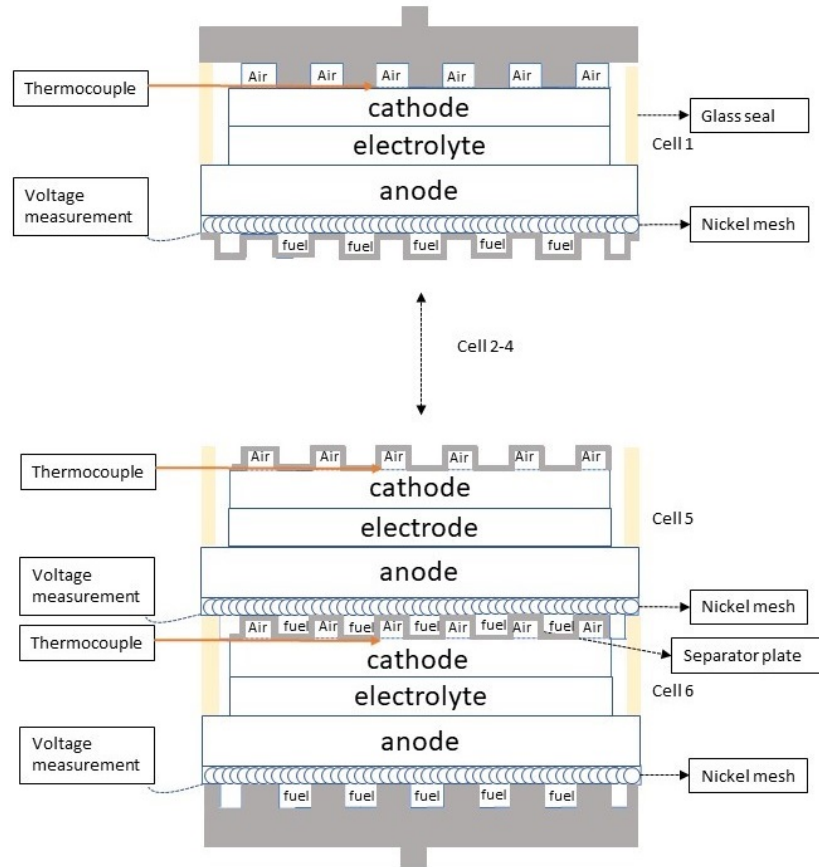
Figure 3.3: Scheme of a Stack with 6 cells.

Each cell has its own voltage connection for the measurement (measured against the ground separator plate), and a thermocouple is seated at different position on the cathode surfaces. The stack is connected to the current by the endplates, one side to the positive and the other side to the negative.
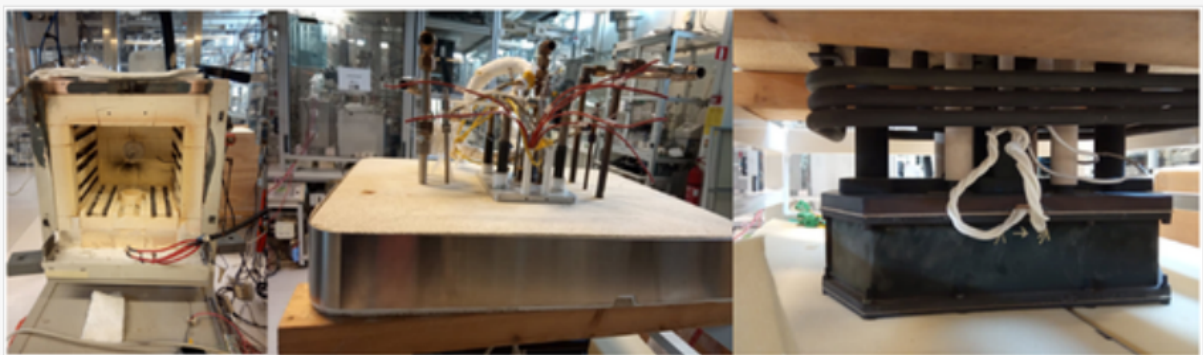

Figure 3.4: Furnace and stack.

All the channels of the airside are connected to an inlet and outlet pipe, and the same happens for the fuel side, the inner pipes have the aim to heat the gasses too as shown in Figure 3.4 on the right. All the pipes are connected to the different cells and, than all the stacked cells are surrounded by a metal box. The stack is placed inside of a furnace which, as shown in Figure 3.4 to heat up and maintain the temperature at the desired values.

3.2.   Control scheme

The Figure 3.5 is a simplification of the FuelCon station with in house modifications done at DTU laboratory to suit the testing requirements. The scheme shows the major components that were used for the testing. Firstly, the two main pipes that are going in and out from the Stack, one is for the Fuel-side and the other is for the Air-side.
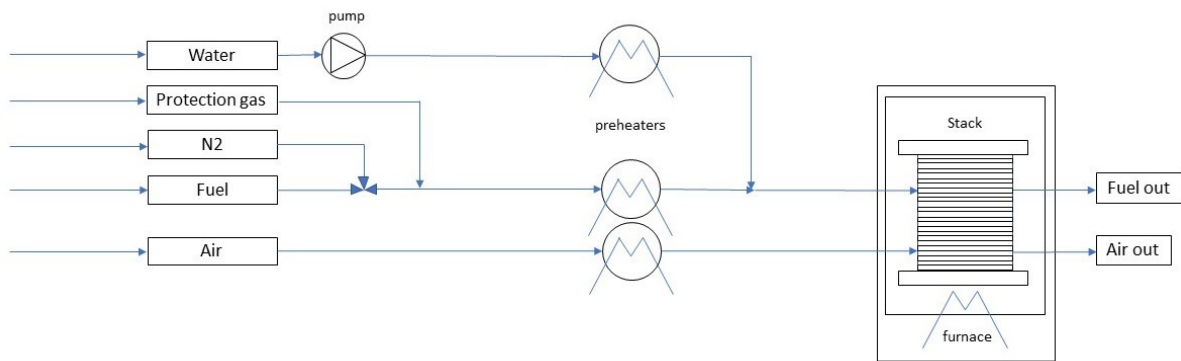
Figure 3.5: Rig scheme for pipes and heaters.

The description will be focused, mainly, on the testing station, then a detailed description of the safety and the complete control will be presented. There are 5 different gas lines provided, as represented from the Figure 3.5. One pipe is for the cathode side where air is fed with an upstream pressure of >6 bar. The air is heated through a preheater before entering the stack to a temperature around 100-200°C below the furnace temperature, to reach at the entering of the furnace a temperature drops around 300°C. The Air then goes into stack and exits at a temperature close to the furnace temperature.
The different gases to the anode side are fed though a mass flow controller with a magnetic valve as a safety measure. In this study, hydrogen and nitrogen were used as the gases for the fuel side (along with steam), because the stack was tested under fuel cell mode for $H_2 - H_2O$ gas composition.
The nitrogen line is provided with an upstream pressure of 12.1 bar, N_2 is used during the

heating up and cooling down procedures exploiting its inert gas property to maintain all systems at a constant temperature. It is also used during the long-term test to maintain a constant total flow rate.

Another pipe line is for the protective gas. The protective gas or ´safety gas´ is commonly used to refer to a particular mixture of nitrogen and a content of 5% of H_2. It is used during the startup for start of Ni reduction in the fuel electrodes and also when a failure occurs, and the different fuels get cut off. This ensure that the nickel does not undergo re-oxidation at these high temperatures ($>600°C$). The flow is provided at 6.9 bar, and this pipe is controlled by a manual ball flowmeter, through a magnetic valve that opens when a fault is detected and the system is set to safety conditions.

The last pipe supplies water to the system and is characterized in series by a pump, a back pressure valve, and an evaporator. The pump provides the system with a precise flowrate, the backpressure valve helps the pump to set the desired output pressure at the pump outlet and ensure there is no back flow from the evaporator. The evaporator is needed to change the state from liquid water to steam before mixing with other anode side gases.

Three additional pipes are provided with methane, carbon monoxide, and carbon dioxide respectively, those are not shown in the scheme, as they are not used in the present test. All the pipes for the fuel side flow through a preheater composed of a heated pipe (to up to 600°C) such that the inlet to the furnace would be close to 300 °C below the furnace temperature. This is crucial also to ensure there is no steam condensation in the pipes before the stack to limit the noise in the measurements.

As we can appreciate from the original FuelCon scheme in the appendix A.1 the water supply is connected to two tanks, one for the Airside and one for the Fuel side to humidify the gases. This system was modified with a pump to reach a higher gas and steam flow rates as shown in the Appendix A.2.

3.2.1. Furnace

One of the main components of the Rig is the furnace, where the stack is placed at the desired temperatures. The furnace is controlled using a Eurotherm Model 3216 as shown in Figure 3.6. It requires two power supplies of 230V AC, one to the controller and the other for the power output to heat up the electric coils. In addition, two thermocouples (S-,N-or k-types are supported) are provided to measure and cut off the temperature based on the maximum limits. The furnace has the possibility to reach high temperatures, up to 1100 °C. The furnace is able to maintain the temperature constant, in this case around 750

°C, ramp up and down for heating and cooling procedures, with a set rate as per manufacturer's protocols (2 °C min^{-1} in the stack tested in this work). Furnace temperature setup is done manually as the furnace was provided by an external supplier. However the safety system based on the furnace temperature is integrated into the Testwork software. The additional features can be read about on [12].

Figure 3.6: Eurotherm Furnace controller.

The furnace is composed of two parts: the power supply that has control of the temperature, the coils and ceramic insulator where the stack are located as reported previously in Figure 3.7. This ceramic material retains the heat to insulate the furnace and Stack inside and has a top handle to open and giving house for the needed thermocouples.

Figure 3.7: Furnace.

3.2.2. Thermocouples

The thermocouples are sensors composed of two different electrical conductors, represented in Figure 3.8, that are joined together at the end and are shielded to separate them from the environment.
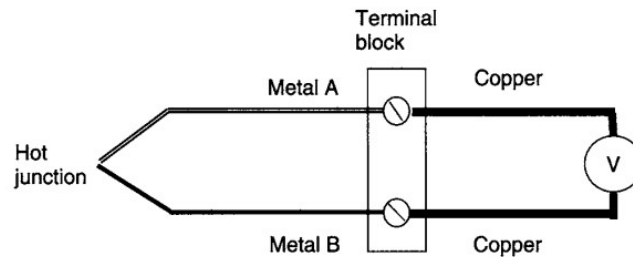
Figure 3.8: Scheme of a thermocouple[9].

It relies on the Seebeck effect that states that, when two junctions are held at different temperatures a thermoelectric voltage is produced. Importantly, to measure this difference a voltage measuring device is inserted in the loop, and then the measurement is correlated to temperature. The thermocouple does not measure the absolute temperature, but the difference between the two metals. The thermocouple wires are composed of different metals compared to the one of the measuring voltage device, and based on the Law of Intermediate Metals [9] 'simply states that a third metal may be inserted into a thermocouple system without affecting the system if the junction with the third metal is kept isothermal´ as we can appreciate from the Figure 3.8.

In the end, to know the absolute temperature of the hot junction, it is required to know the absolute temperature of the reference junction. Two ways are possible: one is to measure the temperature of the junction accurately, using a thermistor or a semiconductor temperature sensor, and the second way is to locate the reference junction in a controlled environment. In our case, we use the first measurement, as we seen from the Figure 3.9

12 different standard thermocouples are distinguished by the type of material, the most common are Type-K, Type-J, Type-E, Type-E, Type-N, Type-S, Type-R, and Type-B.

Figure 3.9: Ambient thermocouple.

The rig uses two main types: Type-K, and Type-N, Type-S for the furnace.

The most common is the Type-K, which is composed of $Ni - Cr$, and $Ni - Al$ (Alumel) metal, which has a general utilization between -180 °C and 1350 °C, and sensitivity is approximately 42 $\mu V/C$ (reference). With a tolerance of +-2.2, reported in [9].

The next thermocouple used is the N-type, which is composed of $Ni - Cr - Si$ (Nicrosil) and $Ni - Si - Mg$ (Nisil) metals and is suitable for use between -270 °C and 1300 °C, and the sensitivity of the type N is $30\mu V/C$. With a tolerance of +-2.2 reported in [9].

In the Appendix B.1 are reported other types of thermocouples.

As indicated in Figure 3.10 the thermocouple differs in the junction mounting. There are three different junctions mounting. The first is the Insulated junction, where the junction is isolated from the sheath and is used for corrosive environments. The second one is called Grounded junction that is used for corrosive environments and high pressure, with a faster response. The last one is the Exposed junction that provides the fastest response and, it is used to measure air and gas temperature.
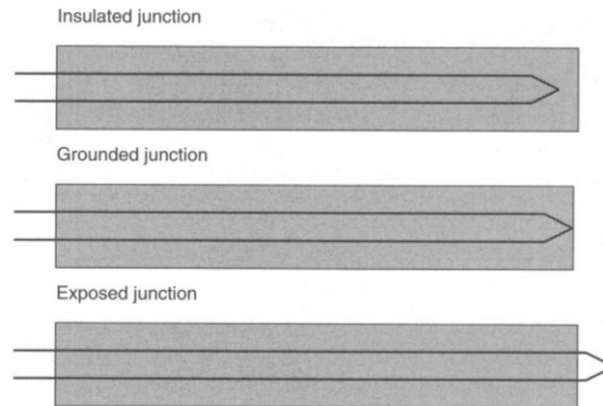
Figure 3.10: Different junctions[9].

The insulation usually is in PVC with a temperature until 100 °C, then there is Teflon with a higher range from -250 °C to 250°C, and the glass fiber till a maximum temperature of 500 °C.

In the rig station, the stack has 6 thermocouples Type-K, that are measuring the different cells, we have a thermocouple Type-K for the evaporator, and we have two thermocouple Type-N for the furnace. The fuel/Air inlet temperature and the fuel outlet temperature are measured by the other three Type-N.

The measurement of the voltage is then corrected since the temperature of the joint reaches 40 degrees due to the functionality of all the pipes, and furnace heat.

3.2.3. Gas lines

The next subchapter aim is the detailed description of the different configurations of the pipes. Each line is characterized in series by a safety valve, mass flow controller, and heater connected in series.

3.2.4.   Hydrogen line
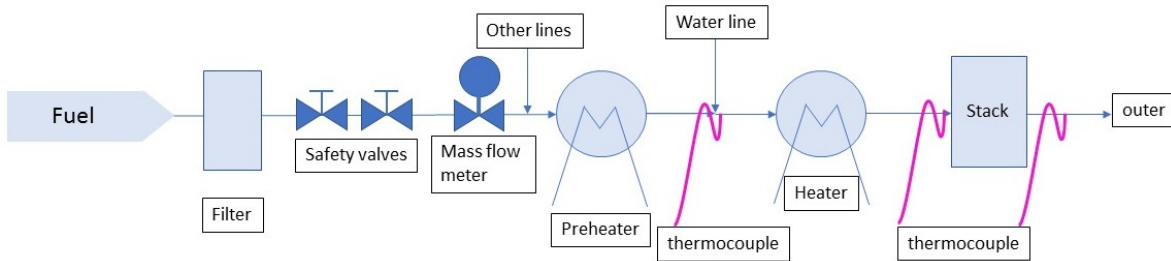
Figure 3.11: Fuel line.

As represented in Figure 3.11, the line for the H_2 is composed in series by a filter provided by DK-LOK Filter [2] and two magnetic valves aimed, to close the pipe when a fault arises (the second valve is for additional safety in case of a failure in one of the valves) and a mass flow controller provided by Bronkhorst [17]. This is interfaced to the computer by the software TestWork (property of FuelCon) where the flow rate can be regulated for the desired amount.

After the mass flow controller is mounted a T junction where the inlet fuels gas are mixed, for example, N_2 or safety gas. A preheater shown in Figure 3.12 is located with the purpose to preheat the gases till 180 °C from room temperature. This value is predefined by the software and is heated using a flexible hose irrespective of flow conditions.

Figure 3.12: Preheaters.

Subsequently, the preheater outlet is connected to the outlet steam line (from the evaporator and buffer tank unit), with a T-junction to ensure uniform mixing between the two fluids. A detailed description of this line is presented in the next subsection.

After the T-junction the gases enter a heater composed by a flexible hose, which will turn the gas to a 200 °C lower than the set point of the furnace, controlled by an external regulator, and thanks to a TypeN thermocouple the temperature is recorded.

Proper insulation of each part of the pipes is crucial (especially in the addition of steam). This is achieved by using glass fiber covered by aluminum foil for preventing any significant loss of heat resulting in condensation of steam.

One of the most important aspects is the safety valve, which closes when a critical alarm is triggered and at the same time opens the protective gas line. The alarm can occur for various reasons, for example (i) when there is a leak from the stack, (ii) deviation of ventilation, (iii) low or high limit in furnace temperature, (iv) or a drop or increase of the pressure etc.

3.2.5. Airline
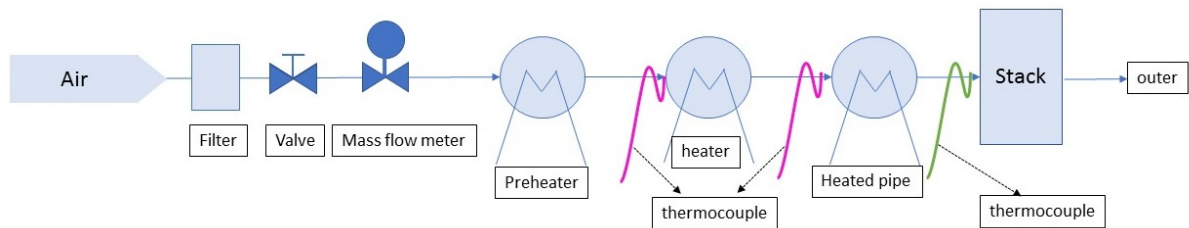
Figure 3.13: Air line.

The Airline is characterized, as is shown in the Figure 3.13, by in sequence a filter, one safety valve, and a mass flow controller provided by Bronkhorst [17], that regulates the amount of flow.

The line is characterized by a preheater that heats up the gas from an ambient temperature to 180°C, (similar to the fuel side) then it is preheated to reach 200 °C below the set point of the furnace. This heater can be controlled with a cascade controller by setting the desired stack inlet temperature or manually by regulation of power to the heater. The regulation is done as a percent of output power desired to achieve the set temperature. The temperature is monitored by a Type-N thermocouple reported in Figure 3.13 in pink. The last pipe between the heater and the Stack inlet pipe is maintained at a constant temperature with an external heated cable that is mounted around the pipe and controlled using a Type-N thermocouple reported in figure in pink, and an additional

Type-k thermocouple in green to record the inlet temperature.

Every part of the pipe is then insulated with glass wool similar to the fuel side to prevent condensation and high temperature gradients between the furnace and gas line.

3.2.6. Safety gas line
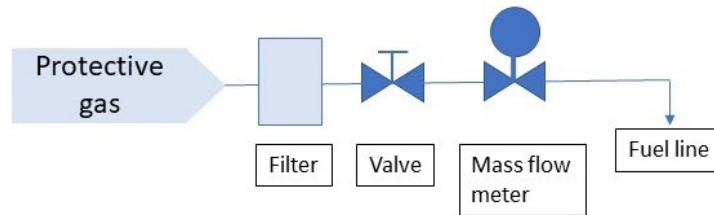
Figure 3.14: Protective gas line

The line of ´safety gas´ is shown in Figure 3.14. It consist of a filter, a valve, and a mass flow controller that is regulated using a manual flow regulator. Before the flow meter, a magnetic valve is mounted which is a ´normally open valve´, so that when a critical alarm occurs, closing all the other fuel lines (power to the valves are cut), the safety gas line inlet opens. After the mass flow controller, the line is connected via a T valve to the main fuel line that was explained earlier.

3.2.7. Nitrogen gas
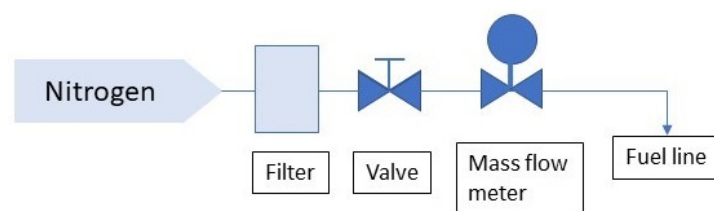
Figure 3.15: Nitrogen line

Similar to the safety gas, nitrogen line is composed of a filter a valve, and a mass flow controller that is regulated to the desired flow rate with the software Testwork. The N_2 line is connected to the other fuel gas lines before the preheater (as explained in the H_2 subsection).

3.2.8.   Waterline

The description of the waterline will follow the Figure 3.16 for simplicity.
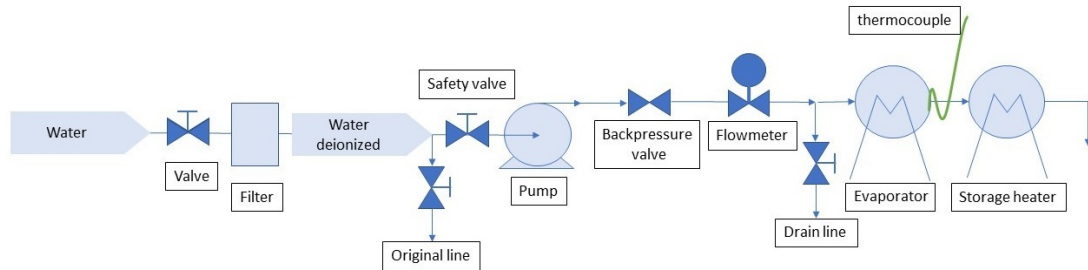
Figure 3.16: Water line.

The water line is characterized firstly by a valve and a filter in series. The filter is a product by Leyco [6] and it is a demineralization ion exchanger. After the filter, the water passes through a T-junction. One of the outlet goes through the humidification tanks (as per the original configuration for the steam supply) and the other line is a bypass to the pump via a safety valve. The pump is a dual piston pump liquid chromatography pump (HPLC) provided by Knauer Azura Pump 2.1S Figure 3.17 which has a regulation between 0.01 mL/min to 50 mL/min [7].
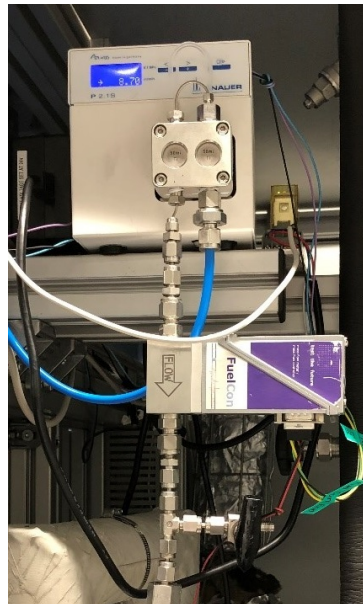
Figure 3.17: Pump and flowmeter.

The outlet pressure of the pump is regulated with a backpressure valve that provides a head to overcome and helps the flow to go in one direction and does not give the possibility

to have backflow. Downstream of the backpressure valve, there is a mass flowmeter that regulates the amount of water flow. A T valve is connected at the downstream of the pump to either direct the flow to a drain line (to purge the line) or an evaporator. The evaporator has a temperature controller to maintain the temperature at 150-200 °C. The temperature is with a Type-k thermocouple. The outlet of the evaporator is connected to a heated buffer thank to regulate the outlet pressure desired to the stack. This is maintained with silicon based heating line at 200 °C. This pipe then leads to the fuel line through a T connection (as described before).
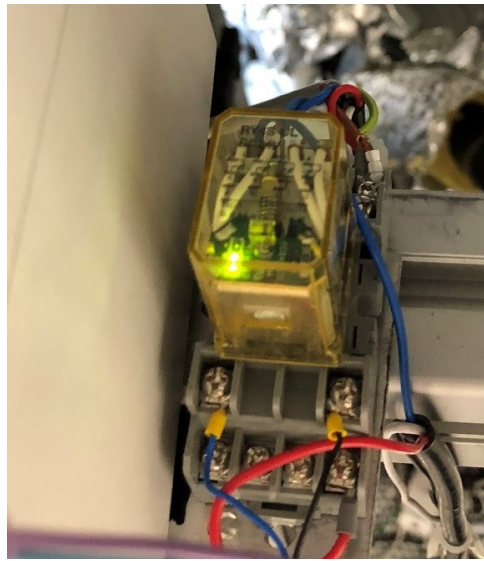
Figure 3.18: Relay that controls the pump's power.

For safety reasons, the magnetic valve and the pump are connected to a relay that will close the circuit only when the hydrogen valve is open Figure 3.18. When hydrogen flow is cut off it will cut the 24 V supply to the magnetic valve of the water and the power supply of the pump. This ensures that there is no incorrect build up of water in the inlet lines and stack during a power failure or other malfunction. An additional safety system was added, composed by an extra relay Figure 3.18 that controlled by a script that was implemented to ensure of maintaining the temperature of the evaporator and the inlet fuel pipe temperature higher then 110 °C degrease otherwise switching of the pump. This implementation was needed for facing any additional short circuit or reduction of temperature below the evaporation temperature.

3.2.9. Electric circuit
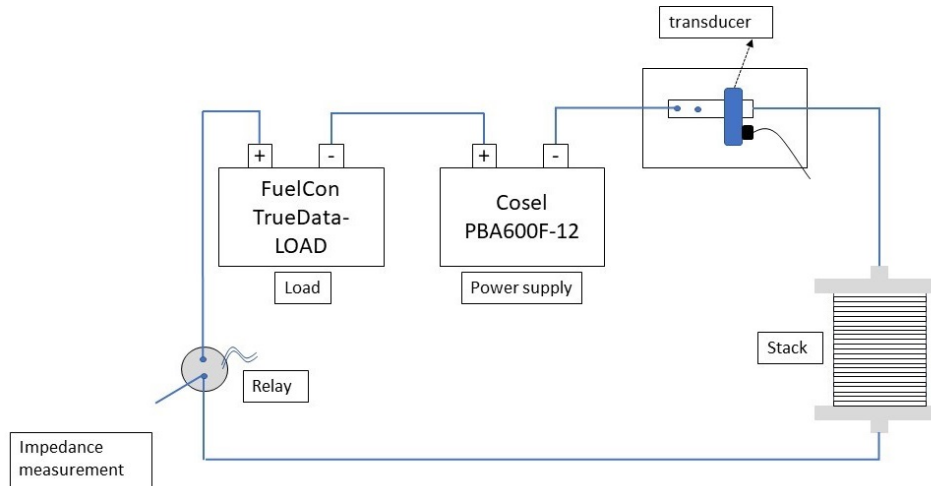
Figure 3.19: Electric circuit.

As is represented in the Figure 3.19, two cables are connected to the Stack one on each side that are one positive and one negative. One line is connected to a relay, and one is connected to a transducer, then the circuit will close within a series of a power supply and a load.

The relay has the aim to switch off the branch of the load and power supply and connect the line where all the equipment for impedance measurement is switched on. The next chapter will be explained this in more in detail.

The transducer is a LEM 200-S Ultrastab, that measures the current by sensing the magnetic field generated by the current passing through.

Cosel PBA600F-12 is a power supply that is needed if electrolysis mode will be on, in fact, provides DC current to the Stack, with a max output power of 600 W, and output current of 53A, and output voltage of 12V.

The FuelCon TrueData-Load [11], are cascade electronical DC load modules with the maximum continuous power of 600 W, that will dissipate the power generated by the stack, in fuel cell mode.

3.3. Measurement Equipment

This section describes the frequency response analyzer system, the additional equipment, and the associated electric circuit. In Figure 3.20, the different instrumentation for the impedance characterization is shown and further detailed explanation is provided in the upcoming subchapters.
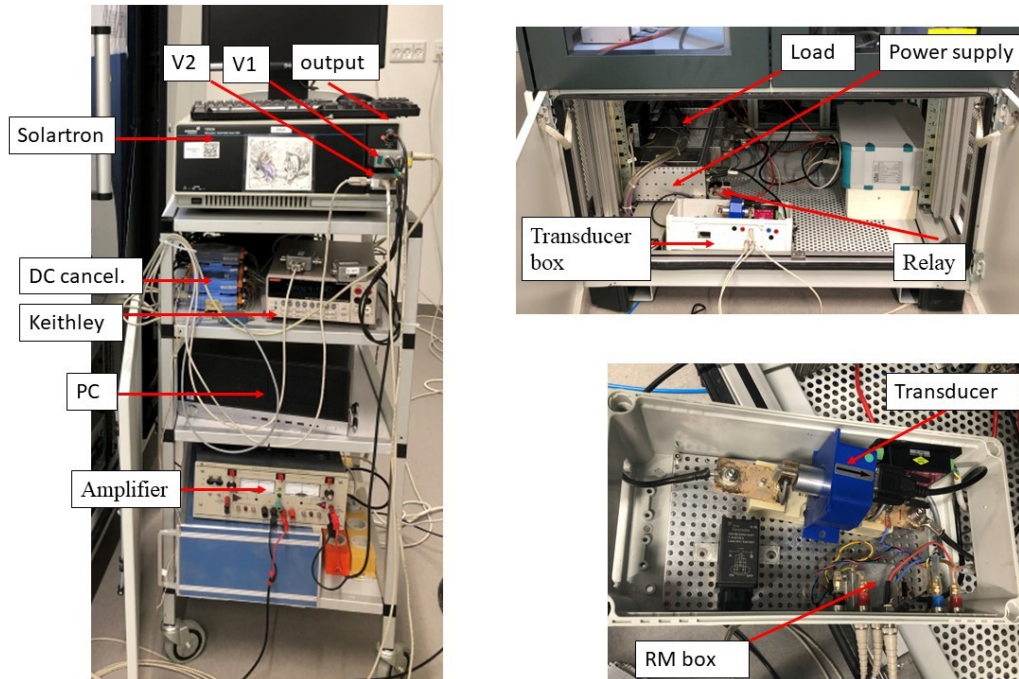
Figure 3.20: Different componenet in the impedance measurement.

The Frequency response analyzer is used to measure the complex impedance under excitation with a sinusoidal AC current at different frequencies, the main equipment is reported below.

3.3.1. Solartron 1252 A

The Solartron 1252 A is a frequency response analyzer, with a large frequency range between 10 µHz to 300 kHz [8], and the maximum voltage excitation is 3Vrms. The input voltage ranges are 30mV, 300mV, and 3V, with a resolution of $1\mu V, 10\mu V,$ and$100\mu V$, respectively. The best input range is 30mV and can be done by reducing the input voltage by applying the DC cancellation circuit. This device has two main purposes, to excite the system with an alternating input and to read the voltage measurement [8].

3.3.2. Kepco

The Kepco BOP 50-2m bipolar is an operational amplifier that can be used to provide dynamic voltage or current in all 4 quadrants. It is a 200 W amplifier with a max current of 4A and a max voltage of 50V. In this work, this device has as an input voltage from the Frequency Response Analyzer (Solartron) and an output as current in a range between 0 and 4 A. In [4] is reported as the datasheet of this device.

In the datasheet is reported that the slew rate (rise time, tr) is $25\mu sec$, for the rise and fall time for the current, which insert in eq.(3.1) gives a bandwidth of around 14Khz that has to be taken in account due to the reduction of the magnitude at higher frequencies, after the bandwidth.

$$f_b = \frac{0.35}{t_r}. \tag{3.1}$$

This means that the current response decreases increasing the frequency and has to be remembered to understand the different behavior of the impedance. Even though, the impedance can still be calculated thanks to the current transducer present in the circuit. This is going to be explained in detail in the next subchapter.

3.3.3. Electric circuit

As explained in the previous chapter, the Electrochemical Impedance Spectroscopy imposes a sinusoidal/voltage to the amplifier that converts into current and the corresponding sinusoidal/voltage response from the stack is recorded. The phase shift results in responses over different frequencies, between 0.1 Hz, and 98600 Hz to identify different physical processes. The frequency response analyzer measures the voltage response of each cell and calculating the current passing through the system with a transducer. It is possible to calculate the impedance, with this eq.(3.2).

$$Z = \frac{V}{I}. \tag{3.2}$$

To calculate the current, it is used normally a known resistor called Shunt, and according to the inverse of the eq.(3.2) measuring the voltage, it is possible to calculate the current. In this system instead is used a transducer due to the high DC current imposed, where metal strip resistors are not suitable.
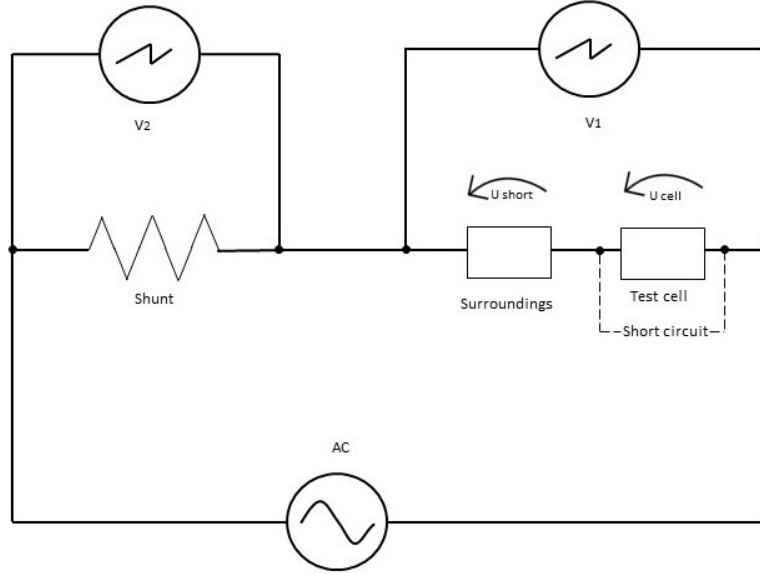
Figure 3.21: Impedance electric circuit

From the Figure 3.21 there are two measurements of the potential needed: one over the R shunt, called V1, for calculating the current flowing into the system, and one measurement is over the Test cell and the surrounding, called V2.

In the next paragraph are reported the mathematical passages for the impedance calculation.

$$Z^*_{cell} = \frac{V_1}{I_{cell}} \tag{3.3}$$

$$I_{cell} = \frac{V_2}{Z_{shunt}} \tag{3.4}$$

$$Z^*_{shunt} = \frac{V_1}{V_2} \times Z_{shunt} \tag{3.5}$$

$$U_{cell} = V_1 - U_{short} \tag{3.6}$$

$$Z_{cell} = (\frac{V_1}{V_2} - \frac{U_{short}}{V_2}) \times Z_{shunt} \tag{3.7}$$

The Solartron according to these equations 5 sinusoidal current to the amplifier that excites the Stack, and the other two main goals are to measure V1, and V2.
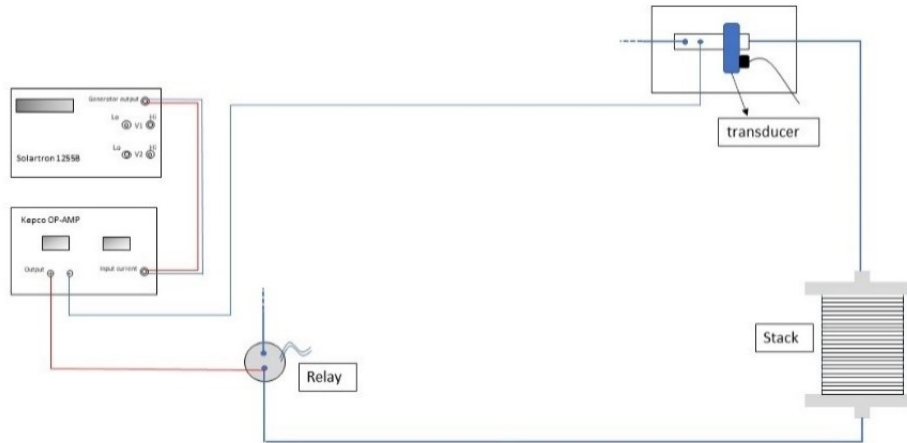
Figure 3.22: From Solartron output to stack.

In the Figure 3.22 the electric connections for the solicitation of the stack is reported. When the relay is open, i.e., when the impedance measurement are performed. Solartron sends a sinusoidal voltage signal at different frequencies to the Kepco amplifier, which amplifies and translates into a sinusoidal current. This fluctuation is connected to the Stack passing through a transducer that will measure the current thanks the correlation between the magnetic field generated and the current flowing, following eq.(3.8).

In Figure 3.24 is reported the measurement from the Solartron V2, to evaluate the current. As reported above in eq.(3.4) to calculate the current flowing, a transducer records a corresponding voltage based on the conversion value and is read at the Solartron at input V2. The connection between the Solartron and the transducer is through a Rm box, and a Dc cancellation box, as reported in the scheme.
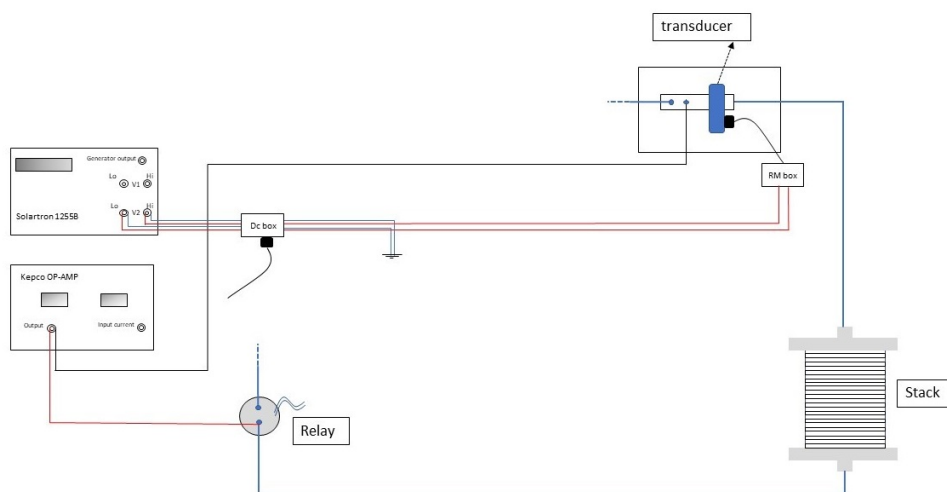
Figure 3.23: Electric scheme for measurement V2.

The Rm box [33] gives the value of the voltage Urm correlated to the magnetic field created by current flowing through the transducer. To calculate the current it is used this equation:

$$I = \frac{Urm}{Rm} \times Kn.$$ (3.8)

Where Kn is a constant value Kn=1:1000 [5], then to the wires is added the Dc cancellation box that has the purpose to remove the Dc component of the signal. The DC voltage in the differential mode needs to be canceled to have the voltage in the lowest range at the input of Solartron, which is 30mV that has the highest resolution.

The Figure 3.23 reported below, represents the connection between the Solartron input, V1, connection, and the measurement of every single cell.

Figure 3.24: Electric scheme for measurement V1.

The Keithley 2750 multiplexer, a CMR box, and the dc box are connected in series.

The Keithley 2750 [3], is a device that allows to switch between different channels that are connected to different cells.

The CMR box, common-mode rejection, is an active circuit that cancels the common-mode voltage given by the difference between the two red cables, expressed in eq.(3.9), and gives back the measure of the single repeating units in Sofc stacks [33].

$$V_{out} = V_{high} - V_{low}.$$ (3.9)

The ground cables, called shields, are placed to avoid interference with other electromagnetic sources, and then the screens of these shielded cables are connected to each other

in a common node in a star way.

The dc box and the CMR box are placed in the same circuit, designed at DTU Energy conversion which minimizes the common-mode voltage and cancels out the dc contribution for utilizing the best resolution on the voltage input provided to the Solartron V1, as explained in the subchapter above.

3.3.4. DC cancellation

The dc cancellation is fundamental because Solartron has the maximum resolution in the range of +-30 mV [8], but without the dc cancellation the AC responses for cells are generally only a few mV at a generator current of 60 mA. Adding 1 to 2 V Dc bias to it, forces the Solartron to choose the 3V range with a resolution of $100\mu V$ compare to 1 µV with range of 30mV [33].

Under the impedance measurement trolley is placed the equipment to apply the Dc cancellation, Figure 3.20. Every measurement is then reported through a GPIB connection to a computer reported in Figure 3.26, through an interface developed by DTU energy called Elchemea 6.0.4.

3.4. Communication interface

This chapter describes the different connections between the equipment and the PCs, which are going to be divided into the two softwares used: TestWork, and Elchemea, with an additional focus on the pump regulation.

3.4.1. TestWork

FuelCon AG provided a software called ´Testwork´, to control and add changes to the Rig85, which is connected to the ´rig´ thanks to a LAN communication through a PLC, in Figure 3.25 is reported the main page, during manual operation.
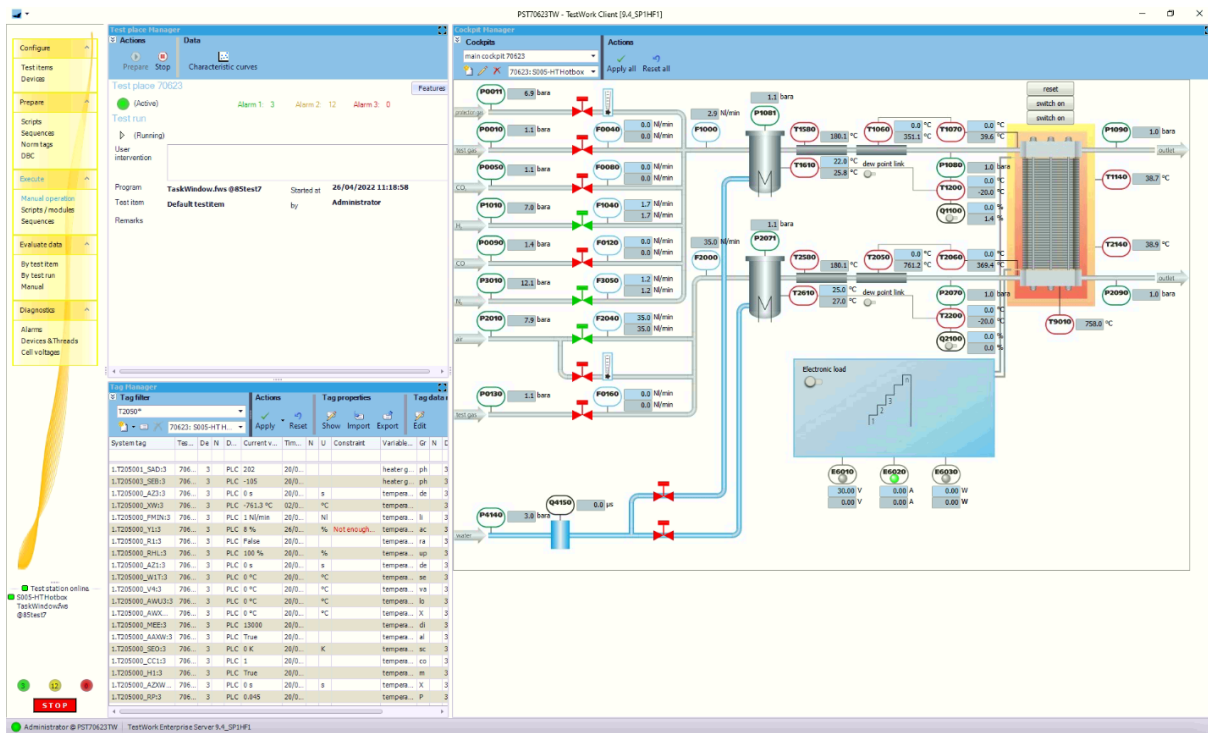
Figure 3.25: Screenshot of Testwork.

In this figure is represented the cockpit manager where it is displayed the scheme of the
´rig´ with all the main pipes, and a scheme of the Stack and the furnace on the right.
Fundamentals are the different tags example P2010 that indicate the different tempera-
tures or pressure, or flow rates measured in the various points of the rig. This software
gives the possibility to open and close the different valves and regulate the flow rate for
each pipe through the masses flow meters.

Instead, the old water pipe, is still present in the display, even though there was an update
on the line. On the left is present a menu with the different categories. The mains are:
Configure, Prepare, Execute, Evaluate data, and Diagnostics.

The main category is Execute where it presents two main subcategories: Manual oper-
ation, where is present the simple scheme and the Tag Manager, where it is possible to
look on specific tag, and then there is Script/modules where is possible to run the desired
script.

Another important category is the Alarm, where are listed the different alarms with three
different colors: green, yellow, and red, in base of the importance.

The critical alarms are shown as red alarms, which will switch off the gases and power
supply to the rig is cut off, and runs on safety gas and air controlled through the manual
ball valves. These alarms appear if for example the temperature limits of heaters of fur-
nace, if there is a ventilation alarm due to the open of the main doors of the rig, due to

some leaks, sensor calibration errors etc.

The tag reported in the task manager defined for example of T2060, is defining a thermocouple. FuelCon record every parameters every minute in this way it is possible to understand the different behavior of the cell during the changes in temperature and other parameters. Important is to remember which tags control which parameters, such as temperature or pressure.

The last important category is under Evaluated data under Manual, which is reported a brief diagram of the voltage cell, the temperature of the furnace, the temperature of the Stack, cell voltage, flows, and pressure air, and other less important parameters, all those are represented during the time.

3.4.2. Elchemea 6.0.4

Elchemea, is a software developed by DTU Energy that is connected thanks to a GPIB connection to the Solartron trolley, and records the difference impedance and voltage for the IV curve, reported in Figure 3.26 the main page of this software.
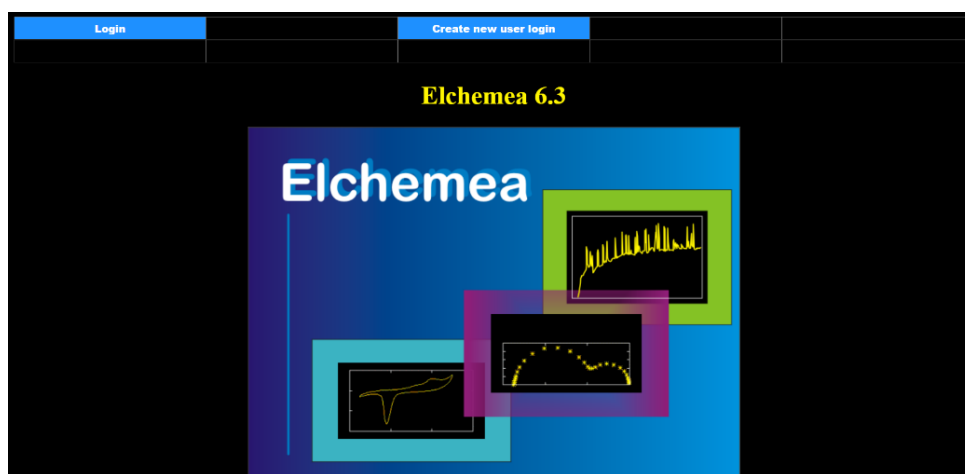
Figure 3.26: Elchemea.

3.4.3. Water Flowmeter

The flowmeter after the pump in the water line, was added to measure the exact flow rate of water passing and going through the evaporator.

This is connected externally not through the LAN and TestWork but uses a connection RS323 connected to the computer that will open a communication channel through a software called FlowDDE and can display and count the flow in time thanks another software called FlowPlot. The valve of the flow meter is naturally closed so before opening

the pump needs to be open the connection otherwise the fluid will not pass. Here reported the Figure 3.27 of the Flow meter.
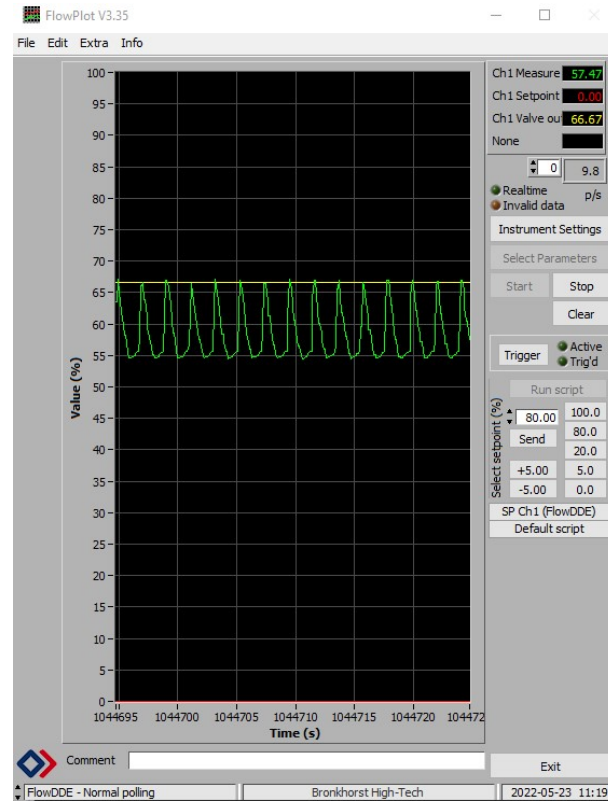
Figure 3.27: Water oscillation from FlowPlot.

4 | Methodology

This chapter will describe the different instruments used for evaluating the cell. It is divided in different subchapters: Nernst equation, impedance spectroscopy, and then the I-V curve.

4.1. Nernst equation

The open circuit voltage is the reverse voltage that the cell reaches in ideal conditions. The deviation between OCV value and the Nernst equation can be related in the function of feed gas composition changes, gas pressure difference, and unexpected operating temperature.

The Nernst equation for the hydrogen-oxygen fuel cell reaction is expressed in eq (4.1).

$$U_n = E_{Nernst} = E^o - \frac{R_g T}{nF} \ln \frac{\prod x_{products}^{v_i}}{\prod x_{reactans}^{v_i}} \tag{4.1}$$

$$U_n = E_{Nernst} = E^o - \frac{R_g T}{2F} \ln \frac{x_{H_2O}}{x_{H_2} x_{O_2}^{1/2}} \tag{4.2}$$

Where R is the gas constant, n is the number of electrons, F is the Faraday constant ai is the activity of species and vi is the stoichiometric coefficient of species, and x is the molar fractions for the species. To calculate the Nernst equation needs the electrochemical reaction; in fuel cell case, the equations are reported below:

$$2H_2 + 2O_2^- -> 2H_2O + 4e^- \tag{4.3}$$

$$O_2^- -> O_2 + 4e^- \tag{4.4}$$
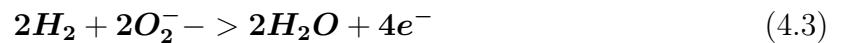
The theoretical OCV can be computed so as:

$$OCV = E^o - \frac{RT}{2F} \ln \frac{a_{H_2O}}{a_{H_2} a_{O_2}^{1/2}} \tag{4.5}$$

The approximation as fuel and air as ideal gasses will lead to the simplification of activity to the ratio of partial pressure of the component and reference pressure (1 atm).

$$a_i = \frac{P_i}{P_{ref}} = x_i \frac{P_{tot}}{P_{ref}} = x_i P_{tot} \tag{4.6}$$

The stack is at 1 atm, so the OCV theory is calculated as:

$$OCVtheory = E^o - \frac{RT}{2F} \ln \frac{x_{H_2O}}{x_{H_2} x_{O_2}^{1/2}} \tag{4.7}$$

Eo is defined as -DeltaGo/(nF)

4.2.   Electrochemical impedance spectroscopy

This section will describe the theory of electrochemical impedance spectroscopy, which is deemed a powerful tool for the characterization of electrochemical systems. Electrochemical impedance spectroscopy (EIS) gives information on the various losses experienced by electrical equipment according to different frequencies. The power of this tool is the use of sinusoidal oscillation at a different frequency, which is perfect for studying a complex system; in fact steady-state polarization curves are not enough since is going to identify just a single rate-determining step. The dynamic behavior of the physic and chemical processes affects the internal resistance in an extensive range of frequencies.

As reported in Figure 4.1, slower processes have a time constant from minutes to hundreds of hours. Instead fast processes have a relaxation time between microseconds and tends of a second.
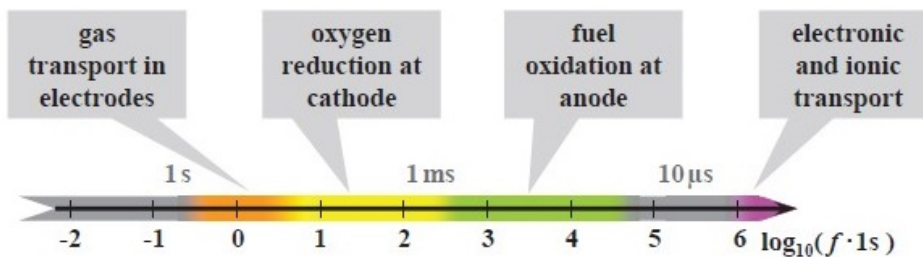
Figure 4.1: Dynamics of a SOFC:Characteristic relaxation frequencies f of the individual electrochemical loss mechanisms occurring under operation of an anode supported SOFC [25].

The cell voltage U_{cell} deviates from its equilibrium value under open-circuit conditions

anytime an electrical current I_{load} flows through an electrochemical cell. Knowing the cell current I_{load} and the overvoltage $U_{pol} = U_{OCV} = U_{cell}$, a polarization resistance R_{pol}, can be calculated for the system. In this case, there are different chemicals and physical processes, which will lead to a nonlinear relation between the read voltage and current.

In an Ac input current signal, the definition of the polarization resistance is more complicated then Dc. In fact, a complex impedance value Z_{cell} can be assigned to the system coming from the phase-shifted respect to the perturbation input of the AC voltage signal detected at the cell's terminals and the perturbation current input.

Due to the nonlinear behavior, the system is not just dependent on the frequency changes but depends on the amplitude changes too, so it is fundamental to keep the perturbation amplitude sufficiently small.

To evaluate the EIS is performed as in Figure 4.2, and follow these steps.

1. Operates the cell in steady state condition, which can be open circuit voltage, constant current ecc

2. Apply a sinusoidal current to the steady state condition $i(t) = iosin(wt)$ with a small amplitude

3. The voltage at the terminal is measured $u(t) = uo(w)sin(wt + fi)$, presents the same frequency, and a phase shift with respect to $i(t)$. In Figure 3.27 is reported the trends of current

4. The impedance is, then, calculated from the ratio between the complex variables of voltages and current eq(4.8).

$$\boldsymbol{Z(w)} = \frac{\boldsymbol{u(t)}}{\boldsymbol{i(t)}} = \frac{\boldsymbol{u_o(w)}}{\boldsymbol{i_o(t) \times \exp\left(ifi(w)\right)}} = \boldsymbol{re(z(w)) + jim(z(w))} \qquad (4.8)$$

$w = 2 \times pi \times f$ represent the angular frequency, and fi is the phase shift.
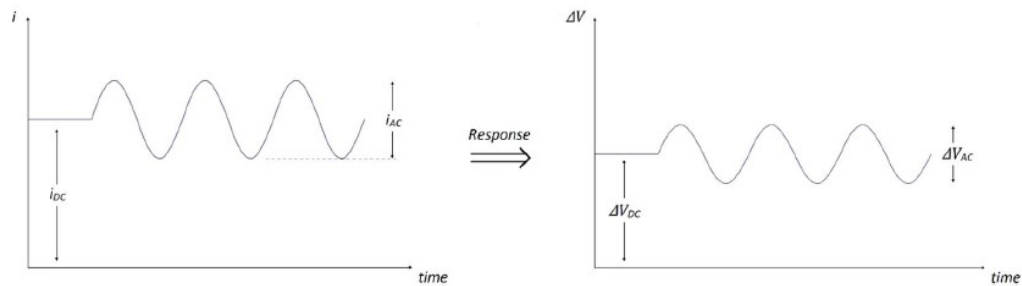
Figure 4.2: Current and voltage response during EIS

5. Then the results are reported in different diagram.

The frequency range varies between discrete values, and the recorded impedance values are plotted in a complex plane called the Nyquist plot, or can be plotted in the Bode diagram composed of imaginary impedance in the function of the frequency figure. In the two plots, the imaginary parts are reported with an opposite sign because most of the behaviors are capacitive.

Figure 4.3 shows an example of the Nyquist plot for a SOFC with content 20/80 at 700°C, where on the y-axis is present -immaginary impedance, and on the x-axis is present the real part.
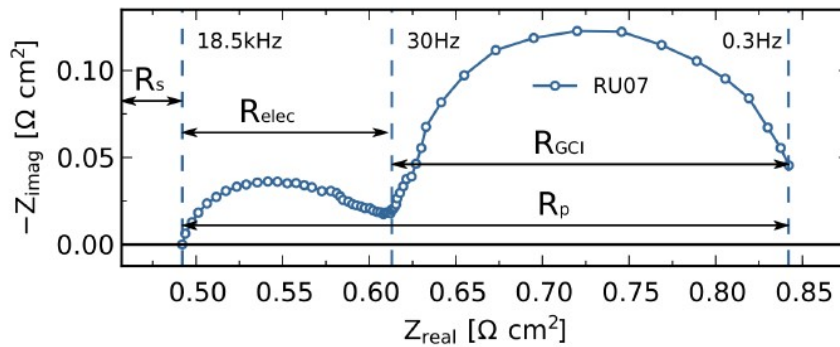
Figure 4.3: Nyquist plot for a SOFC with content 20/80 at 700°C.

In this Figure 4.3 the high-frequency intercept with the real axis corresponding to Rs, ohmic resistance. The intercept of the low frequency with the real axis is called ASR, and it is identical to the slope of the I-V curve at the given operating point. The difference between ASR and Rs gives Rp, that is, the polarization resistance.[46]
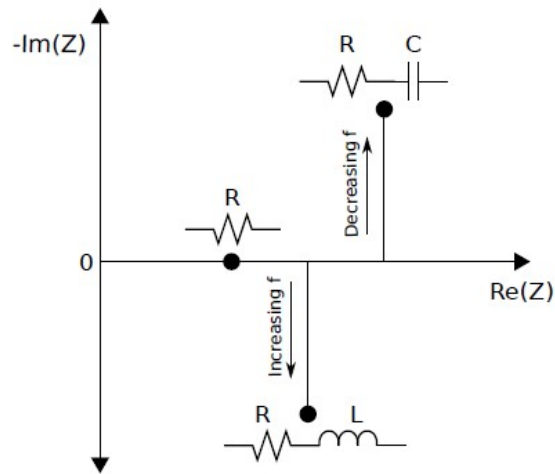
Figure 4.4: Different electric elements to simply the EIS.

Further study will lead to a deep analysis of the Nyquist plot[42], using a model that will simplify the system thanks to an electrical circuit with different elements. This system can be simplified with different connection of resistor, capacitance and inductance [45], as it is appreciable from Figure 4.4, to identify the different contributions of specific phenomena. For instance, the solid electrolyte can be considered as a series of a resistor and capacitance in parallel. This analysis wasn't the focus of this thesis, and it was decided not to adopt any model to analyze the EIS [26, 41], just using the ohmic resistance and the polarization resistance thanks to the fitting of the data using a polynomial equation. To identify the different phenomena instead, is used the bode diagram, which identify the peaks changes at the different conditions, these different frequencies are related to different phenomenon as gas transport in the electrodes, cathode/anode reactions, and ion and electron conduction thanks to the variation of single parameters. In this work, the identification of the different phenomenon are related to literature of the same cell because this wasn't the aim of this work.

4.3. Polarization curve

The polarization curve or I-V curve is another tool that is used to study the electrochemical system, this curve shows the electric energy, according to the potential difference between the two sides of the cell, relating to a specific current imposed. An example is reported in Figure 4.5 in fuel cell mode.
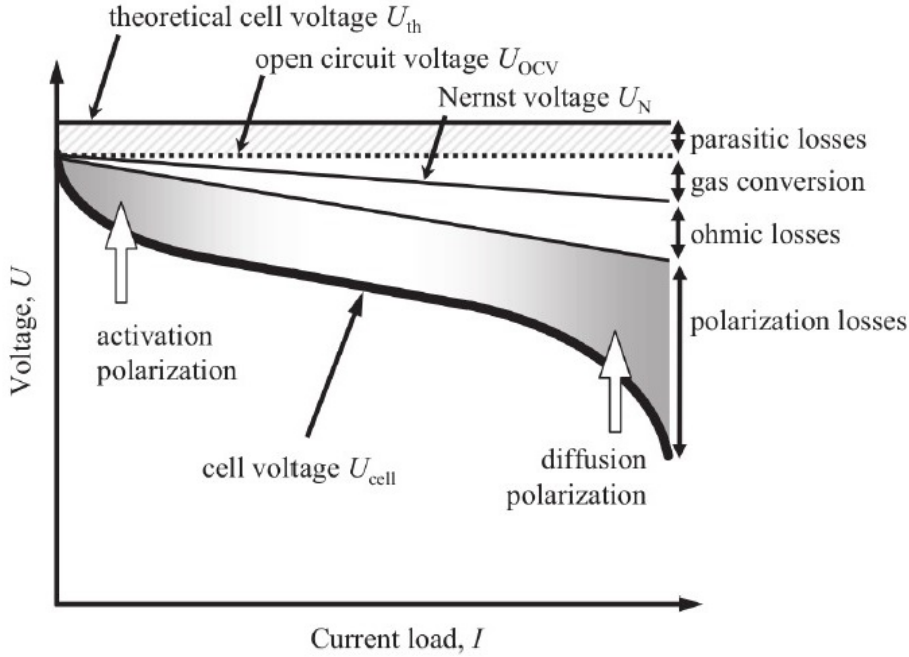
Figure 4.5: Schematic representation of the current-voltage characteristics of a SOFC. The individual loss processes cause a decrease in cell voltage with increasing current.

The curve is measured by imposing a step increase of the current and measuring the voltage terminals. This curve represents the losses when the current is applied. The first information from the curve is the difference between the voltage, calculated with the Nernst equation, and the voltage at OCV, which is caused by the fuel and oxidant crossover, or temperature changes. Based on previous experimental observations, the allowed OCV divergence between the observed value and the predicted one is roughly 10 mV, which compensates for system imperfections as well as minor variations in temperature and feed composition with regard to the nominal ones.

Further voltage losses occur when the current is drawn, and the curve can be divided into two regions. The first losses are ohmic losses; the second is the polarization losses. Ohmic losses are related to the electrodes' electrical resistance, the interconnects' contact sites, and the resistance brought on by ions' conduction through the electrolyte. The polarization losses are divided into the activation polarization losses, related to charging transfer reaction at the electrodes and are strongly dependent on the exchange current density, and then concentration-diffusion losses, related to the mass transport limitation in the electrode structure for gas diffusion and conversion [33].

The cell voltage with all the different losses is expressed by eq (4.9).

$$U_{cell} = U_{th} - \eta_{act} - \eta_{ohmic} - \eta_{conc} \tag{4.9}$$

The loss related to the electrolyte has an ohmic nature and influences in the middle region of the plot. Instead, the loss connected to the electrodes are for the activation of the reaction, and concentration of reactants at TPB is influencing the first part related to the low current density. Instead, the curve at high current is associated to the limitations given by reactant concentration.

Another important parameter is ASR, which is defined as the total cell's resistance, and it can be measured from EIS, or I-V curve. In fact, is calculated following this eq(4.10) as the derivative of the curve at a current of interest.

$$ASR = \frac{\partial u_o(w)}{\partial i_o(t)} \tag{4.10}$$

Also available from polarization curve data is the power curve, where power density is simply calculated as the product of voltage and current density.

5 | Results analysis and discussion

This chapter discusses the test procedures and results for two ASC stacks. The tests were performed on two stacks assembled by SolidPower, as shown in Figure 5.1. The stack on the right is composed of DTU cells and then assembled by Solidpower. Instead, on the left is the stack built entirely by Soldpower. Both stacks are composed of anode-supported cells (ASC).

(a) Stack A.

(b) Stack B.

Figure 5.1: Photo of the two stacks tested, Stack A tested for 500h, Stack B tested for 1400 h.

Cells were characterized by polarization curves and EIS spectra. This provides an understanding of the system behavior during the testing period.

The first analysis was carried out on the first stack, $\boldsymbol{stackA}$, composed of 6 cells, entirely made by Solidpower. The second analysis was performed on $\boldsymbol{stackB}$, composed of DTU cells, and assembled by Solidpower. This chapter is divided into electrochemical characterization at standard conditions pre and post-durability testing, durability performance of the two stacks, and finally, comparison with single cells. In addition, during the tests, the stacks faced interruptions that are further described in the upcoming sections.

5.1.   Stack A

5.1.1.   Initial Electrochemical characterization

This section describes the results of stack A, with 6 Anode Supported Cells (ASCs) composed of $Ni - YSZ$ anode ($250\mu m$ in total), then a dense YSZ electrolyte layer ($8 - 10\mu m$) a CGO barrier layer ($5\mu m$) and an LSCF-CGO air electrode ($50\mu m$) [35]. The purpose of this test was to study the stack performance under high steam content for $500h$ at OCV. Cells form the same manufacturer has been previously studied [35].
The electrochemical characterization was performed for all cells of the stacks through I-V curves and EIS spectra at OCV at a temperature of 753°C. The temperature was considered at the outlet of the Air side as suggested by the Solidpower company.
Table 5.1 summarizes the initial conditions under which the stack was tested. The initial procedure was composed of three I-V curves, the first two were at dry H_2 on the fuel side, and then the flow rate on the Airside was increased. The third I-V curve was recorded with 60% steam on the fuel side. Afterward, two EIS were recorded at 60% and 90% steam, and then an I-V was registered at 90% steam.

tests	H_2 **L/min**	**Steam L/min**	N_2 **L/min**	**Air L/min**
I-V 100	1.7	-	1.2	16
I-V 100	1.7	-	1.2	32
i-V 60/40	1.7	0.953	1.2	35
EIS 60/40	1.7	0.953	1.2	35
EIS 10/90	1.7	13.07	1.2	35
I-V 10/90	1.7	13.07	1.2	35

Table 5.1: Tests initial characterization

Figure 5.4 compares the I-V curves for the stack's six cells at different steam concentrations at T 753°C. 60/40 H_2/H_20, 10/90 H_2/H_2O, and 100% H2 with no humidification Air in Airside.
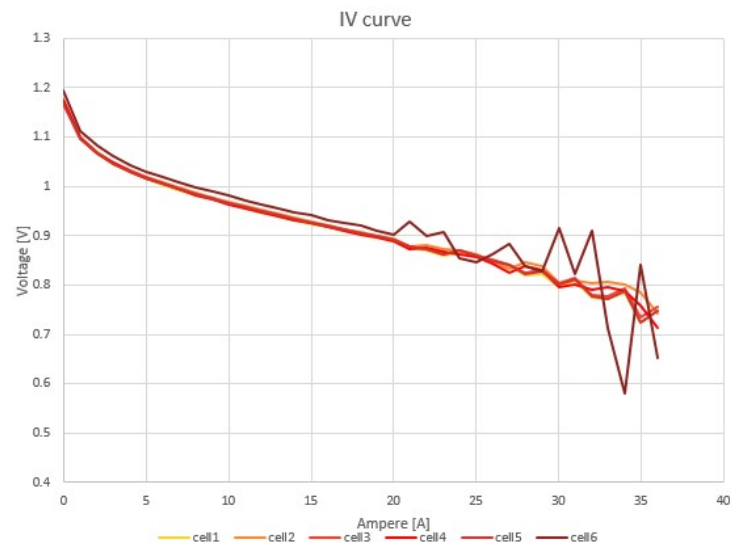
Figure 5.2: Polarization curves with composition 100 H_2 at a T 757°C.
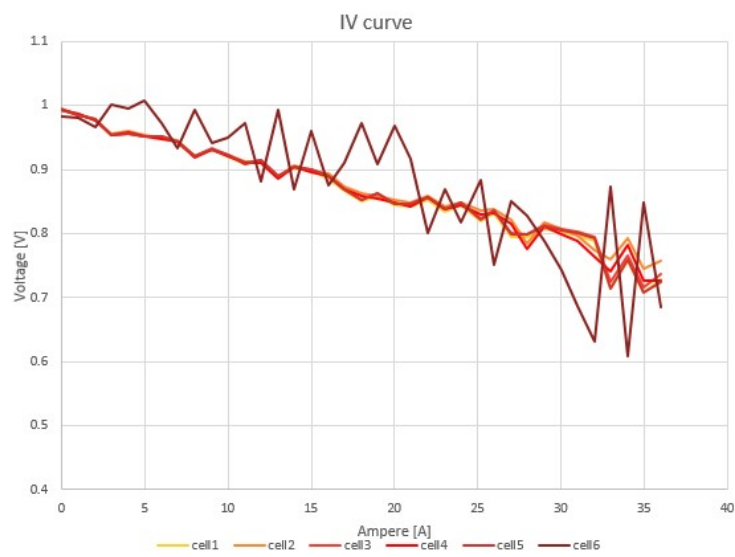
Figure 5.3: Polarization curves with H_2/H_2O 60/40 at a T 757°C.
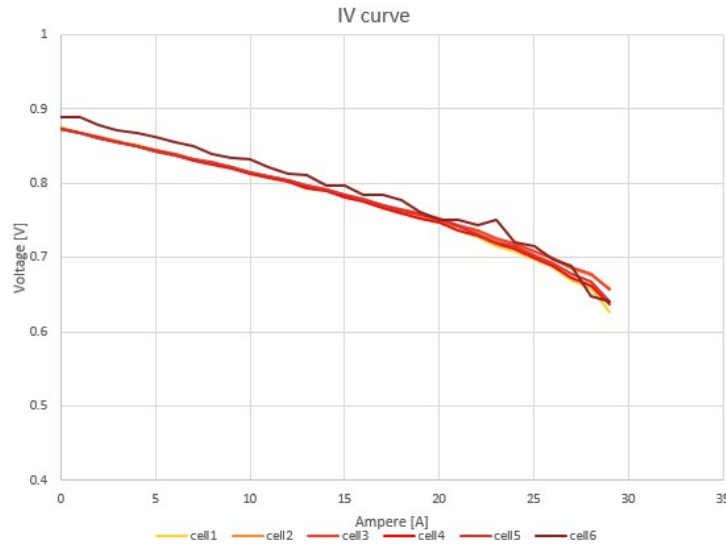
Figure 5.4: Polarization curves with composition H_2/H_2O 10/90 T 757°C.

From Figures 5.4 5.3 5.2, trends are characterized by different steam content. By increasing the steam content from 100% H2,the OCV value decreased, as expected by the Nernst equation. Secondly, the slope of the different curves was lower, increasing the steam content.

The OCV values of the six cells at 60/40 H_2/H_2O showed a minor difference between the theoretical value calculated with the Nernst equation, explained in previous chapters, and the average value of 6 cells. The theoretical value is $982mV$, instead, the average is $992mV$, with a $10mV$ difference that could be due to a minor leak or an inaccuracy of the pump (thus delivering a lower or higher steam content) corresponding to an actual composition of H_2/H_2O of 69/31.

The OCV of the cells at 10/90 H_2/H_2O showed a difference of $8mV$ between the theoretical value of $867mV$, which corresponds to an actual composition of $H2/H2O$ of 14/86. These values indicate good sealing and gas tightness for all the different compositions [35].

	10/90%	**40/60%**
ASR	0.5583 Ωcm^2	0.7373Ωcm^2

Table 5.2: ASR calculated at 10/90 and 60/40

Table 5.2 shows the average ASR value; the values were calculated as the derivative of the I-V curve in a specific current or as the sum of the resistances in the EIS curves. The ASR is almost constant between the cells at a composition of 10/90, with a variation of

3% from the average value. Howerver, at 60/40 H_2/H_2O, , the ASR is affected by some noise due to flow fluctuations from the pump. The six cells in the I-V curves at a 60/40 and at 100% $H2$ presets some noise at a higher current, compared to other cell trends, in Figure 5.5 are reported the I-V curves at 100% H_2. One possible explanation for this noise could be the contact between the current cable and the stack, where the screw was slightly undersized. Anyway, those noises are not affecting the results of the different tests.
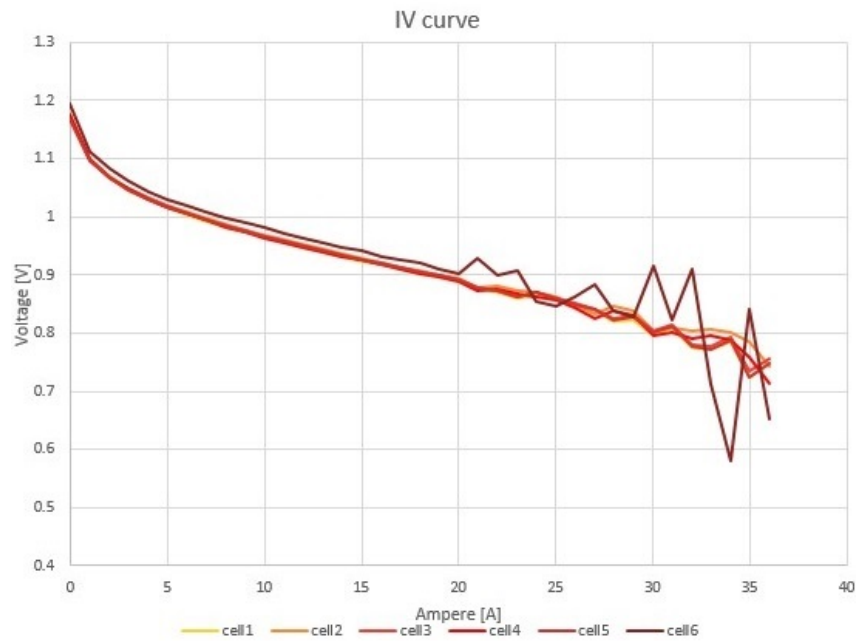
Figure 5.5: I-V curve of different cells at 100% H_2 and 16 l/min air side at T 757 ˚C.

Figure 5.6 shows the Nyquist and Bode diagram at different steam concentrations, 10/90 and 60/40 H_2/H_2O compositions, for the six cells. Figure 5.6 was limited to a frequency of $\approx 25000Hz$ due to limitations from the frequency analyzer caused by the mutual inductance at higher frequencies in combination with low resistances [1, 33]. A suitable polynomial fitting was used to obtain the ohmic and polarization resistance for the 60/40. In Appendix C.1 reports the complete EIS curves without the $25000Hz$ limitation.
The variation in the EIS 10/90 between the six cells is limited; the polarization resistance varies 6% around the average value of $0.322\Omega cm^2$. And the ohmic resistance varies 2.6% from the average value of $0.236\Omega cm^2$.
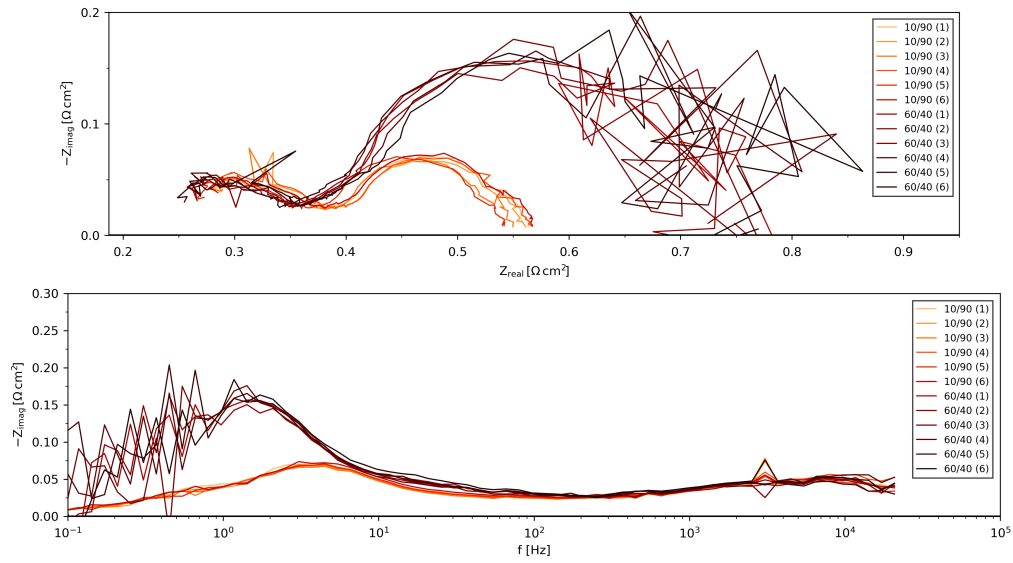
Figure 5.6: Nyquist (top), Bode (bottom) for stack A, with concentration of 10/90 60/40 at a T 757°C.

For the EIS recorded at 60/40 H_2/H_2O, the region at low frequency is affected by noise from the pump's effect for low steam content. On the right side of Figure 5.7, the water flow rate from the pump is shown. On the left, the oscillation voltage of the different cells shows an evident variation of almost $+/-25mV$.
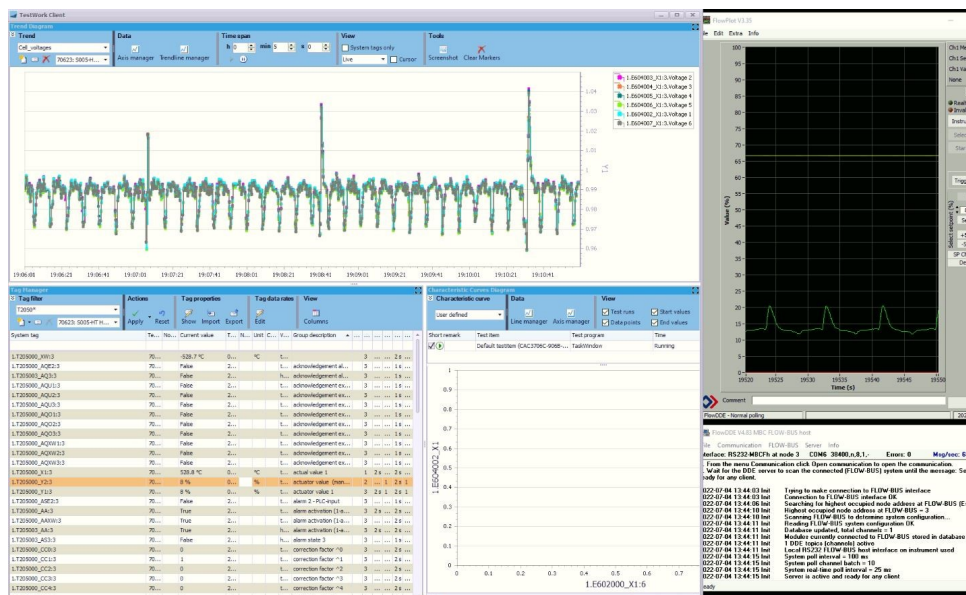
Figure 5.7: Screen shot of of TestWork software (Fuelcon), right pump flowrate, left voltage in function of time.

The variation of the ohmic resistance is about 3.7 % from the average value of $0.225\Omega cm^2$, and the polarization resistance varies about 7.3 % and the average value is $0.511\Omega cm^2$. Additionally, Figure 5.6 shows at low frequency an increment of the polarization resistance between 10/90 and 60/40 caused by the difference in steam content, because this region of low frequency in the Bode diagram, is associated with gas conversion and diffusion contributions. An increase of steam from 40 to 90% showed a reduction of polarization resistance. This observation suggests that nickel catalytic activity depends on the steam content. Budiman et al. studied the hydrogen oxidation reaction with steam in an anode-supported SOFC [13]. They concluded that the presence of OH- on the Ni surface could enhance hydrogen oxidation reaction (HOR). Budiman et al. [13] reported a plausible mechanism of hydrogen oxidation reaction mechanism, identified by two possible spillover reactions of hydrogen from the Ni surface to oxide ions and hydroxyl ions on the YSZ surface, reported in Figure 5.8.
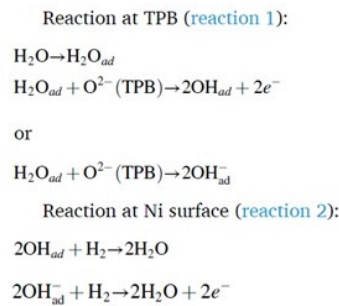
Figure 5.8: Equation form Budiman article [13].
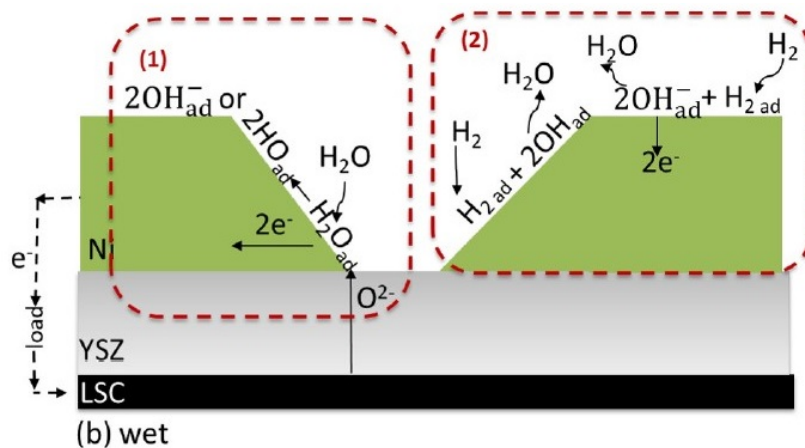
Figure 5.9: Schematic view of plausible hydrogen oxidation reaction mechanism during high p(H2O) [13].

These reactions are represented in Figure 5.9 where some hypotheses regarding the influence of steam on the polarization resistance were studied in Budiman's articles [13, 32]. The HOR can take place at two sites in wet atmospheres. At the TPB, the H_2O enhances O_2^- spillover at the TPB as OH. The OH -ions- from the TPB can enhance the H2 oxidation on the Ni surface. As a result, the active area is not only at TPB but also could be on the Ni surface. And at the end the R_p decreases with the increase of p(H_2O).

The long-term aging of 500 h was carried out to study the changes in the cell performance at OCV, with a concentration of 10/90 H_2/H_2O, without I-V to exclude the effect of current.

5.1.2. Long-term procedure

Figure 5.10: Voltage during 500 h for stack A.

The stack was aged for 500h with no load (OCV) and with a high steam content of 90% and 10% of hydrogen supplied to the fuel electrode to study the isolated effects of steam on the cell performance that was seen in previous cell tests [35]. Figure 5.10 shows the OCV of the total stack during the 500h. In this period, the stack was tested at 10% H2 + 90% H_2O, and at a constant temperature of 753 °C. In the figure are reported some notches along the curve; those voltage changes are caused by the fluctuation for EIS recorded. The EIS and I-V curves were measured at lower steam content to have a more detailed characterization. In fact, in the first 50 h, there was a higher average cell voltage compared to the rest of the period. This is due to the initial characterization at a lower steam content of 60/40; a reduction of water will increase the voltage following the Nernst equation.

Table 5.3 summarizes the flows used during the long-term test. As reported in the Table 5.3, 4 EIS were recorded at 10/90 composition for the long-term characterization. After the first 50 h, the fluid was carried at a constant composition of 10/90, and during this period, some irregularities and discontinuities due to unforeseen events happened. At 200 h and 369 h for a few hours, the pump stopped; however, the test outcome was not affected. After the initial characterization, no IV curves were measured to avoid polarization of the cells. The EIS was recorded at 0 h, 240 h, 388 h, and 500h to minimize the impact of the current.

Time h	Test EIS	$H2L/min$	Ateam L/min	N_2 L/min	Air L/min	Temperature
0	10/90	1.7	13.07	1.2	35	753
240	10/90	1.7	13.07	1.2	35	753
388	10/90	1.7	13.07	1.2	35	753
502	10/90	1.7	13.07	1.2	35	753

Table 5.3: Long tests

Additionally, in Figure 5.10 is possible to appreciate a constant voltage during the test with no appreciable changes.
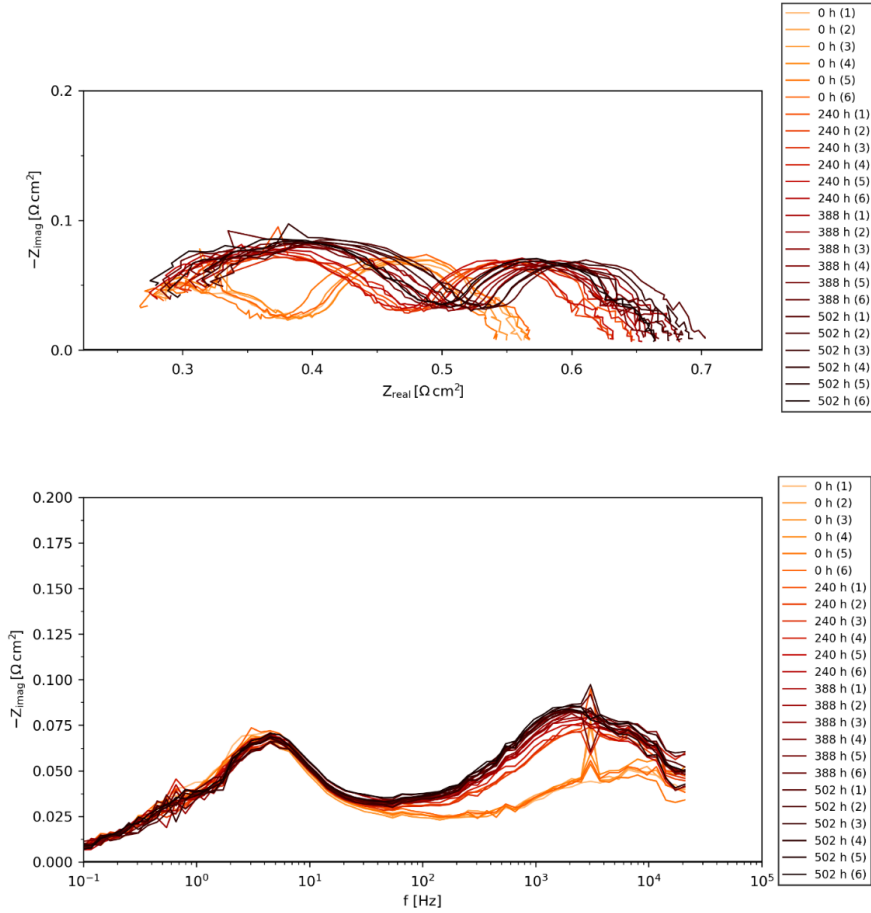
Figure 5.11: Durability at 10/90, on top Nyquist plot, on bottom Bode diagram T 757°C.

The Nyquist and Bode plots, recorded during the durability test at 10/90 at OCV are shown in Figure 5.11.

Figure 5.11, shows that a shift to the right of the EIS with time is observed, as shown in the Nyquist plots. The polarization resistance and the ohmic resistance showed an increase.

After the polynomial fitting of the EIS spectra, it is possible to appreciate a slight increase in ohmic resistance, from an average of $0.236\Omega cm^2$ to $0.252\Omega cm^2$, with a rise in $\approx 6.7\%$. A clear increase can be noted in the polarization resistance, from an average value of $\approx 0.32\Omega cm^2$ to $\approx 0.43\Omega cm^2$ at 502h corresponding to an increase of $\approx 33.5\%$. This effect is also shown in the Bode diagram at high frequencies.

From previous studies [36], identified the loss contribution and their corresponding different frequencies. This increment in the Bode diagram corresponds to a peak at $1kHz -$

$4kHz$, identified by [36] as the charge transfer contribution at the fuel electrode.

Loss contribution		ASC
	Fuel electrode	
Gas conversion		Circa 1Hz
Gas diffusion		30-50Hz
charge transfer		2-6kHz
	Air electrode	
Gas bulk diffusion		0.3-10 Hz
O^{--} **diffusion and** O_2 **surface kinetics**		0.1-1kHz

Table 5.4: Loss contribution and their corresponding different frequencies [36]

The representation of the impedance of the first cell at 0 h and 502 h is shown in Figure 5.12. The shift on the right of the Nyquist plot was observed, with a slight increase in the ohmic resistance and a significant increase in the polarization resistance. The following subchapter explains in detail the different hypotheses related to this behavior.
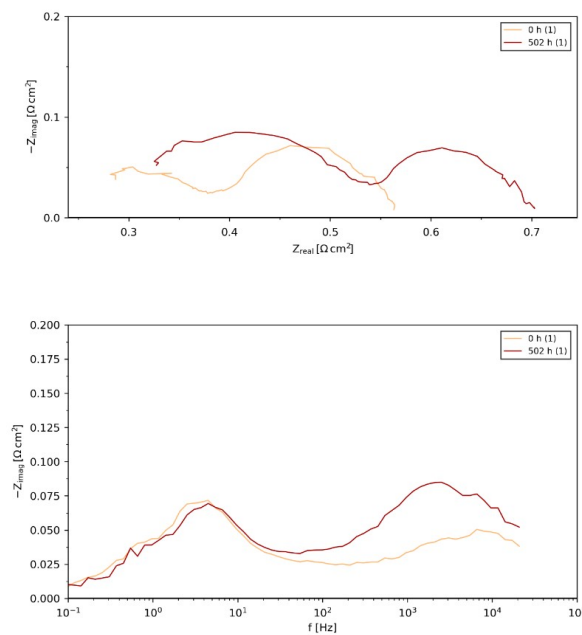
Figure 5.12: Cell 1 at 0h and 502 h at T 757°C and concentration.

5.1.3.   Final characterization

EIS spectra and I-V curve pre and post-durability were taken to obtain a deeper under-standing of the degradation.
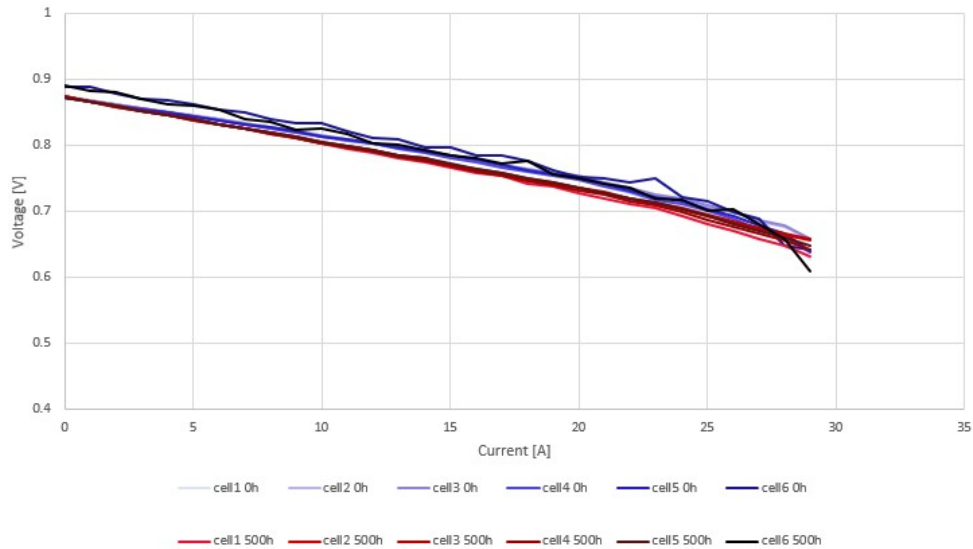
Figure 5.13: I-V curve, blue cells at 0h, orange cells at 500h at 10/90.

Figure 5.13 compares the I-V curve for the different cells before and after the 500 h with 90% steam. The OCV and the cell resistances (slope of I-V) for the other cells are almost identical at 0 h. Increasing the current, the 500 h curves deviate from the starting I-V curve towards lower voltages. Figure 5.14 reports the overall I-V curve of the entire stack at 90% steam, where the trends explained are underlined. In Figure 5.14, the I-V curves of pure Hydrogen noticeable shift towards lower voltages with time.
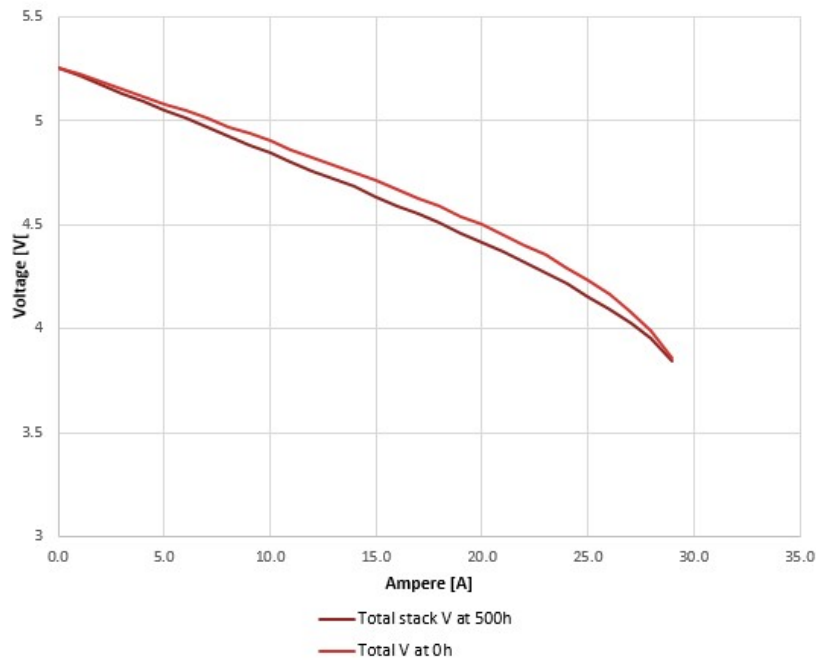
Figure 5.14: I-V curve for the total stack.
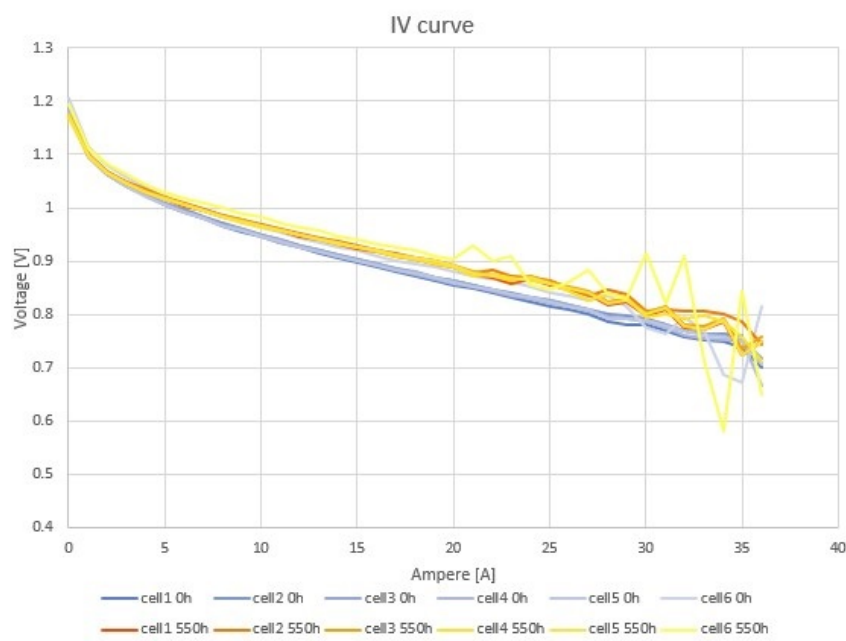
Figure 5.15: I-V curve with fuel content of 100 H2.

For a deeper understanding, the study follows the degradation path graphs from the works of Rasmus and Gazzarri [16, 33], where an increase in the visualization of the evolution of the degradation can be obtained.
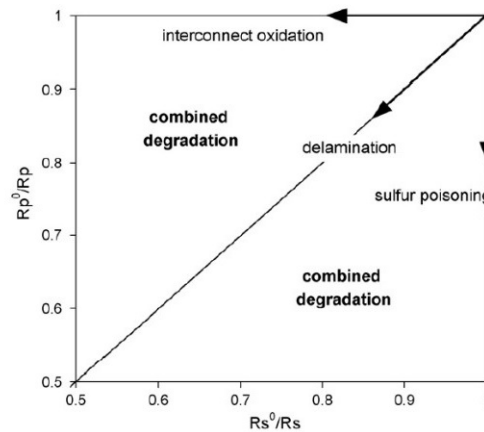
(a) Approximate overall degradation path followed by the mechanisms under study, when acting individually.
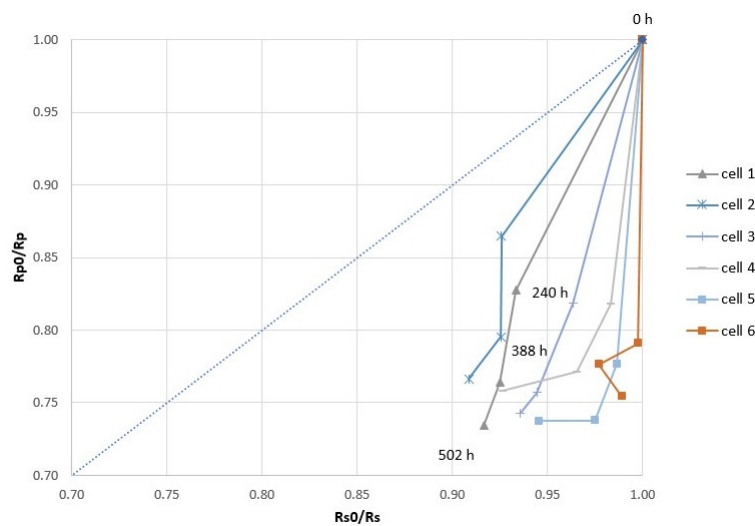
(b) Normalized resistances for each cell.T 757°C at a composition 10/90

Figure 5.16: Study of the normalized resistances.

In Figure 5.16(a), the graph shows the normalized polarization resistance Rop/Rp on the y-axis versus normalized ohmic resistance RSo/RS on the x-axis from the Gazzarri article. Rop and RSo are the initial values, and the point (1,1) corresponds to the initial performance. Different processes mainly affect Rp, reported by [22, 33], such as nickel coarsening, chromium or silica poisoning, and or water-induced changes on the cathode side. If the trajectory follows the 45-degree line, it indicates a change in the active area of the repetitive unit, e.g. delamination. It is essential to identify that this way of visualization of the data does not recognize the degradation specifically, it only identifies

the primary type of degradation, Rs, Rp, or both.
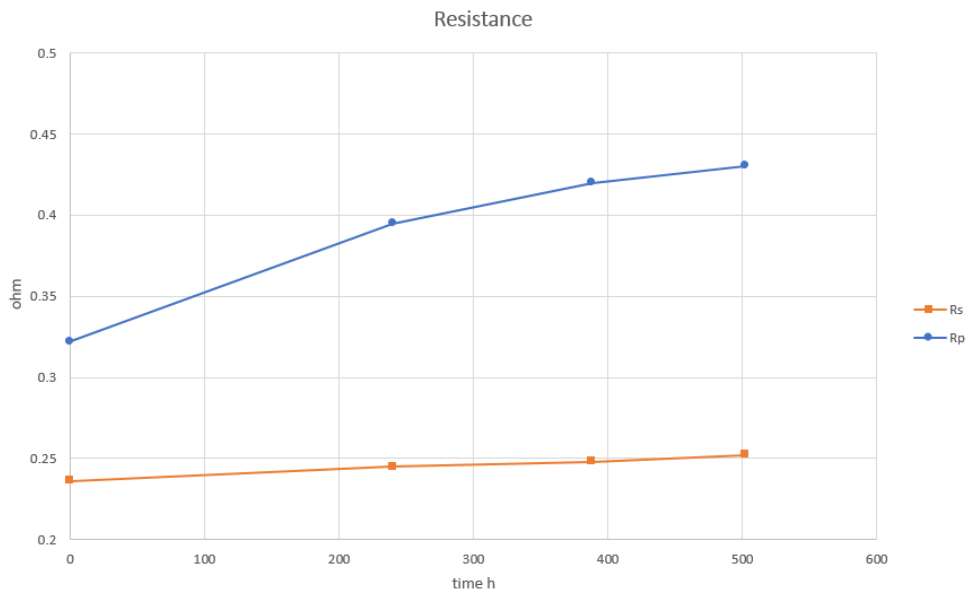
Figure 5.17: Average resistance os stacl with time at T 757 °C and composition 10/90.

On the right of Figure 5.16b is reported all cell normalization of polarization resistance and ohmic resistance at 240 h, 388 h, and 502 h. From this, it is appreciable that the overall trends are below 45°which means that the increase of Rp is higher compared to Rs. In the end, it is observable that the ohmic resistance between 388 h and 502 h have an increased degradation rate compared to the other period. To understand the different trends and to help to speculate, Figure 5.17 shows the variation of the average resistance over time. The ohmic resistance, Rs, is characterized by a slight increase of about 6.77 % from the starting value of $0.236\Omega cm^2$, instead for the polarization resistance is characterized by an increase of approximately 33.5% from the starting value of $0.322\Omega cm^2$. The trend of the polarization resistance is interesting, which seems to reduce the degradation of the Rp after 400 h, reaching a plateau after 500 h.
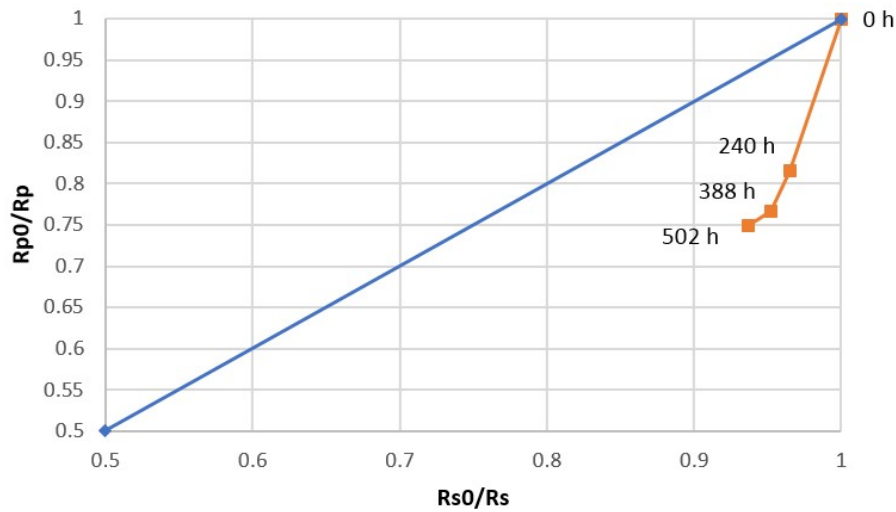
Figure 5.18: Average of the normalized ohmic and polarization resistance at T 757°C and composition 10/90.

Figure 5.18, is reported the overall average degradation of the six cells, where a markable decrement for Rp and a slight decrement of ohmic resistance are notable. This could be explained by a reduction of TPB, like Ni coarsening, Cr poisoning, or silica poisoning, and slight delamination from [22, 33]. A more probable explanation from [22] is the reduction of TPB caused by the Ni coarsening. To arrive at a more detailed understanding of the degradation process, an analysis needs to be supplemented by post-test microscopy, which is beyond the scope of this work. Some hypotheses were found in the literature that are reported below.

Aiswarya's articles [35] speculated on the increase of the ohmic resistance that can be attributed to various causes such as Ni migration resulting in a higher ohmic resistance due to the increase of the electrolyte thickness and an increase in the O_2^- pathway. And/or loss of contact due to delamination from foreign phases. A deep analysis was held by [33] and [35] previously identified that an increase of Rp is attributed to a reduction of the charge transfer contributions at the fuel electrode. The important changes observed were at high frequencies, indicating a TPB loss in terms of Ni coarsening or migration. Aiswarya's articles, which compared two identical cells, one tested at OCV, and one tested in electrolysis mode at 90% steam, seem to identify that the presence of steam degrades the cell, instead with -0.4 A and steam, the degradation results in more than double. As reported in the appendix D.1

Morgensen's articles [32] claims that the loss of active three-phase boundary is associated

with Ni particles coarsening. The reason the coarsening/migration appears opens a field of hypothesis, where three are proposed in the literature.

One from Trini articles [44] where the acceleration in migration has been attributed to the diffusions from the electrode/electrolyte interface towards the support due to the low pO_2, that has high contact angle towards higher pO_2 resulting in a locally lower Ni/YSZ contact angle. In contrast, Morgensen's [32] hypothesis is related to Ni migration and then coarsening, determined by the formation of surface and/or gas phase species of $Ni(OH)_x$, following equation in Figure 5.19, that follow a relative positive local potential toward relative negative potential.

$$Ni(OH)_x\,(g) + 2x\,e^-\,(Ni) \rightleftharpoons Ni\,(s) + x\,O^{2-}\,(YSZ) + \frac{1}{2}x\,H_2\,(g) \tag{4}$$

$$Ni(OH)_x\,(g) + \frac{1}{2}x\,H_2\,(g) \rightleftharpoons Ni\,(s) + x\,H_2O\,(g) \tag{5}$$
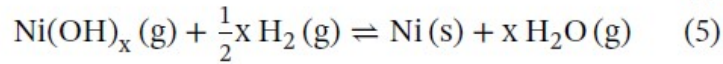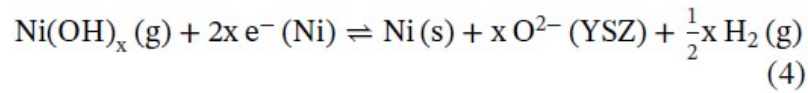
Figure 5.19: formation of $Ni(OH)_x$.

Zekri's article[47], article, instead, speculate that the Ni particles could be transported by evaporation/condensation and diffusion mechanisms. Claims that nickel hydroxide ($NiOH_2$) could be formed near the triple phase boundary, and thanks to the lower melting point of the nickel hydroxide, volatile can move to the surface of the anode. Once nickel hydroxide diffuses to a region with a high partial pressure of hydrogen, the hydroxide then condenses.

Another study speculates on the increase of the degradation rate thank to higher current and higher steam content. In this case, the degradation was happening even due there was no current applied. Therefore, it seems that a deep study must be done. Still, a hypothesis can state that the degradation comes with current and without current, as [35] discovered that the current increases the degradation rate. In the end, it seems that all of the hypotheses from Mogensen, Trini, and Zekri were acceptable; in fact, it appears that the degradation occurs in the formation of Nickel hydroxide, which is transported towards higher pO_2 without current or follows the overpotential if the current is applied. A deeper analysis must be done using SEM to validate those hypotheses.

5.1.4. Comparison with single cell

In this section is reported the comparison between two identical cells, one tested as single cells for 1000 h at 90% steam, as reported by Aiswaria [35], and the other is the first cell of the stack tested for 500 h. Those cells are composed of the same materials, and

Figure 5.20 shows the initial characterization of the cells with the Bode and Nyquist diagram.
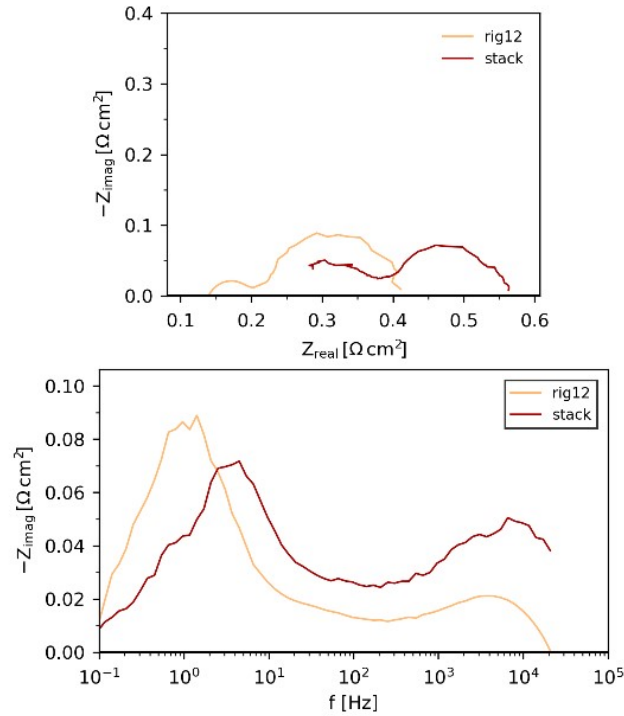
Figure 5.20: Comparison single and first cell of the stack at time 0h, at T 757°C and at a composition of 10/90

From the Nyquist plot, it is evident that the cell from the stack has a curve shifted on the right due to the increase of the ohmic resistance of about 73% from $0.13\Omega cm^2$, probably due to the presence of the interconnection of the different cells. Instead, the polarization resistance for the cell coming from the stack has increased by the 18% more compared to the cell tested alone. The hypothesis behind this change could be related to the slight difference in fuel content, the pretreatment that the stack must undergo for the sealing of the different cells or the influence interconnection of the different cells.

5.2.   Stack B

5.2.1.   Electrochemical characterization

This section is dedicated to the results of the second stack, called Stack B. This stack is composed of 6 cells produced by DTU Energy and assembled by Solid Power Spa in

a Solid power case. The stack was pre-reduced when received from the company. Cells were composed of: a $30\mu m$ thick composite $LSC - CGO$ oxygen electrode, a 6–7μm thick CGO, a $10\mu m$ thick YSZ electrolyte, a 12–16μm thick $Ni - YSZ$ fuel electrode, and a $300\mu m$ thick $Ni - YSZ$[1]. The active area of one single cell is $80cm^2$.

The difference between the two stacks is the previous uses and the air electrode; stack A is a brand-new stack with LSC. Instead, Stack B was already tested at the DTU laboratory in a co-SOEC mode under dynamic conditions and had $LSCF$ as the cathode. The current density was modulated following a wind profile simulating electricity input from fluctuating sources, with a constant flow of $65\%H_2O + 25\%CO_2 + 10\%H_2$, for 1000 h. The electrochemical characterization is characterized by the I-V curve and EIS spectra at OCV for all cells of the stack, a temperature of 757 °C measured on the out of Airside Table 5.5 reports the initial conditions under which the stack was tested. The first I-V tested was characterized by $100\%H_2$, and $16l/min$ in the Airside. Afterward was recorded the impedance diagram at $60\%H_2$, and 40% steam, and subsequently an I-V measurement at 10/90, and then one EIS, at 10/90 H_2/H_2O.

tests	H_2 **L/min**	**Steam L/min**	N_2 **L/min**	**Air L/min**
I-V 100	1.7	-	1.2	16
EIS 60/40	1.7	0.953	1.2	35
I-V 10/90	1.7	13.07	1.2	35
EIS 10/90	1.7	13.07	1.2	35

Table 5.5: Tests initial characterization stack B

Figure 5.21 compares the I-V curves for the stack's six cells at different steam concentrations at T 757 °C with different fuel content, 10/90 H_2/H_2O reported in blue and $100\%H_2$ reported in red with Air on the cathode side.
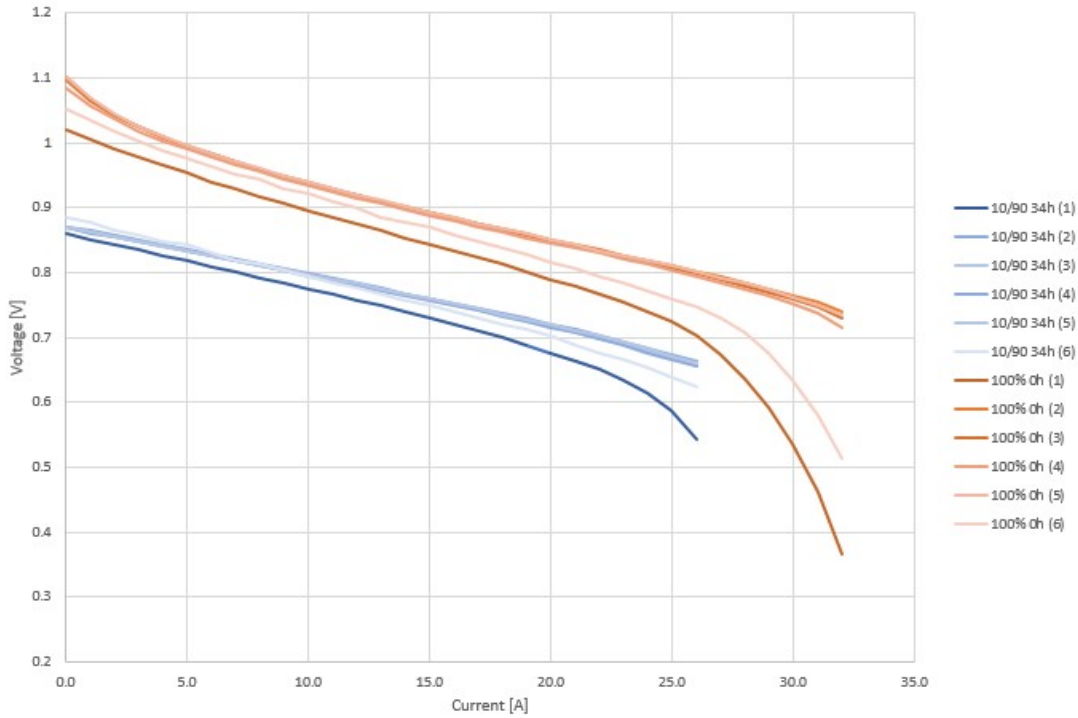
Figure 5.21: I-V curves for different cells at 100% H2 and 10/90.

The OCV values of the cells at 10/90 H_2/H_2O showed an average real value of 0.870 V with a difference of $13.7mV$ from the theoretical value of $856.3mV$ calculated with Nernst; this deviation corresponds to some leakages, which brings to an actual composition of H_2/H_2O of 13.2/86.8. The different cells vary from the average value, with a maximum detachment of 1.6% from an average of about 0.8708 V. The detachment of voltage between different cells increases with the current, as is appreciable in Figure 5.21. The cells that separate the most are the first and the last, which could be explained due to the close position with the metallic box or by different contacts. The same trends are seen in the pure H_2, with a vast separation of the first and last cells compared to the others.

	10/90%	**40/60%**
ASR	0.7476 Ωcm^2	1.0181Ωcm^2

Table 5.6: ASR calculated for concentration at 10/90 and 40/60.

Table 5.6 reports the ASR value; the derivative of the I-V curve can calculate those values in a specific current or as the sum of the resistance in the EIS curves. The ASR varies between the six cells, with a maximum detachment of 14% for the cell 6th in 10/90 content.

Instead, at 60/40, the maximum variation from the average value of ASR is 9.2% for the 6th cell.

Figure 5.22 reports the Nyquist and Bode diagram at different steam concentrations, 10/90 and 60/40, for the six cells. As explained in the previous chapter, the diagram reported in Figure 5.22 have a frequency limit of about 25000 Hz caused by the mutual inductance between the difference voltage cables inside the stack [33]. The ohmic resistance was evaluated thanks to a polynomial fitting of data. On the left is reported the 60/40 H_2/H_2O plot, and on the right is reported the 10/90 H_2/H_2O.
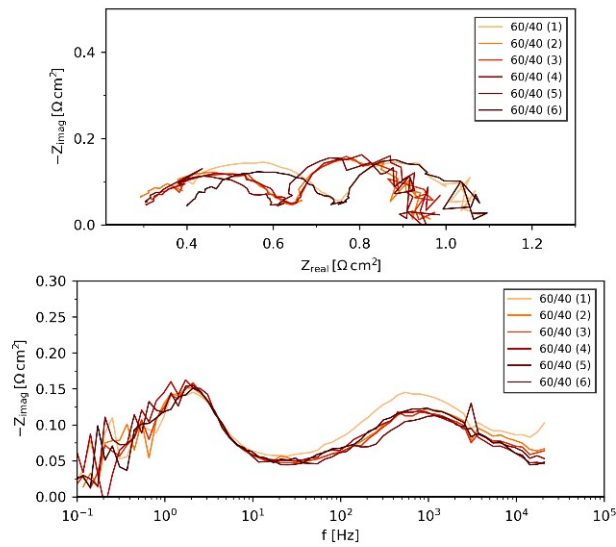
(a) Stack A.
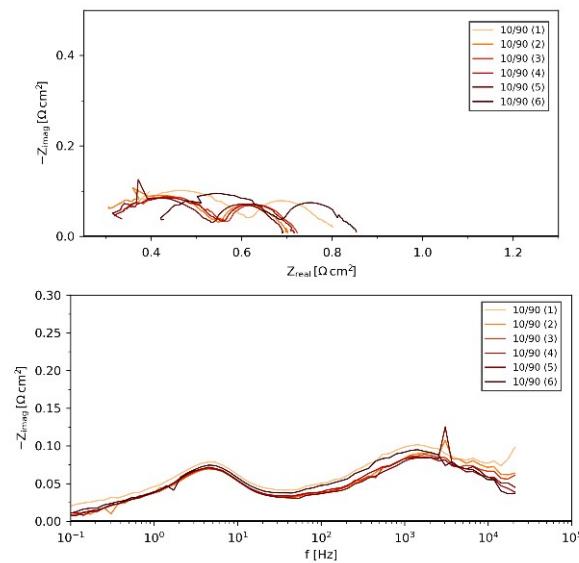
(b) Stack B.

Figure 5.22: EIS for different concentration, on the left 60/40 and on the right 10/90 for different cell at a T 757°C.

As seen in the previous chapter, by reducing the steam content, the polarization resistance increased, and the same trend was seen during the last stack too. The first markable aspect in each diagram is the shift of the impedance of cell 1 and cell 6, which was seen already in Rao's article that tested this stack before this test. [1] They reported speculation about the different behavior of the cells related to the temperature gradient or contact issues

between the cells.

The variation for the polarization resistance in the EIS 60/40 content for the six different cells is about 11.2% from the average value of $0.758\Omega cm^2$. Instead, the ohmic resistance varies 37% from the average value of $0.259\Omega cm^2$. The difference between the first and last cells is interesting compared to the others, which have a more considerable ohmic resistance. In the end, the 60/40 Nyquist and Bode diagram presents some noise caused by the pump at low frequencies as reported in the previous analysis.

The IV and EIS characterization prove that the different cells are comparable. Thus, the long-term aging of 500 h was carried out to study the changes in the cell performance at OCV, with a concentration of 10/90 H_2/H_2O, without I-V to exclude the effect of current.

5.2.2.   Long-term procedure
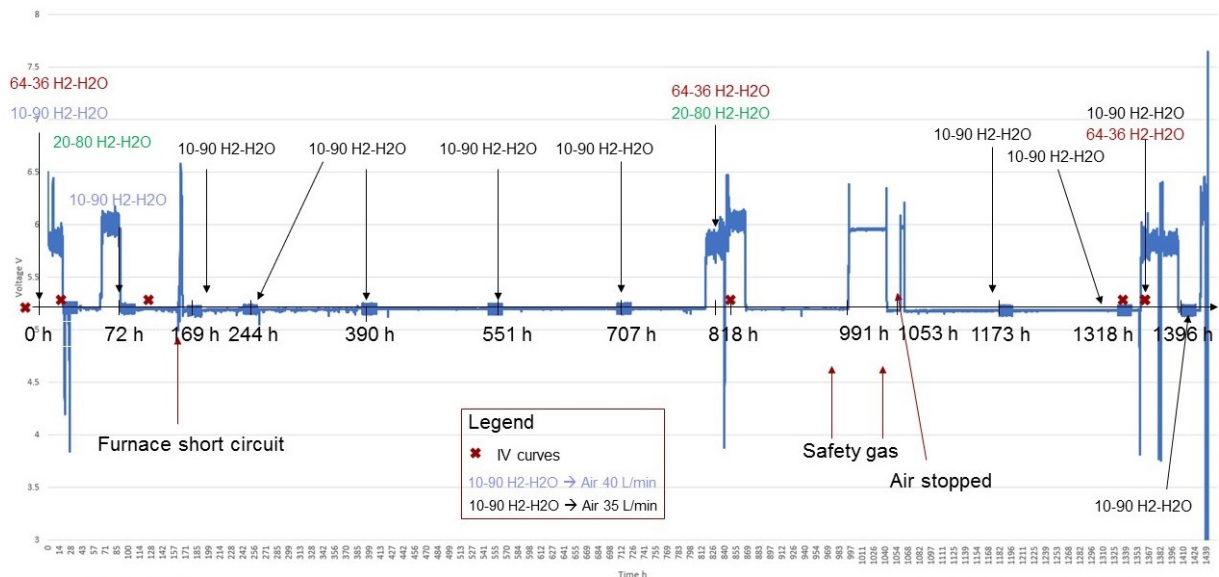
Figure 5.23: Open circuit voltage in function of time for the entire stack.

The stack was tested for 1439 h with no load (OCV) at high steam content of about 90% and 10% of hydrogen supplied to the fuel electrode.

Figure 5.23 reports the OCV of the total stack during the time tested. In this period, the stack was tested at $10\%H_2 + 90\%H_2O$, and at a constant temperature of 757°C, in the figure are reported some notches along the curve, and those voltage changes are caused by EIS recorded. In the first 72 h, there is a recorded voltage higher, compared to the rest of the period, due to the initial characterization at lower steam content of 60/40 and 20/80; in fact, a reduction of water will increase the voltage following the Nernst equation.

Table 5.7 summarizes the flows used during the long-term test, where were recorded 8

EIS at 10/90 composition. During this period were recorded, two additional EIS with a composition of 10/90, reported in purple in Figure 5.23. Those plots differ from the others due to the flow at the Air-side with 5 l/min more. This will influence the temperature of the inlet and outlet stack and are not comparable with the other. In the end, 3 EIS were recorded at 0 h, 840 h, and around 1374 h at 60/40.

After the first 72 h, the flow rate was carried at a constant composition of 10/90, and during this period, some irregularities and discontinuities due to unforeseen events happened. At 169 h, the furnace stopped for a short circuit, and at 991 h for some hours, it was forced to switch to safe mode for laboratory maintenance. Safety gas is a flow used during the warm-up procedure or cool-down; it is composed of 5% of H_2, and 95% of N_2. After 1053 h the Air stopped.

The explanation of the different effects of this effect is going to be addressed later. After the initial characterization, only one I-V curve was measured to avoid polarization of the cells, at 840h. The EIS was recorded at a distance of about 150 h to minimize the impact of the current.

Time h	Test EIS	$H2 L/min$	Ateam L/min	N_2 L/min	Air L/min	Temperature
0	EIS 10/90	1.7	0.953	1.2	16	757
169	EIS 10/90	1.7	13.07	1.2	35	757
244	EIS 10/90	1.7	13.07	1.2	35	757
390	EIS 10/90	1.7	13.07	1.2	35	757
551	EIS10/90	1.7	13.07	1.2	35	757
707	EIS10/90	1.7	13.07	1.2	35	757
818	EIS 60/40	1.7	0.953	1.2	16	757
840	I-V 60/40	1.7	0.953	1.2	16	757
1173	EIS 10/90	1.7	13.07	1.2	35	757
1369	I-V 60/40	1.7	0.953	1.2	16	757
1396	EIS 10/90	1.7	13.07	1.2	35	757

Table 5.7: Long tests

Figure 5.23 shows that the voltage trend at OCV for the first period till 818 h seems quite linear. The OCV average for the entire stack between 270-370h is 5.194 V; instead, the average between 600-700 h is about 5.2003 V, with an increment of 0.12%. Instead, after the safety gas period, there is a little decrement in the voltage. In fact, the average

between 1200 and 1300 is 5.1844 V, with a reduction of 0.30%. These are little changes that can be considered due to some voltage measurement contact movement, or slight temperature changes.
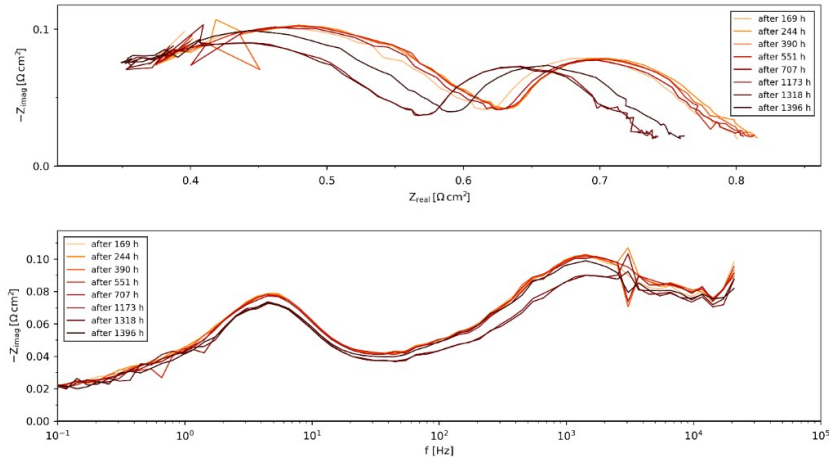
Figure 5.24: Nyquist and Bode diagram, for cell1 in time at 10/90.
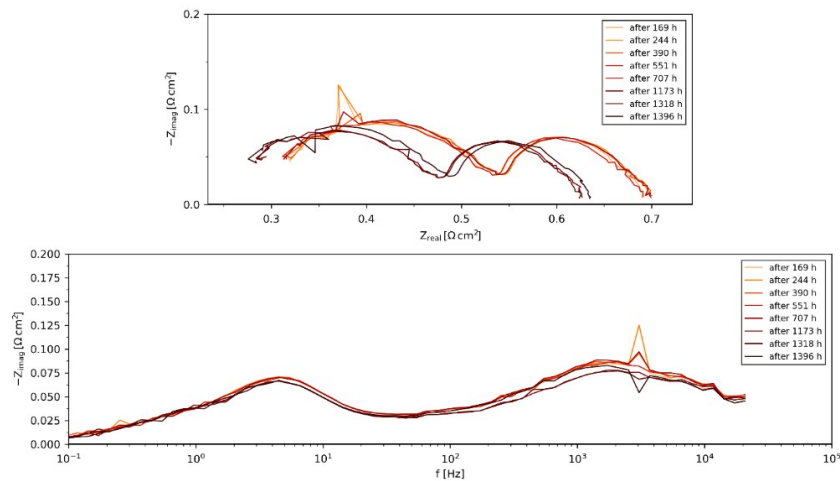
Figure 5.25: Nyquist and Bode diagram for cell 5 bottom in time, at 10/90.

Figure 5.24, 5.25, shows Nyquist and Bode plots for cells 1 and 5 with a fuel input of 90% H_2O, and 10% H_2. In both cases, it is appreciable that the curves for the first 707 h are almost the same with little changes. In the appendix E.4 are reported the other 4 cells. Even in the Bode diagram, the curve is consistent, instead, the darkest curve is the curve after the safety gas period, so after 1173h are shifted on the left. Those shifts are related

to the ohmic resistance and the polarization resistance. Comparing the cells between 169 h and 1173, for the ohmic resistance, there is a reduction of 4% from the average Rs 0.28 Ωcm^2 and a 10 % reduction for polarization resistance from the average value of 0.462 Ωcm^2.

The reason for these changes can only be speculated because there wasn't the possibility to open the stack and have an SEM analysis. One hypothesis could be related to the re-oxidation and reduction after the stop of the fuel of the Nickel surface [24], or related to an improvement of contacts.

In Figure 5.26 are reported the Nyquist and Bode plots for cell 1 on the left and cell 4 on the right, recorded during durability test at 60/40 at OCV.

(a) Stack A.

(b) Stack B.
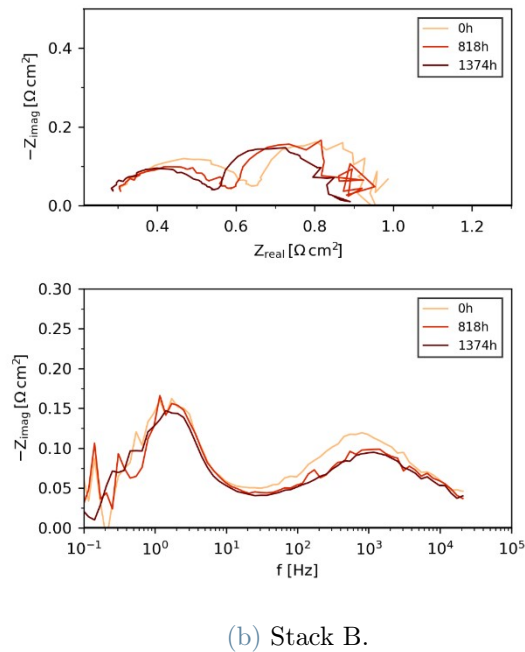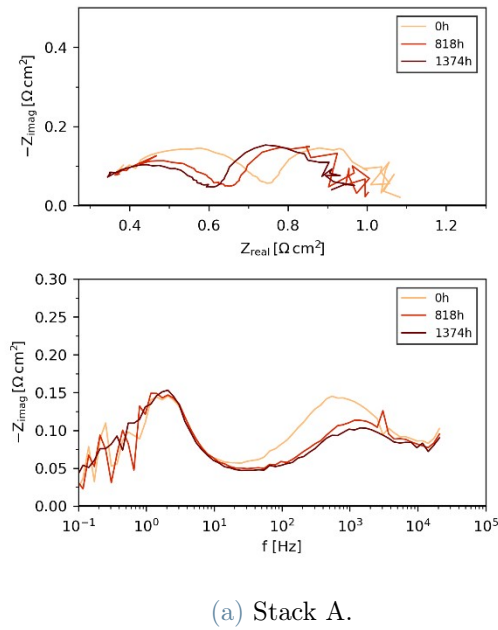
Figure 5.26: Nyquist and Bode plot at 60/40 for cell1 (left) and cell4 (right).

The first appreciable thing is the effect of the pump at low frequencies that creates some noise, which can be seen in the Bode diagram and Nyquist. Figure 5.26 shows for simplicity, just two cells, the other is going to be reported in the appendix F.4, and as explained in the previous chapter, the curves are cut at 25000 Hz. From the Nyquist diagram, it

is evident that with the changing of time, there is a shift on the left of the impedance curve. It can be appreciable more between 0h and 818 h than seems to reach a plateau of improvement. The average polarization resistance decreases by about 13.2% from a starting value of $0.758\Omega cm^2$, with a decrement of 6.3 % in the first 818 h and 7.3 % till 1374 h.

Instead, the average ohmic resistance has a decrement of about 3% overall, with an increment in the first 818 h of about 2% from the starting value of 0.2594 Ωcm^2, and a decrement of about 5.05%, till $0.2514\Omega cm^2$ at 1374h.

Looking to the previous chapter, the affected frequency region is between 100 and 3000 Hz, which Aiswarya identified as the TPB region [35]. These changes are appreciable in the Bode diagram, where the improvement at 1000 Hz reduces over time; after the 818 h, it seems to reach a plateau. The different hypotheses of unconventional behavior will be explained in the following subchapter.

5.2.3. Final characterization

To obtain a deeper understanding of the durability, EIS and I-V curves pre and post-durability were taken.

5.2.4. Long-term procedure
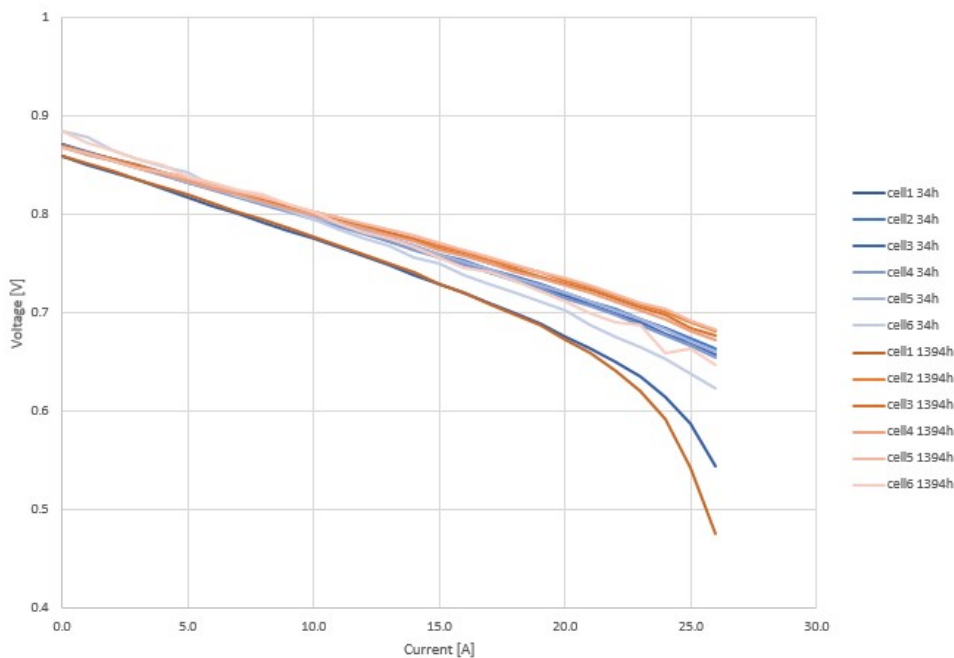
Figure 5.27: I-V at 10/90 at 34 h and at 1394 h T 757 °C.

Figure 5.27 compares the I-V curve for the different cells before and after the 1394 h with 90% steam. The first thing that can be appreciated is almost no change at OCV, then increasing the current is evident that the I-V curve taken at 1394 h deviate from the curve taken at 34 h, which presents an improvement for all the cells apart from the first cell.
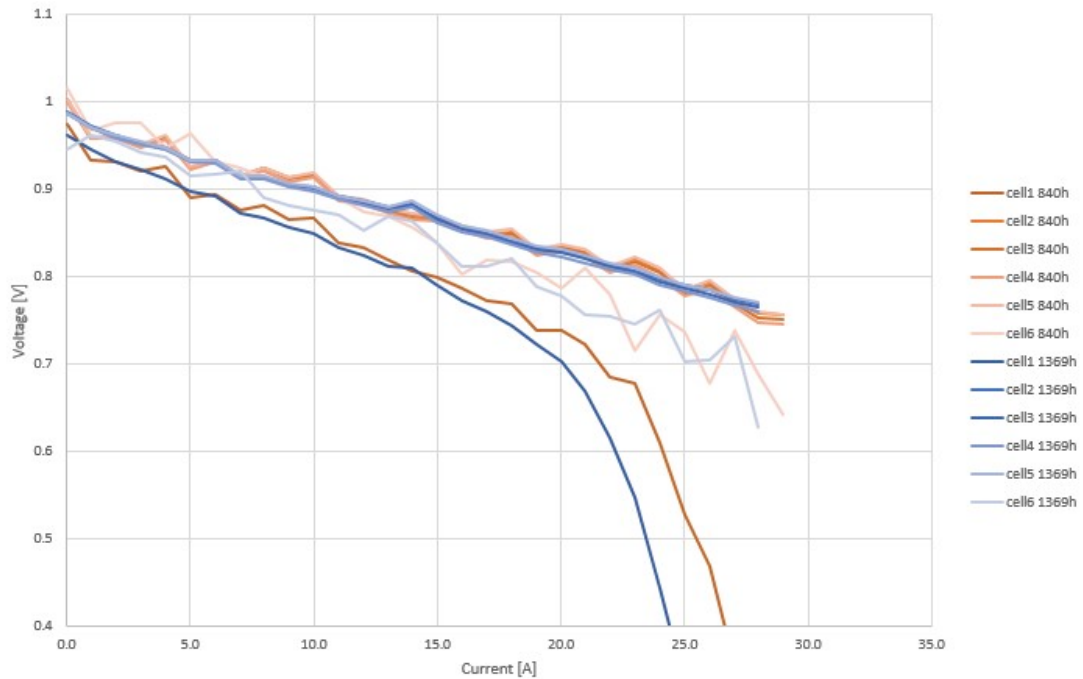
Figure 5.28: I-V at 60/40 at 840 h and 1369 h.

Instead, Figure 5.28 reports the I-V curve for a fuel content of 60% steam and 40% H_2; those curves were taken at 840 h and 1369 h. The first evident thing is that the curves are characterized by some noise that can be attributed to the pump; then, apart from the 1 cell, it is appreciable that the different cells' curves are almost identical over the others in time. This underlines the same behavior seen at OCV with EIS, that after 818 h, there was a reduction of improvement till 1394 h.

Instead, from Figure 5.28 is evident that the first cell is characterized by degradation, unseen by the EIS because was taken at OCV. The same trends were already found in the literature [18, 21] and were explained by the near presence of the metallic box, affecting the cell with chromium poisoning. This hypothesis can be verified by the presence of chromium found at the outlet of the stack's inner side, Figure 5.29, but only an SEM analysis of the cell will verify this phenomenon.

(a) Stack A.
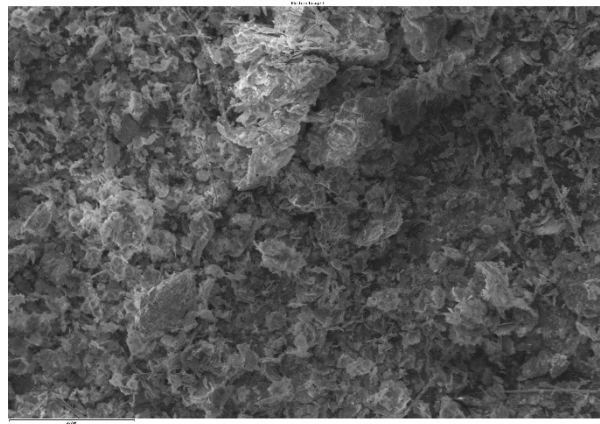
(b) Stack B.

Figure 5.29: On top where was located the powder, on bottom are the SEM image.

As reported in the previous analysis of stack A, to understand the deep phenomenon, the study will follow the graph of [16, 33], where an increase in the visualization of the evolution of durability is appreciable Figure 5.30.
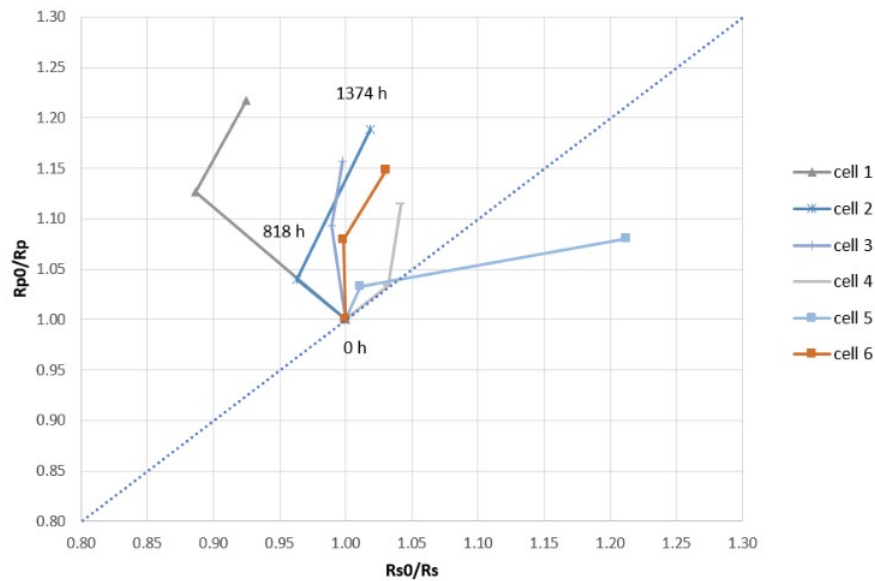
Figure 5.30: Normalization of the ohmic and polarization resistance 60/40.

Figure 5.30 reports all cells normalization of polarization resistance and ohmic resistance at 818 h and 1374 h at 60/40. All the trends are above the two bottom quarters delimited by (1,1), which means there is an improvement for Rp. In fact, all lines are going towards a high value of normalization, starting from (1,1); instead, the ohmic resistance is characterized by different behaviors. The first, second and third cell have a degradation of Rs, till 818 h; instead after 818 h, the influence of safety gas stop and seems to influence the cell, reducing the ohmic resistance for all the cells. The other cells are in the high-right quarter, which indicates an improvement for Rs and Rp. As speculated by Rao in articles [1] this different behavior of cells can be attributed to the difference in temperature gradient or, more feasible, to some contact issues between the cells.
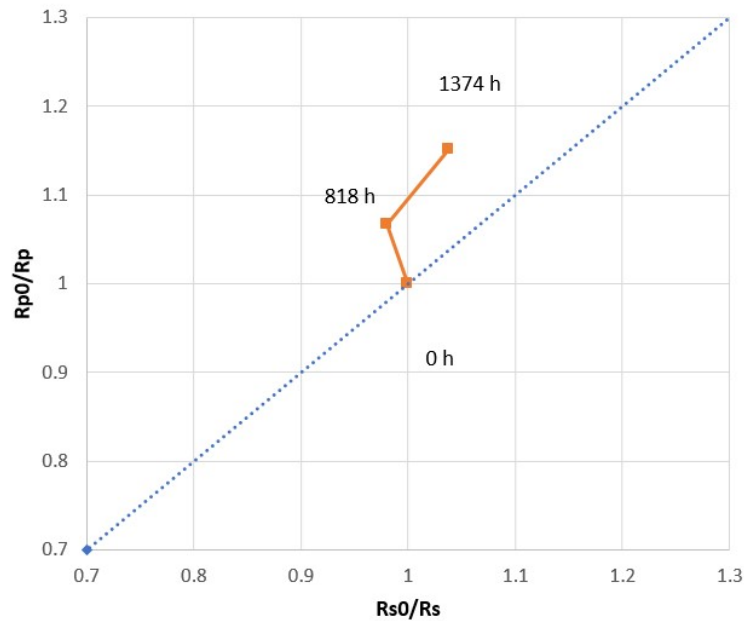
Figure 5.31: Overall stack normalization 60/40.

Figure 5.31 shows the average Rs and Rp, for the 6 cells, at 818 h and 1374 h. Overall the test is characterized by a decrease of the polarization resistance, a slight degradation of the ohmic resistance till 818 h, and an improvement caused by the safety gas period. This trend can be seen in Figure 5.32 where the different resistance is reported in the time function.
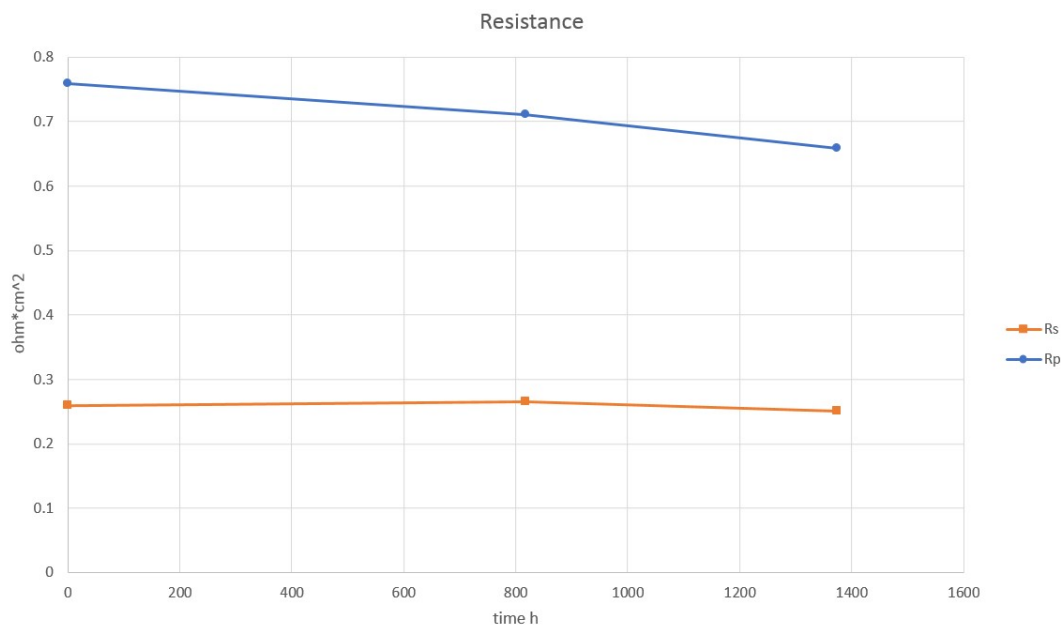
Figure 5.32: Resistance in function of time at 60/40.

The first appreciable thing is that the ohmic resistance is almost constant, and the huge improvement is given by the polarization resistance, which is affected by 100-2000 Hz, which is related to the TPB. Unluckily, in this study, there wasn't the possibility to open the stack and analyze the cells through SEM, but looking at the literature, some hypotheses were speculated to be similar behavior.

Singhal's article [18, 24] claims that Ni can catalyze the formation of carbon from hydro-carbons under reducing conditions. Unless sufficient steam and hydrocarbons are used to remove the carbon from the nickel surface, this could explain these test results due to the existence of CO_2 in the stack's prior history of roughly 1000 hours, which may coat nickel surfaces, and because of fuel with a high steam content (9%), carbon might be removed from the surface even if it occurred at two distinct times.

5.3. Comparison with single cell

This section reports the comparison between two identical cells, one tested as a single cell for 1000 h at 90% steam, written by Aiswarya [35], and the other one is the second cell of the stack tested for 1439 h. Those cells are composed of the same materials for the anode side for the cathode side instead of the cell of [35], which is composed of $LSCF - CGO$. Instead the stack is composed of $LSC - CGO$. Figure 5.33 shows the initial characterization of the cells with Bode and Nyquist diagram.
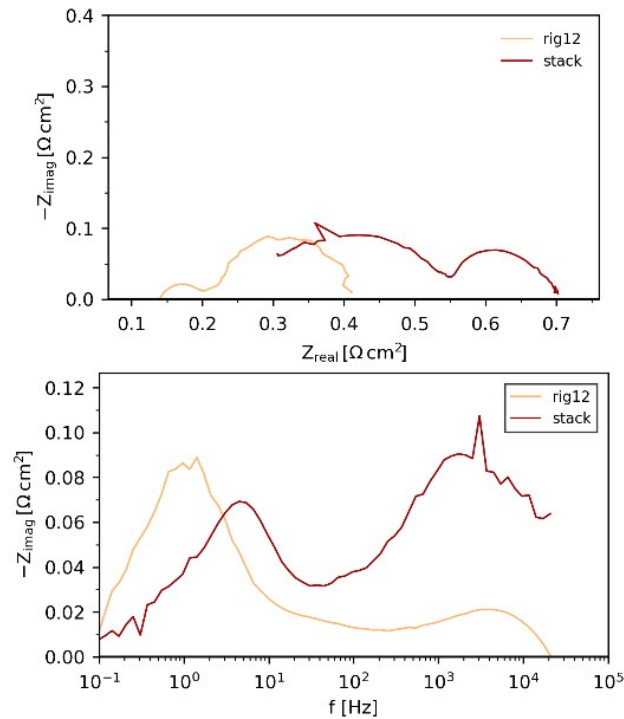
Figure 5.33: Comparison between single cell and stack cell at 10/90.

From the Nyquist plot, it is evident that the cell from the stack has a curve shifted on the right due to an increase of the ohmic resistance of about 67% from $0.13\Omega cm^2$, probably due to the presence of the interconnection of the different cells. Instead, the polarization resistance for the cell from the stack has increased by the 72%. The hypothesis behind this change could be related to the difference in the cell material and to the previous history of the stack, 1000h in co-electrolysis.

5.4.   Comparison of stack A and stack B

In this subchapter are going to be compared the two stacks. Stack A is brand-new, and Stack B has a previous history of co-electrolysis for 1000h.

Figure 5.34 reports the EIS for stack A in orange colors and stack B in darker colors. Those measurements were taken at the beginning of test time. It is appreciable that stack A has lower ohmic resistance and lower polarization resistance compared to stack B. Instead, stack B was taken at 169 h because the measurements taken before this time weren't incomparable.
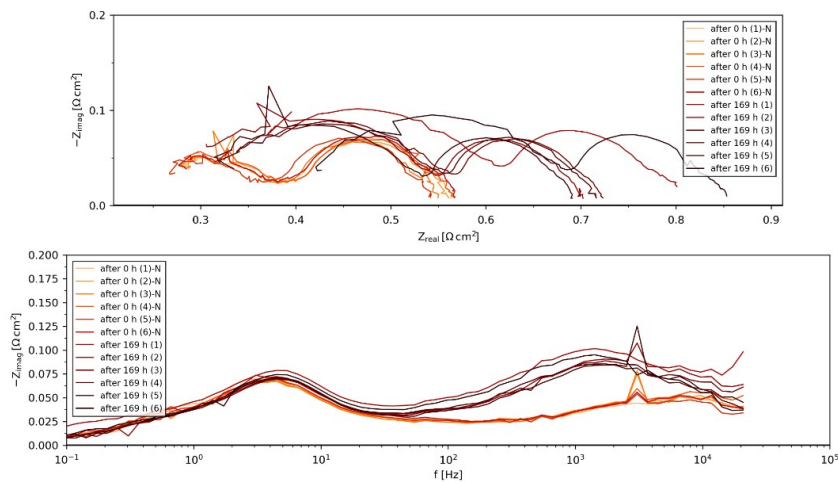
Figure 5.34: Comparison of different stacks cell at 10/90 at the beginning of test.

Figure 5.35 shows the average Rs and Rp in the function of time for Stack A and Stack B with a fuel content of 60/40. In the figure, Stack A is characterized by a triangle dot, instead, Stack B is represented by a circle. As reported in the previous chapters, during the 500 h Stack A has a degradation related to the polarization resistance, and the ohmic resistance remains almost constant with a slight degradation.
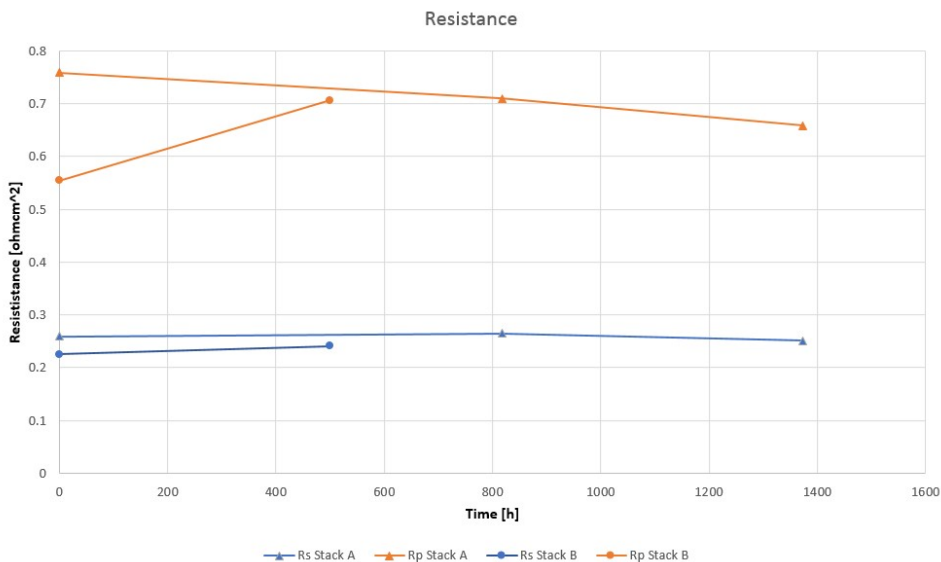
Figure 5.35: Average resistance in time for stack A and stack B at 60/40.

Instead, for the Stack B during the 1400 h, is present a reduction in the ohmic polarization and the ohmic resistance remains almost constant. This figure 5.35 is interesting for the

trend of stack A, which has a huge degradation rate caused by the high content of steam, which reaches almost the values of polarization resistance of Stack B at the initial test. Those trends explain that the use of high steam content leads to a big deterioration, compared to a stack that is not brand-new high steam as Stack B.
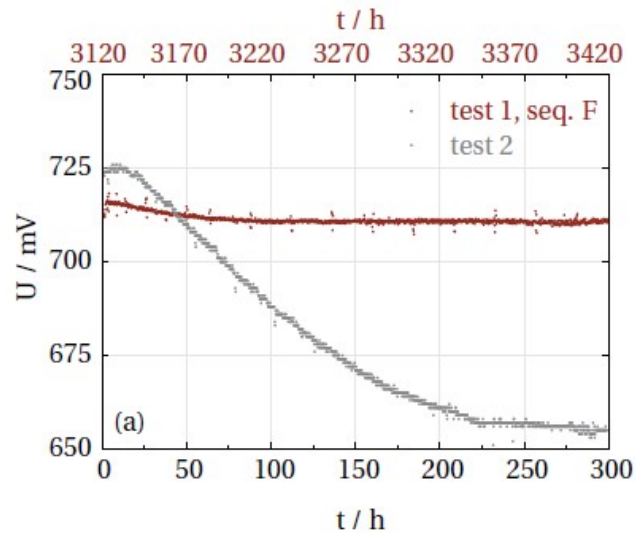
Figure 5.36: Ploner tests: 2 cells one fresh and the other with a pass hystory, with current at $0.5A/cm^2$ and $p(H_2O)$ of 0.72.

Ploner saw this tendency in her Ph.D. thesis [37] where she tested two identical cells; cell 1 was characterized by 3100 h of the previous test instead, cell 2 was brand-new. That two cells were then tested for 300 h with $0.5A/cm^2$ with a $p(H_2O)$ of 0.72, and in figure 5.36 are reported the cell voltage during this period. She underlined that the presence of high steam content on a brand new cell increases the degradation rate compared to a cell with a previous history. Ploner speculates that the $Ni - YSZ$ electrode goes through an initial period of 'stabilization,' which is affected by steam content. The degradation was discovered during the analysis using SEM in the outlet of the cell, where was evident some percolating Ni.
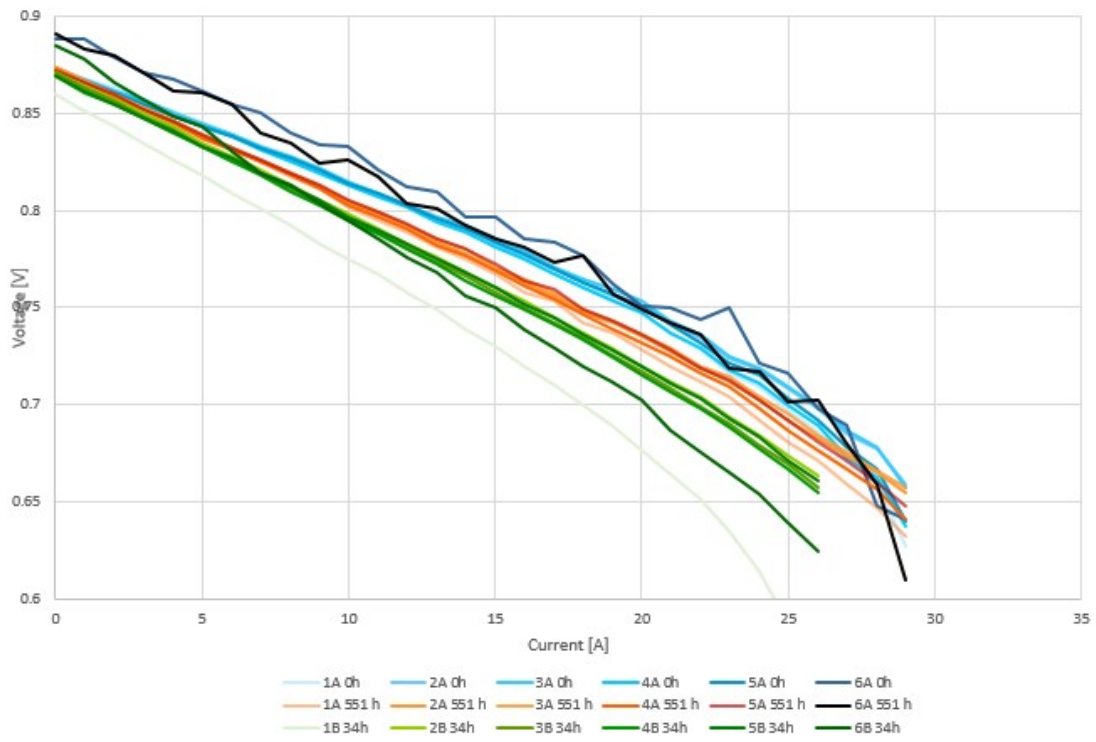
Figure 5.37: Stack A at 0h and 551 h and Stack B at 34 h at 10/90.

To complete the analysis Figure 5.37 reports two groups of I-V curves for Stack A and Stack B. Stack A is represented by blue/orange colors; green colors characterize instead stack B. Figure reports the three groups of I-V measured, at 34 h for stack B, and before/after 551h for Stack A. As already explained in previous chapters, cell 1 for Stack B is completely separated from the others, instead is interesting that the groups of cells from stack A during 500 h degradate, almost reaching the I-V curves at the beginning of Stack B. This trend was explained in the Rp/Rs Figure 5.35 and was inspired by Ploner speculating that with high steam content, there is an increase in the degradation rate higher if the stack is brand-new compared to one with the previous history of the test.

6 | Conclusion and outlook

This work is composed of studying two stacks, stack A and stack B; both tests were characterized by a test at 10/90 H_2O/H_2 concentration at OCV.

The difference between the two stacks is the previous uses and the air electrode; stack A is a brand-new stack with LSC as cathode. Instead, Stack B was already tested at the DTU laboratory in a co-SOEC mode under dynamic conditions and has $LSCF$ as cathode.

Stack A

After 500 h of test was seen a degradation in the polarization resistance of about 33.5% and 6.7% in the ohmic resistance, these changes are related to the high frequencies and can be speculate that is caused by a degradation of the triple phase boundary. In the end, looking to literature for some hypotheses, seems that all of the hypotheses from Mogensen and Trini, and Zekri were acceptable; in fact, it appears that the degradation is caused by coarsening/migration of Ni, and this occurs thanks to the formation of Nickel hydroxide, due to the presence of a high concentration of steam. Nickel hydroxide diffuses and is transported towards higher pO_2 without current, so towards lower contact angle or follows the overpotential if the current is applied. In this case, the degradation was happening with no current applied. A deeper analysis must be done using SEM to validate those hypotheses seen in the literature.

Stack B

The stack was tested for 1439 h with no load (OCV) at high steam connect of about 90% and 10% of hydrogen supplied to the fuel electrode. Overall, the test is characterized by a decrease of the polarization resistance, a slight degradation of the ohmic resistance till 818 h, and then an improvement; this can be caused by the safety gas period.

The first appreciable thing is that the ohmic resistance is almost constant, and the considerable improvement is given by the polarization resistance of about 13.2%, which is effect by 100-2000 Hz, which can be related to the TPB.

Unluckily, in this study, there wasn't the possibility to open the stack and analyze the cells through SEM, but looking at the literature, some hypotheses were speculated to be

similar behavior. In fact, Singhal's article [18, 24] claims that Ni can catalyze the formation of carbon from hydrocarbons under reducing conditions. Unless sufficient steam and hydrocarbons are used to remove the carbon from the nickel surface. This could explain this test results due to the existence of CO_2 in the stack's prior history for roughly 1000 hours, which may coat nickel surfaces, and because of fuel with hydrogen and a high steam content (90%), carbon might be removed from the surface even if it occurred in a second moment than CO_2.

In the end, overall, the same trend was seen by Ploner in her Ph.D. thesis [37]. She underlined that the presence of high steam content on a brand new cell increases the degradation rate compared to a cell with a previous history. Ploner speculates that the $Ni - YSZ$ electrode goes through an initial period of 'stabilization,' which is affected by steam content.

To underline and understand better those hypothesis, new tests must be done with the possibility of studying the cell with SEM. It will be interesting to use two identical cells with a content of 90% of steam as fuel in, one at OCV and one under current. Those tests with post-mortem SEM analyses could give some final proof of the mechanism behind this degradation.

From the tests, there are two takes home that must be underlined. First, in literature, cell degradation, studied 500 h, can be affected by the steam phenomenon if present, so the degradation test should start after considering this stabilization time. Second, it can be interesting the utilization of high content of steam at OCV to regain the performance lost after the co-SOEC utilization of the stack.

Bibliography

[1] Durability of solid oxide electrolysis stack under dynamic load cycling for syngas production. URL `https://www.researchgate.net/publication/339088508`.

[2] V76a-d-6m-s-v76seriesteefilters.

[3] Series2700daqsystemdatasheet.

[4] Test equipment solutions datasheet. URL `www.kepcopower.com/bop.htm`.

[5] Current transducer it 200-s ultrastab i pm = 200 a. URL `www.lem.com`.

[6] Seite 1 kompetenz in wasser.

[7] Pump p 2.1s/p 4.1s instructions hplc hplc. URL `www.blauer-engel.de/en/uz195`.

[8] 252a lf frequency response analyzer. URL `www.solartronanalytical.com`.

[9] Thermocouple sensors temperature.

[10] Clean hydrogen mission-no emission, 2020.

[11] Truedata-load modular electronic dc load, 2021.

[12] Mechanical details, 2022. URL `www.eurotherm.co.uk`.

[13] R. A. Budiman, T. Ishiyama, K. D. Bagarinao, H. Kishimoto, K. Yamaji, and T. Horita. Dependence of hydrogen oxidation reaction on water vapor in anode-supported solid oxide fuel cells. *Solid State Ionics*, 362, 4 2021. ISSN 01672738. doi: 10.1016/j.ssi.2021.115565.

[14] K. Chen, D. Dong, and S. P. Jiang. Hydrogen production from water and air through solid oxide electrolysis, 2015.

[15] Q. Fang, L. Blum, R. Peters, M. Peksen, P. Batfalsky, and D. Stolten. Sofc stack performance under high fuel utilization. *International Journal of Hydrogen Energy*, 40:1128–1136, 1 2015. ISSN 03603199. doi: 10.1016/j.ijhydene.2014.11.094.

[16] J. I. Gazzarri and O. Kesler. Short stack modeling of degradation in solid oxide fuel cells. part ii. sensitivity and interaction analysis. *Journal of Power Sources*, 176: 155–166, 1 2008. ISSN 03787753. doi: 10.1016/j.jpowsour.2007.10.046.

[17] B. B. High-Tech. Quick installation guide starting up el-flow®select in 10 steps, 2020. URL `www.bronkhorst.com/downloads`.

[18] J. T. Irvine and P. Connor. Solid oxide fuels cells: Facts and figures: Past, present and future perspectives for sofc technologies. *Green Energy and Technology*, 55, 2013. ISSN 18653537. doi: 10.1007/978-1-4471-4456-4.

[19] J. T. Irvine, D. Neagu, M. C. Verbraeken, C. Chatzichristodoulou, C. Graves, and M. B. Mogensen. Evolution of the electrochemical interface in high-temperature fuel cells and electrolysers, 1 2016. ISSN 20587546.

[20] S. P. Jiang. Development of lanthanum strontium manganite perovskite cathode materials of solid oxide fuel cells: A review. *Journal of Materials Science*, 43:6799–6833, 11 2008. ISSN 00222461. doi: 10.1007/s10853-008-2966-6.

[21] S. P. Jiang and Q. Li. Introduction to fuel cells electrochemistry and materials introduction to fuel cells introduction to fuel cells.

[22] Z. Jiao, N. Shikazono, and N. Kasagi. Study on degradation of solid oxide fuel cell anode by using pure nickel electrode. *Journal of Power Sources*, 196:8366–8376, 10 2011. ISSN 03787753. doi: 10.1016/j.jpowsour.2011.06.069.

[23] G.-B. Jung, L.-H. Fang, C.-Y. Lin, X.-V. Nguyen, C.-C. Yeh, C.-Y. Lee, J.-W. Yu, S.-H. Chan, W.-T. Lee, S.-W. Chang, and I.-C. Kao. Electrochemical performance and long-term durability of a reversible solid oxide fuel cell, 2015. URL `www.electrochemsci.org`.

[24] M. S. Khan, S. B. Lee, R. H. Song, J. W. Lee, T. H. Lim, and S. J. Park. Fundamental mechanisms involved in the degradation of nickel–yttria stabilized zirconia (ni–ysz) anode during solid oxide fuel cells operation: A review, 2016. ISSN 02728842.

[25] A. Kromp. model-based interpretation of the performance and degradation of reformate fueled solid oxide fuel cells.

[26] A. Leonide, Y. Apel, and E. Ivers-Tiffee. Sofc modeling and parameter identification by means of impedance spectroscopy. *ECS Transactions*, 19:81–109, 10 2009. ISSN 1938-5862. doi: 10.1149/1.3247567.

[27] J. Markowski and I. Pielecha. The potential of fuel cells as a drive source of

maritime transport. volume 214. Institute of Physics Publishing, 1 2019. doi: 10.1088/1755-1315/214/1/012019.

[28] T. Matsui, T. Fujinaga, R. Shimizu, T. Ozeki, H. Muroyama, and K. Eguchi. Degradation behavior of solid oxide fuel cells operated at high fuel utilization. *Journal of The Electrochemical Society*, 168:104509, 10 2021. ISSN 0013-4651. doi: 10.1149/1945-7111/ac27dc.

[29] N. Q. Minh. Reversible solid oxide cell technology, 2022.

[30] M. B. Mogensen, A. Hauch, X. Sun, M. Chen, Y. Tao, S. D. Ebbesen, K. V. Hansen, and P. V. Hendriksen. Relation between ni particle shape change and ni migration in ni–ysz electrodes – a hypothesis. *Fuel Cells*, 17:434–441, 8 2017. ISSN 16156854. doi: 10.1002/fuce.201600222.

[31] M. B. Mogensen, M. Chen, H. L. Frandsen, C. Graves, J. B. Hansen, K. V. Hansen, A. Hauch, T. Jacobsen, S. H. Jensen, T. L. Skafte, and X. Sun. Reversible solid-oxide cells for clean and sustainable energy, 11 2019. ISSN 2515396X.

[32] M. B. Mogensen, M. Chen, H. L. Frandsen, C. Graves, A. Hauch, P. V. Hendriksen, T. Jacobsen, S. H. Jensen, T. L. Skafte, and X. Sun. Ni migration in solid oxide cell electrodes: Review and revised hypothesis. *Fuel Cells*, 21:415–429, 10 2021. ISSN 16156854. doi: 10.1002/fuce.202100072.

[33] R. R. Mosbæk. *Solid oxide fuel cell stack diagnostics : Ph. D. thesis*. DTU Energy Conversion, Department of Energy Conversion and Storage, 2014. ISBN 9788792986207.

[34] K. H. Ng, H. A. Rahman, and M. R. Somalu. Review: Enhancement of composite anode materials for low-temperature solid oxide fuels. *International Journal of Hydrogen Energy*, 44:30692–30704, 11 2019. ISSN 03603199. doi: 10.1016/j.ijhydene.2018.11.137.

[35] A. Padinjarethil and A. Hagen. Identification of degradation parameters in soc using in-situ and ex-situ approaches. *ECS Transactions*, 103:1069–1082, 7 2021. ISSN 1938-5862. doi: 10.1149/10301.1069ecst.

[36] A. K. Padinjarethil, F. R. Bianchi, B. Bosio, and A. Hagen. Electrochemical characterization and modelling of anode and electrolyte supported solid oxide fuel cells. *Frontiers in Energy Research*, 9, 9 2021. ISSN 2296598X. doi: 10.3389/fenrg.2021.668964.

[37] A. Ploner. Solid oxide fuel cell degradation studies accelerated testing and lifetime prediction, 2018. URL `www.energy.dtu.dk`.

[38] S. Primdahl and M. Mogensen. Durability and thermal cycling of ni/ysz cermet anodes for solid oxide fuel cells.

[39] M. Rao, S. H. Jensen, X. Sun, and A. Hagen. Unwinding entangled degradation mechanisms in solid oxide electrolysis cells through electrode modifications and impedance analysis. *Fuel Cells*, 19:445–457, 2019. ISSN 16156854. doi: 10.1002/fuce.201800166.

[40] S. N. Sampathkumar, P. Aubin, K. Couturier, X. Sun, B. R. Sudireddy, S. Diethelm, M. Pérez-Fortes, and J. V. herle. Degradation study of a reversible solid oxide cell (rsoc) short stack using distribution of relaxation times (drt) analysis. *International Journal of Hydrogen Energy*, 47:10175–10193, 2 2022. ISSN 03603199. doi: 10.1016/j.ijhydene.2022.01.104.

[41] H. Schichlein, A. C. Mu¨ller, M. Mu¨ller, M. Voigts, A. Kru¨gel, K. Kru¨gel, and E. Ivers-Tiffé. Deconvolution of electrochemical impedance spectra for the identification of electrode reaction mechanisms in solid oxide fuel cells q.

[42] V. Sonn, A. Leonide, and E. Ivers-Tiffée. Combined deconvolution and cnls fitting approach applied on the impedance response of technical ni 8ysz cermet electrodes. *Journal of The Electrochemical Society*, 155:B675, 2008. ISSN 00134651. doi: 10.1149/1.2908860.

[43] D. Stolten and B. Emonts. *Fuel cell science and engineering : materials, processes, systems and technology.* John Wiley Sons, 2012. ISBN 9783527330126.

[44] M. Trini, A. Hauch, S. D. Angelis, X. Tong, P. V. Hendriksen, and M. Chen. Comparison of microstructural evolution of fuel electrodes in solid oxide fuel cells and electrolysis cells. *Journal of Power Sources*, 450, 2 2020. ISSN 03787753. doi: 10.1016/j.jpowsour.2019.227599.

[45] T. H. Wan, M. Saccoccio, C. Chen, and F. Ciucci. Influence of the discretization methods on the distribution of relaxation times deconvolution: Implementing radial basis functions with drttools. *Electrochimica Acta*, 184:483–499, 12 2015. ISSN 00134686. doi: 10.1016/j.electacta.2015.09.097.

[46] C. Xie and S. Quan. Drawing impedance spectroscopy for fuel cell by eis. volume 11, pages 589–596. Elsevier B.V., 2011. doi: 10.1016/j.proenv.2011.12.092.

[47] A. Zekri, K. Herbrig, M. Knipper, J. Parisi, and T. Plaggenborg. Nickel depletion

and agglomeration in sofc anodes during long-term operation. *Fuel Cells*, 17:359–366, 6 2017. ISSN 16156854. doi: 10.1002/fuce.201600220.

A | Appendix A
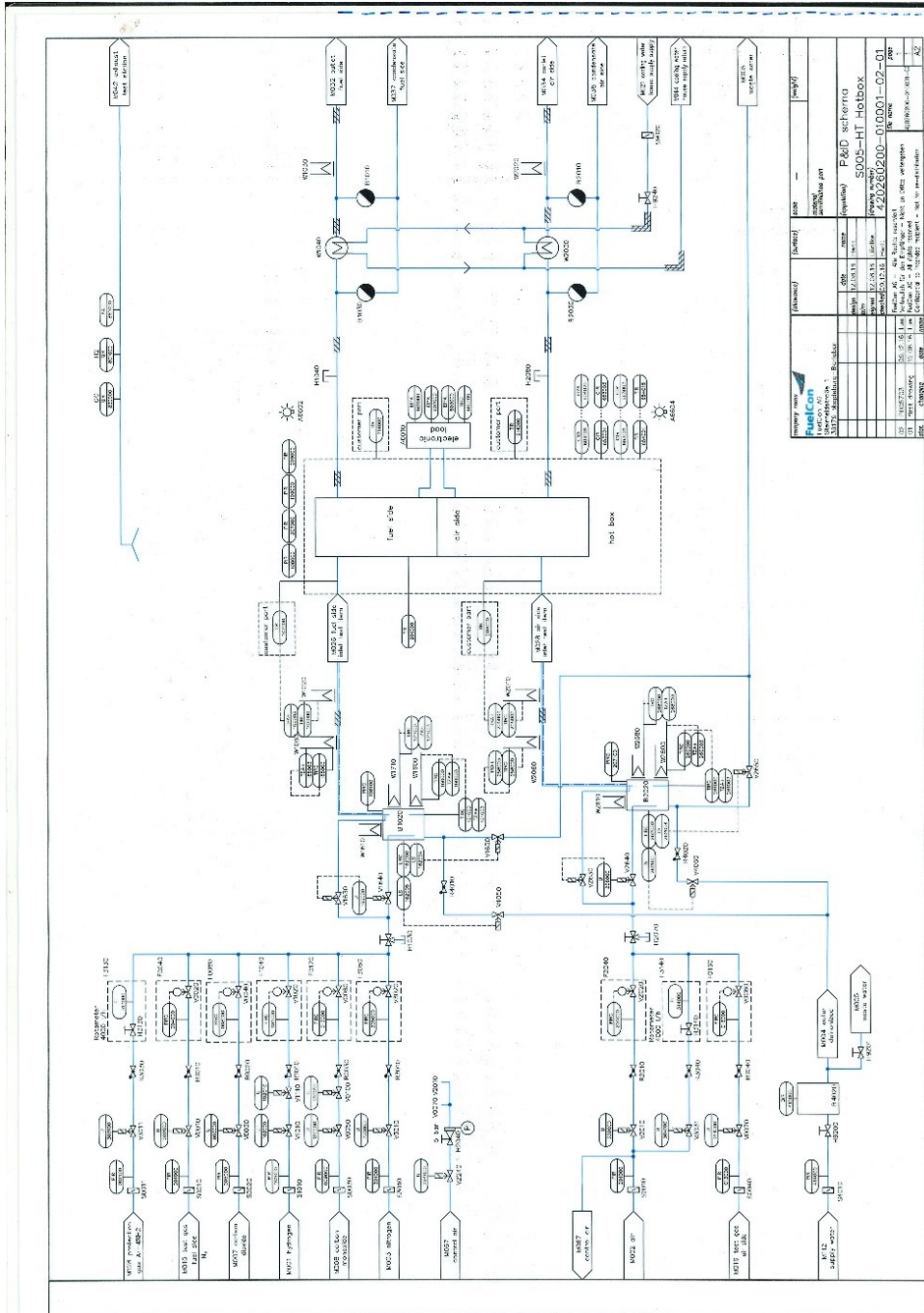
Figure A.1: Original scheme of the Rig.
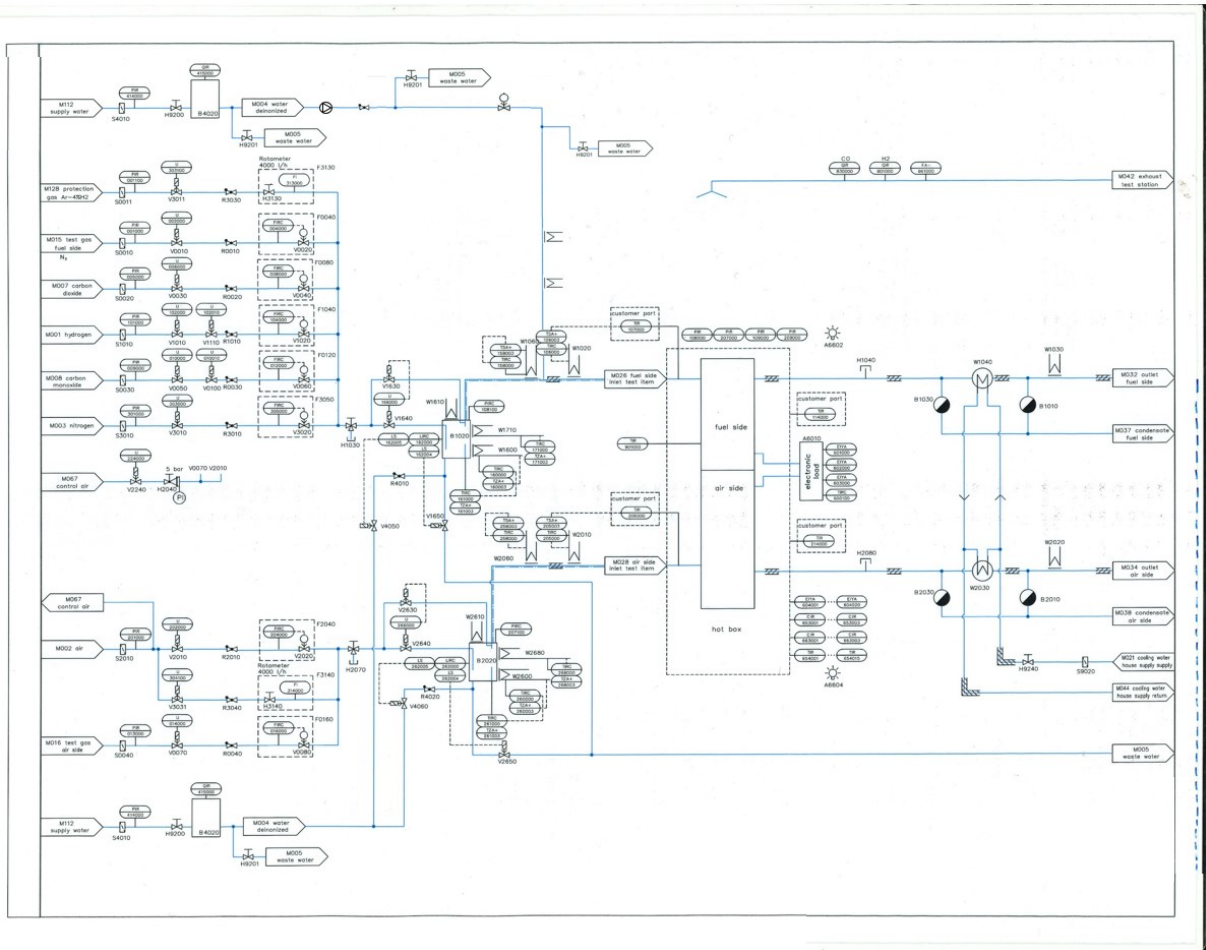
Figure A.2: Modified scheme of the rig with additional water line.

B | Appendix B

B.1.

Type J is built from iron and Cu-Ni metals, the temperature range of this is -180 ˚C to +750˚C. The sensitivity of type J is $54\mu V/$˚C.

Type T is composed of Cu and Cu-Ni. The range is -250˚C to +400˚C. The sensitivity of this thermocouple is 46μ V/˚C.

Type E thermocouple is constructed using Ni-Cr (Chromel) and Cu-Ni (Constantan) metals. The temperature range is -40˚C to +900˚C, and has the highest sensitivity at 68μ V/˚C.

Type R is composed using Pt-Rh (Platinum-radium) and Pt (Platinum). The sensitivity is low at $8\mu V/$˚C. The range is -50˚C to +1700˚C.

Type B thermocouple is composed of Pt-Rh (Platinum-radium). The sensitivity is very low, at $1\mu V/$˚C and the range is -100˚C to +1750˚C

C | Appendix C
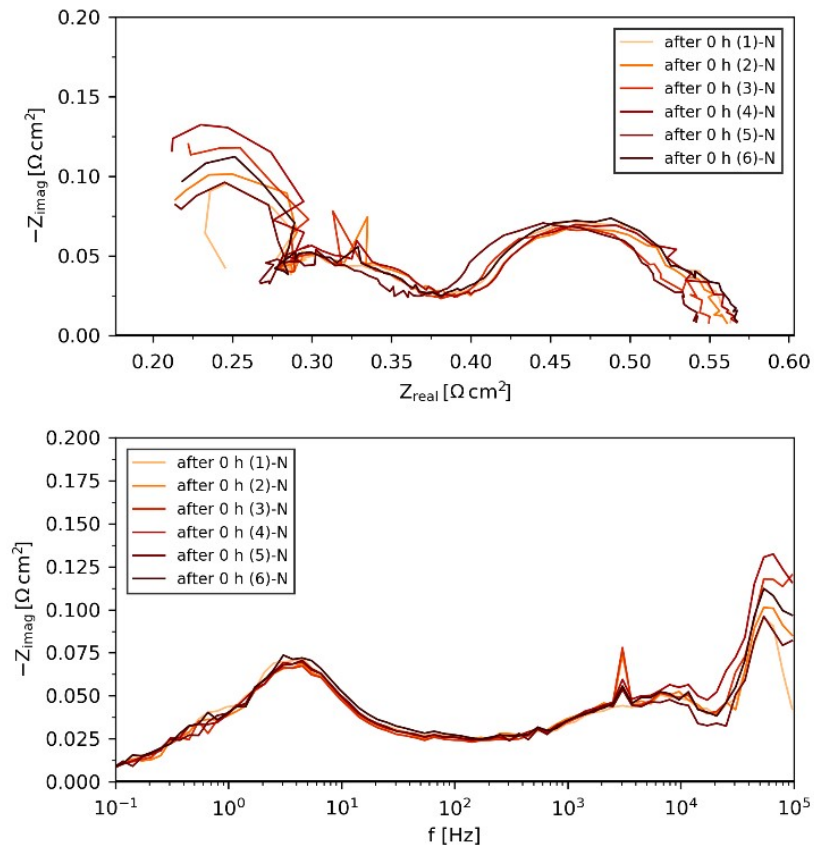
Figure C.1: Nyquist (top), Bode (plot) for the 6 cells of the new stack(A), without the frequencies cut, with a composition of 10/09 at T 757 °C .

D | Appendix D
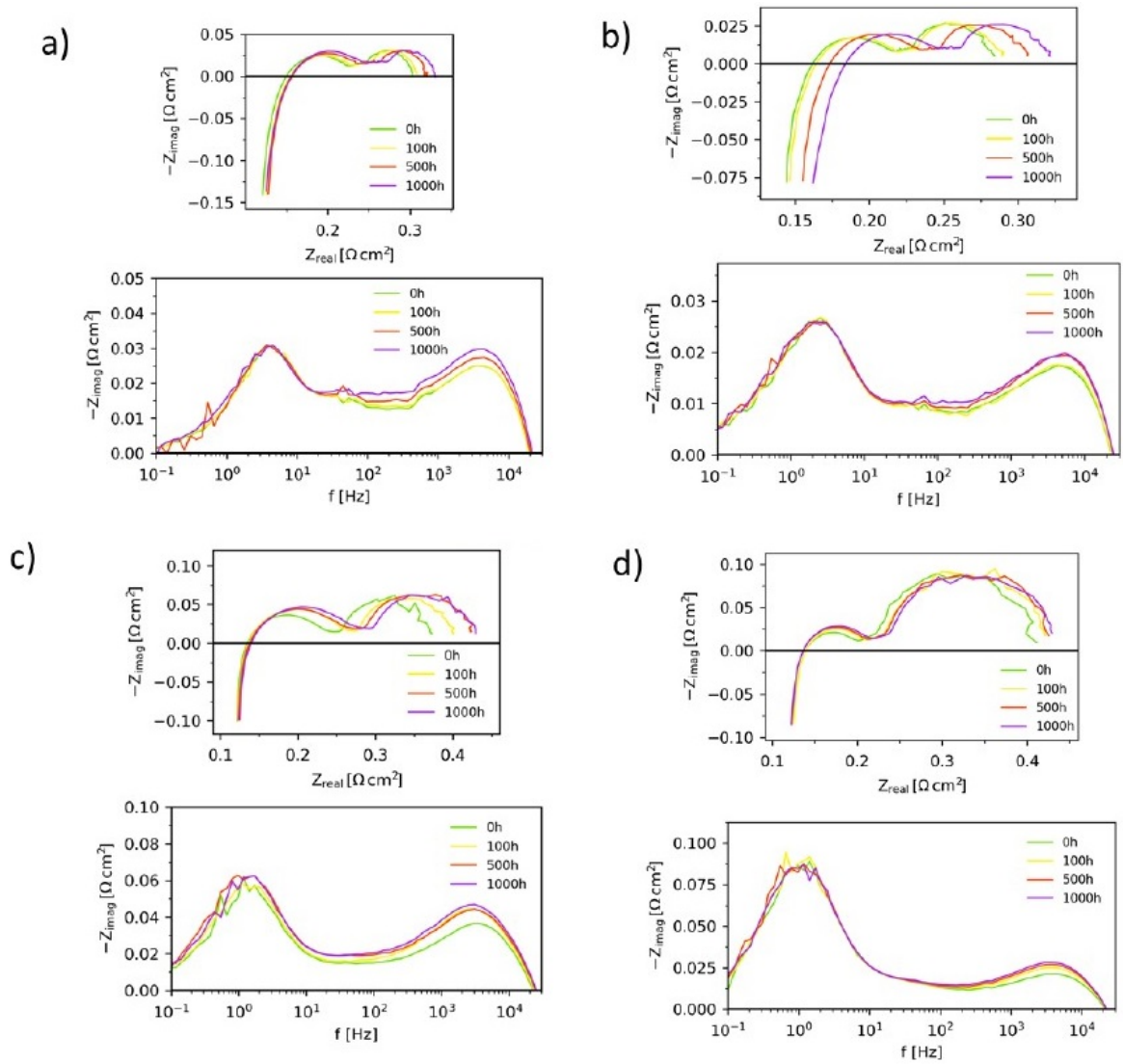
Figure D.1: Nyquist (top) and Bode plots (below) recorded at long term aging at oh, 500h, and 100h for a) 96/4 H_2/H_2O $0.4Acm^2$ FC b)60/40 H_2/H_2O $0.4Acm^2$ FC c)10/90 H_2/H_2O $-0.4Acm^2$ FC d)10/90 H_2/H_2O under OCV condition.

E | Appendix E
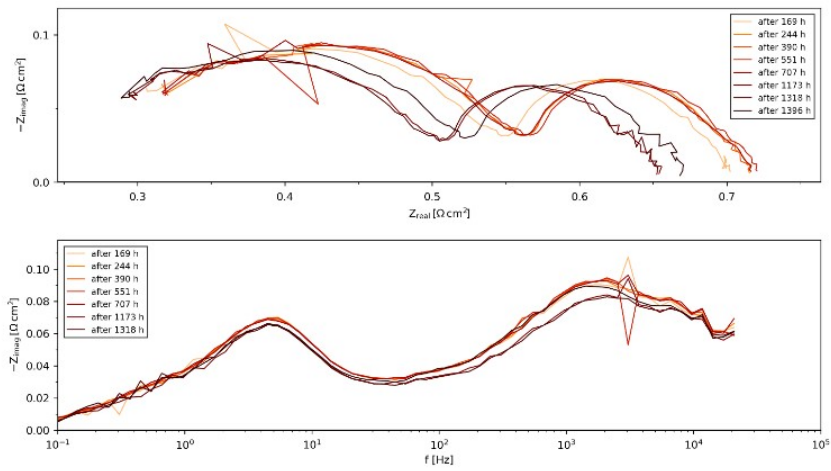
Figure E.1: Cell 2 Nyquist (top), Bode (bottom) for stack B, with a concentration of 10/90 at a T 757°C.
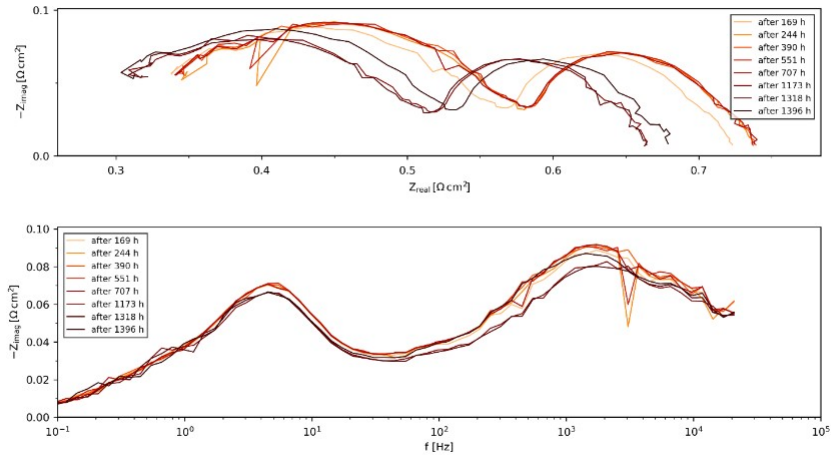
Figure E.2: Cell 3 Nyquist (top), Bode (bottom) for stack B, with a concentration of 10/90 at a T 757°C.
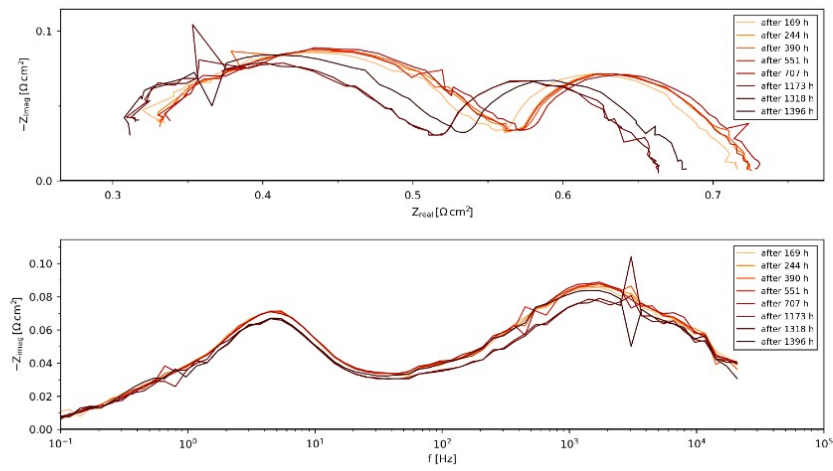
Figure E.3: Cell 4 Nyquist (top), Bode (bottom) for stack B, with a concentration of 10/90 at a T 757°C
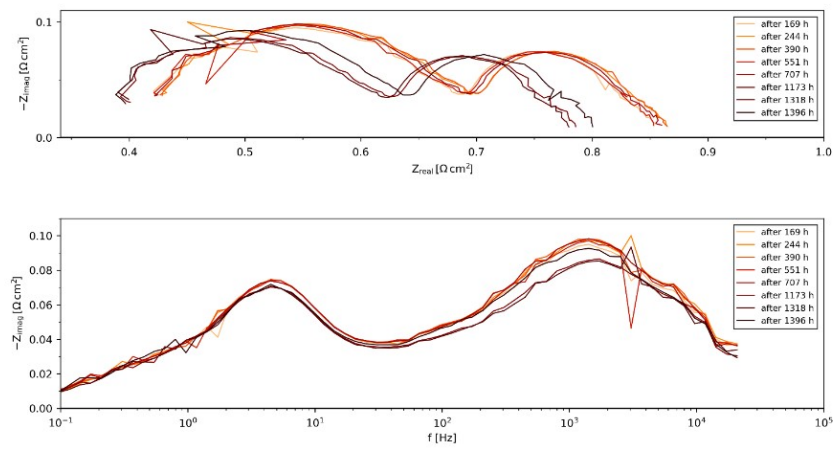
Figure E.4: Cell 6 Nyquist (top), Bode (bottom) for stack B, with a concentration of 10/90 at a T 757°C.

F | Appendix F
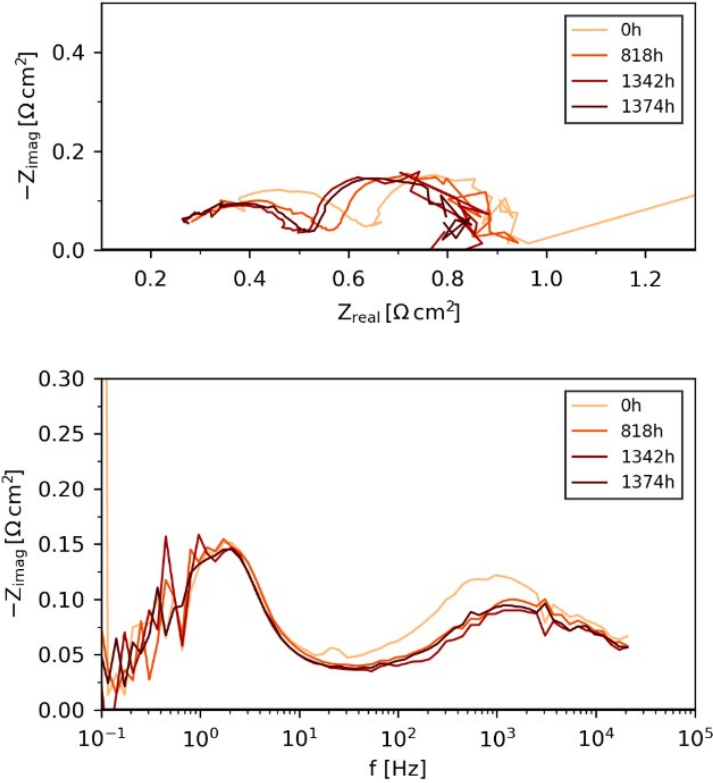
Figure F.1: Cell 2 Nyquist (top), Bode (bottom) for stack B, with a concentration of 60/40 at a T 757°C.
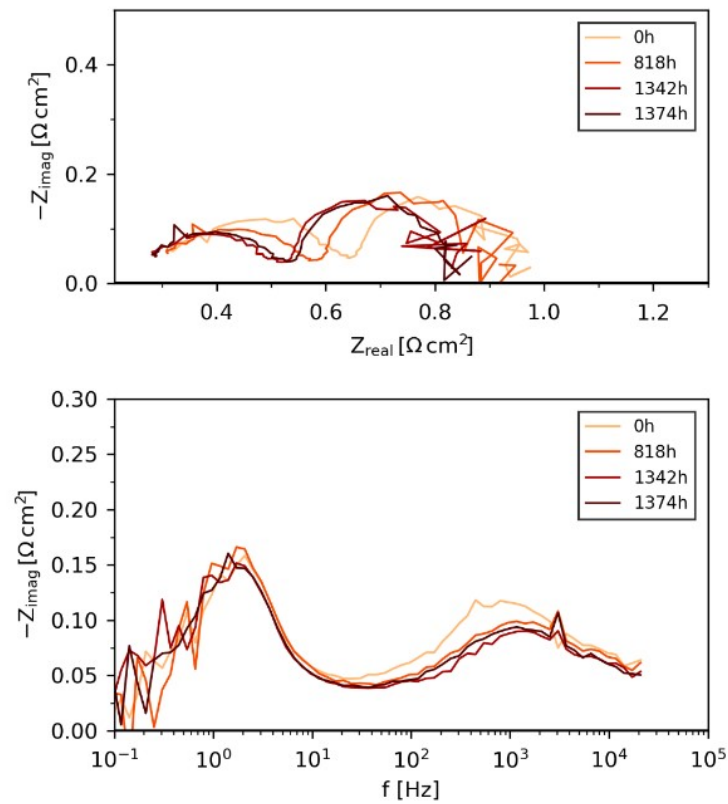
Figure F.2: Cell 3 Nyquist (top), Bode (bottom) for stack B, with a concentration of 60/40 at a T 757°C.

Figure F.3: Cell 5 Nyquist (top), Bode (bottom) for stack B, with a concentration of 60/40 at a T 757°C.

Figure F.4: Cell 6 Nyquist (top), Bode (bottom) for stack B, with a concentration of 60/40 at a T 757°C.

List of Figures

List of Tables

List of Symbols

Variable, acronyms	Description
AEM	Anion Exchange Membrane
AC	Alternating Current
ASR	Area Specific Resistance
CHP	Combined Heat and Power
DC	Direct Current
DTU	Danmarks Tekniske Universitet
EDS	Energy Dispersive x-ray Spectroscopy
EIS	Electrochemical Impedance Spectroscopy
GDL	Gas Diffusion Layer
HER	Hydrogen Evolution Reaction
IPCC	Intergovernmental Panel on Climate Change
LSM	Lanthanum Strontium Manganite
LSC	Lanthanum Strontium Cobaltite
LSCF	Lanthanum Strontium Cobalt Ferrite
LSF	Lanthanum Strontium Ferrite
MIEC	Mixed Ionic Electronic Conductors
MSC	Metal Supported Cell
OCV	Open Circuit Voltage
PEM	Polymer Electrolyte Membrane
RES	Renewable Energy Source
ScSZ	Scandia Stabilized Zirconia
SEM	Scanning Electron Microscope
SOC	Solid Oxide Cell
SOEC	Solid Oxide Electrolysis Cell
SOFC	Solid Oxide Fuel Cell
TPB	Triple Phase Boundary
UF	Utilization factor
YSZ	Yttria Stabilized Zirconia

Acknowledgements

Innanzitutto volevo ringraziare il prof Casalegno per l'opportunità che mi ha dato, successivamente volevo ringraziare la prof Anke Hagen per la sua passione trasmessa e la ricerca veramente interessante proposta alla DTU.

Volevo ringraziare Aiswarya per l'aiuto, la passione e l'insegnamento dato, poi vorrei ringraziare tutti i tecnici alla DTU in particolare Henrick e Axel, e tutti gli amici scoperti in Danimarca.

Volevo ringraziare la mia famiglia che mi ha sostenuto in questo percorso e sopratutto alla Fede che mi ha accompagnato in tutti i periodi e ci siamo sostenuti a vicenda.

E infine ringrazio tutti i miei amici e amici incontrati durante tutto questo periodo che mi hanno fatto crescere e mi hanno accompagnato in questo viaggio.